National Wind Technology Center–Characterization of Atmospheric Conditions

Nicholas Hamilton and Mithu Debnath

National Renewable Energy Laboratory

**NREL is a national laboratory of the U.S. Department of Energy
Office of Energy Efficiency & Renewable Energy
Operated by the Alliance for Sustainable Energy, LLC**

This report is available at no cost from the National Renewable Energy Laboratory (NREL) at www.nrel.gov/publications.

Contract No. DE-AC36-08GO28308

Technical Report
NREL/TP-5000-72091
August 2019

National Wind Technology Center–Characterization of Atmospheric Conditions

Nicholas Hamilton and Mithu Debnath

National Renewable Energy Laboratory

Acknowledgments

Executive Summary

Data provided by the instrumentation located at the National Wind Technology Center (NWTC) is compiled for the purposes of characterizing the atmospheric operating conditions at the National Renewable Energy Laboratory (NREL) wind site. Site conditions are presented aggregating observations by month of the year to show seasonal variation and by characteristic quantities seen in the atmospheric flow including bulk wind speed, direction, and atmospheric stability.

All data reported and analyzed in the following document were collected from instrumentation mounted on the 135-meter-tall meteorological (met) masts at the NWTC near Boulder, Colorado. Each of the two met masts—named M4 and M5—were sited specifically to measure the inflow wind to several of the utility-scale turbines at the NWTC. The construction, operation, and maintenance of the masts have been supported since their commissioning in 2011 by the U.S. Department of Energy (DOE), Office of Energy Efficiency and Renewable Energy, Wind Energy Technologies Office.

Data from the masts are publicly available for download or basic visualization, hosted on NREL's website (nwtc.nrel.gov/135mData). Further, data have been used in the past for a wide range of projects including wind turbine power performance measurements, high fidelity model development and validation, and atmospheric science research. A repository of post-procesing, quality control and visualization codes is avaiable at https://github.com/NREL/MetMastVis and can be used to reproduce many of the graphics included in the current work.

This report describes in detail the atmospheric conditions recorded by M5, the inflow mast for the DOE-owned GE 1.5-megawatt (MW) wind turbine. The report focuses on data recorded from August 2012 to December 2018 and includes:

- An introduction to the wind climate at the NWTC

- A physical description of the met masts

- A review of installed instrumentation

- Data collection, processing, and quality control methods.

In addition to a concise description of the instrumentation from the met masts and the data channels they provide, this report characterizes the behavior of the atmospheric resource first in a cumulative sense, discussing mainly the distribution of wind speeds, flow directions, and thermodynamic properties at several heights along the towers. Periodicity in atmospheric conditions is then detailed through analysis of diurnal and annual cycles of the data streams.

Periods of both low turbulence and extreme atmospheric events that are of interest in terms of wind turbine operation and wind energy research are detailed in the final chapter of this report. The NTWC is known for a relatively higher rate of occurrence of extreme weather events. Extreme atmospheric events observed at the NWTC are compared to their established definitions outlined in the IEC standards. Given the annual variation of operating conditions at the NWTC, wind turbine power performance testing time lines are estimated beginning in each month of the year. Although somewhat less frequent at the NWTC, low-turbulence events are of interest from the perspective of validating new wind turbine and blade designs. Atmospheric conditions and weather patterns that correspond to low-turbulence events are detailed in order to address specific conditions outlined in the IEC standards.

Figure ES-1. Wind turbines and meteorological masts at the National Wind Technology Center. *Photo by Dennis Schroeder, NREL 19015*

Table of Contents

List of Figures

List of Tables

1 Introduction

In 2011, wind turbine manufacturers began producing turbines with hub heights of more than 100 meters (m) above ground level and rotor diameters in excess of 120 m. The continued increase in scale of wind turbines and the respective portion of the overall energy production in the United States requires careful, coordinated monitoring of turbine behavior and wind inflow conditions to understand the impacts of operating wind turbines in complex flow environments. A fundamental step in establishing reliable insights to the interaction between wind turbines and the atmospheric flow comes through a well-documented historical records of atmospheric characteristics and the wind resource in a viable testing and validation environment (Hansen and Larsen 2005; Hand, Kelley, and Balas 2003). The National Wind Technology Center (NWTC) at the National Renewable Energy Laboratory (NREL) has established research partnerships with wind turbine manufactures and offers a premier site for validation of turbine performance under turbulent loading conditions.

Wind turbines operate in the atmospheric boundary layer (ABL), characterized by a wide range of thermodynamic and turbulent conditions. The ABL experiences significant changes in heat fluxes at the lower boundary, switching from convective conditions during the day to stable conditions overnight. Changes in stability are known to play a strong role in the overall character of turbulence and the energy balance posed by the fundamental behavior laws, expressed by a source/sink term coupling the Navier-Stokes equations to the energy equation. The turbulence field varies from location to location and has strong impacts on turbine performance and structural loads (Mücke, Kleinhans, and Peinke 2011). An additional source of energy for atmospheric flows—the rotation of the earth evident through the Coriolis effect—leads to a change in wind direction with height typically quantified through the wind veer. Stability and wind veer represent a departure from the canonical ABL behavior characterized by power or logarithmic profiles (Poulos, Blumen, Fritts, Lundquist, Sun, Burns, Nappo, et al. 2002; Banta, Newsom, Lundquist, Pichugina, Coulter, and Mahrt 2002).

The importance of atmospheric stability and coherent turbulent structures in wind for turbine behavior has been established through a long succession of studies including field measurements (Wharton and Lundquist 2012; Poulos, Blumen, Fritts, Lundquist, Sun, Burns, Nappo, et al. 2002), numerical investigations (Wu and Porté-Agel 2012; Bhaganagar and Debnath 2014; Abkar and Porté-Agel 2015; Lundquist, Churchfield, Lee, and Clifton 2015), and scaled experiments and wind tunnel tests (Hamilton, Suk Kang, Meneveau, and Cal 2012; Chamorro and Porté-Agel 2009). Clifton and Lundquist (2012) used the K-means clustering data mining technique to analyze the winds at the NWTC, finding that these winds could be grouped into four clusters of representative wind speeds and directions based on observations from the M2 meteorological (met) mast installed in 1996.

In previous reporting on the atmospheric characteristics at the NWTC, Clifton and Lundquist (2012) summarize findings from either the 80-m met mast (M2) or the pair of 135-m met masts (M4 and M5), ranging from 1996, when M2 was commissioned. In 2012, the 135-m met masts were updated with new instrumentation and data acquisition system. The design of the masts was specifically suited to quantify inflow winds and the atmosphere with high fidelity and resolution, ranging from the ground across the rotor area of several modern turbines. Instrumentation was synchronized to produce concurrent observations at 20 Hertz (Hz), and the data acquisition system included a set of protocols to quality check data, produce ensemble statistics and derived quantities, and make data available as a public resource. Those data are used in the current report, which is intended to serve as a reference for planning future measurement and control campaigns for wind turbines, novel blade and rotor designs, and as a resource for atmospheric and wind energy research.

2   National Wind Technology Center

Met instrumentation has been affixed to two inflow towers installed at the NWTC, located 36 kilometers (km) (20 miles) to the northwest of Denver, Colorado, and approximately 8 km (5 miles) south of Boulder. The elevation of the wind site is approximately 1,850 m (6,000 feet) above sea level.

Long-term characterization of the atmospheric flow at the NWTC is available as a time-series of measurements made by the M2 at the west end of the NWTC (Figure 1). The historical record available at http://www.nrel.gov/midc/nwtc_m2/ extends from 1996 to the present and shows that the site is dominated by northwesterly winds, coming from Eldorado Canyon, located at the base of the Colorado Front Range. Winds from the west-northwest (WNW) are frequent during the winter and early evenings. Weaker winds may be katabatic winds or drainage flows (Banta, Olivier, and Gudiksen 1993), whereas stronger winds are associated with winter storms and Chinook winds. Winds from the north and south are also seen onsite during summer time, and those winds may be driven by local thermally driven circulation.
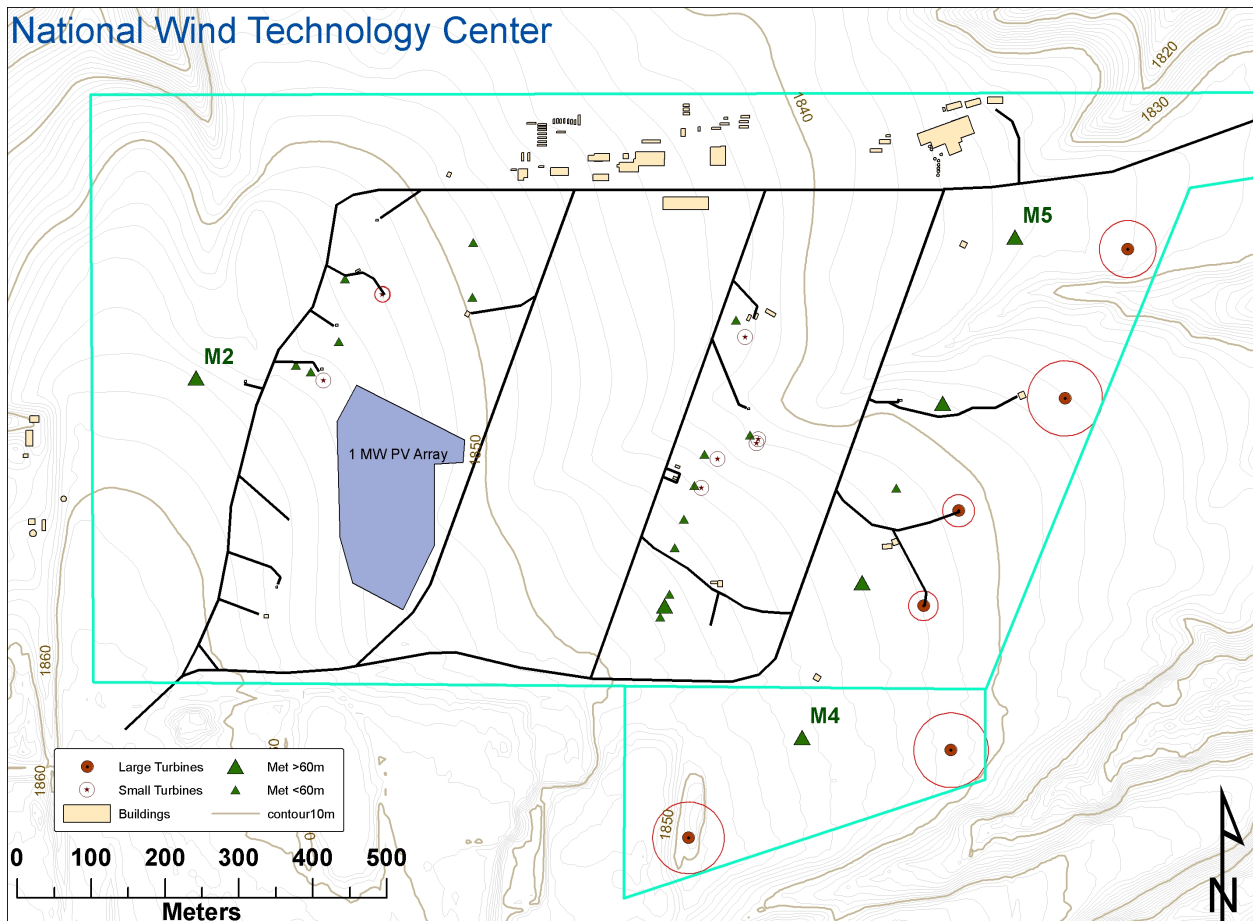
Figure 1. Location of wind turbines and meteorological monitoring towers at the NWTC. *Figure by Joe Smith, NREL*

2.1 Site Layout

The M4 and M5 towers are located on the eastern side of the NWTC grounds (Figure 1). Much of the work below derives results from the M5 met mast, upstream of the DOE-owned GE 1.5-megawatt (MW) wind turbine on site. Results are compared in a limited sense to those from M4, located upstream of the Siemens 2.3-MW turbine. Atmospheric data from M4 are not used to the same degree due to limitations in wind direction that result in unobstructed conditions (see Figure 2a).

All met masts are visible in the site plan as green triangles in Figure 1. Long-term studies and record keeping are being carried out only by the labeled met masts: M2, M4, and M5. The red points and circles in the site plan indicate the position of wind turbines, where the circle scales with the rotor diameter. From the top of the figure are the GE 1.5-MW, Alstom-3 MW (decomissioned in May 2018), the two-bladed and three-bladed Controls Advanced Research Turbines (CART2 and CART3, respectively), the Siemens 2.3-MW, and a Gamesa 2-MW wind turbine. At the time of composition of this report, the Alstom turbine was in the process of being decommissioned and removed from site. Accordingly, obstruction effects from this turbine are no longer an issue for the met masts. However, the wind direction sectors indicating the influence of the Alstom turbine have been retained in Figures 2a and 3a due to the potential impact that the turbine has had on historical records.

2.2 Wind Shadow

Sectors of wind direction that include potential influence of wind turbines on the characterization of the atmospheric conditions at the NWTC were determined using the standards from International Electrotechnical Commission (IEC) 61400-12 Annex A and Annex B (IEC 2005). The standard describes in detail the procedure to determine which sectors are not usable for resource characterization due to the influence or uncertainty introduced by an operating wind turbine or obstacle.

From the standards, the procedure consists of two steps, to be applied in the following order:

1. Evaluation of influences caused by operating wind turbines including the met mast itself as well as neighboring and operating wind turbines, described in Clause A.2.

2. Evaluation of influences caused by obstacles, as described in Clause A.3 and Clause A.5.

Direction sectors that remain after the procedure suggested by IEC Annex A are considered to be valid in terms of analysis. Shadowed sectors for each of the met towers are illustrated in Figures 2a and 3a and described in Tables 2b and 3b.

The purpose of site calibration is to quantify changes in the boundary layer as it follows the local terrain, generally considered to be attached flow. Obstacles can generate turbulent wakes that may induce flow separation and increase the variability in flow measurements. According to the IEC, site calibration of instruments does not typically work well for correcting the effects of flow separation. It should be noted that the IEC standards are quite conservative, and they suggest that an increase in variability by more than 1% be excluded from consideration. To determine the valid wind directions for each met mast at the NWTC, the complete set of site constructions (including buildings, wind turbines, met masts, and terrain) were considered.

In all cases, the terrain was determined to comply with the requirements in Annex B, indicating that it could be considered "flat" and that no site calibration is required due to local orography. Specifically, IEC 61400-12 Annex B accounts for the following:

- Orography at the test site, which may only show minor variations from a plane and passes both through the base of the tower and the terrain within the respective sector.

- The planes to not exceed a certain limit for the slope, 3%–5%, depending on the distance from the base of the tower.

For each met tower, the only additional sources of uncertainty came from other wind turbines on site. Buildings and other equipment at the NWTC did not exceed accepted values outlined by IEC 61400-12 Annex A and Annex B.
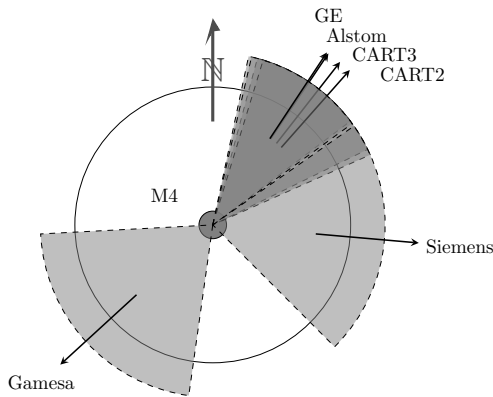
(a) Wind shadow for M4 met mast

Obstruction	Start Angle (°)	End Angle (°)
GE	15	53
Alstom	12	64
CART3	13	54
CART2	17	66
Siemens	55	135
Gamesa	188	267

(b) Wind direction angles to be excluded from analysis for M4

Figure 2. Shadowed wind direction sectors for the M4 met tower and instrumentation
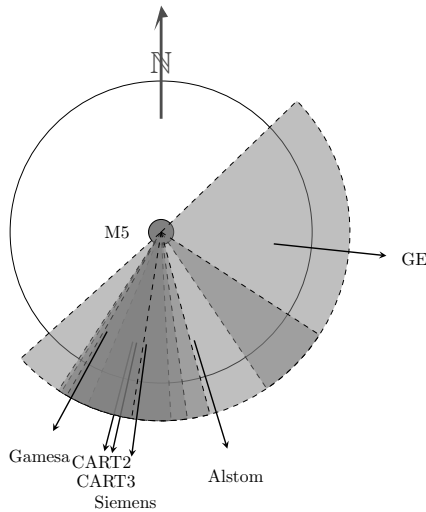
(a) Wind shadow for M5 met mast

Obstruction	Start Angle (°)	End Angle (°)
GE	46	146
Alstom	123	203
CART3	172	213
CART2	177	212
Siemens	165	210
Gamesa	189	228

(b) Wind direction angles to be excluded from analysis for M5

Figure 3. Shadowed wind direction sectors for the M5 met tower and instrumentation

3 Instrumentation

Each of the met masts at the NWTC are outfitted with a range of instrumentation for observation of atmospheric conditions. Raw data produced by the instruments are shown in Table 1, including the parameters measured by each device as well as their specified measurement ranges and accuracy, where possible. Note that accuracy data are from the manufacturer's specification sheets unless otherwise stated.

Table 1. Devices to Measure Atmospheric Properties and Mast Behavior on the M4 and M5 Masts

Parameter	Description	Device	Range	Accuracy
WS	Wind speed	Met One SS-201 Cup anem.	0 to 90 m/s	0.5 m/s or 2%
$WS(1)$	Wind speed (class one)	Thies 4.3351.10.0000	0 to 75 m/s	
WD	Wind direction	Met One SD-201 Vane	0 to 360°	3.6°
T	Air temperature	Met One T-200A platinum RTD	± 50°	
Tdp	Dew point temperature	Therm-x 9400ASTD	± 50 °C	
ΔT	Differential temperature	Met One T-200A	-4.44 °C to +6.66 °C	
u_x, u_z, u_z	Wind components	ATI K-Type sonic anem.	± 30 m/s	0.01 m/s
accn	Boom triaxial acceleration	Summit 34201A	± 2.4g (all axes)	
T_s	Sonic temperature	ATI K-Type sonic anem.	-50 °C to +60 °C	0.1° C
P	Barometric pressure	AIR AB-2AX	740 to 1,000 mBar	
Precip	Precipitation	Vaisala DRD11A	0 (heavy) to 3 (dry)	None given

A short description of the met mast construction and the location of each of the 135-m met masts are provided in Section 3.1, including schematics that show the vertical location of instrumentation along each tower height. Additional details for each instrument are provided in Sections 3.2 through 3.5.

3.1 Meteorological Masts

3.1.1 Boom Arms

Met masts at the NWTC feature two different types of boom designs. Booms are distinguished by their length and the particular instrumentation they support:

- Short booms are 12-feet-long, 2-inch square section, retractable aluminum booms from Tower Systems, Inc. (http://www.towersystems.com). Booms are guyed back to the mast at three points. These booms are usually used as mounts for cup anemometers, wind vanes, and temperature sensors.

- Long booms are custom designed and built to be rigid when deployed but also retractable. They are braced on two sides of the mast and guyed above and below. These booms are used only as mounts for the sonic anemometers.

3.1.2 M4 Mast

The M4 mast (also known as the "site 4.4" mast) is approximately 2 rotor diameters (≈201.6 m) away from a Siemens 2.3-MW wind turbine (see the site map in Figure 1). A sketch of the mast design is shown in Figure 5a. Sensors are listed in Table 5b following the descriptions provided in Table 1. Data from M4 are

not discussed at length in the current report due to the narrow band of directions that are considered free from obstructions as shown in Figure 2a. Additionally, data from M4 are less consistently available than those from M5. The instruments on M4 were decommissioned and moved to other locations at the NWTC on September 2015.
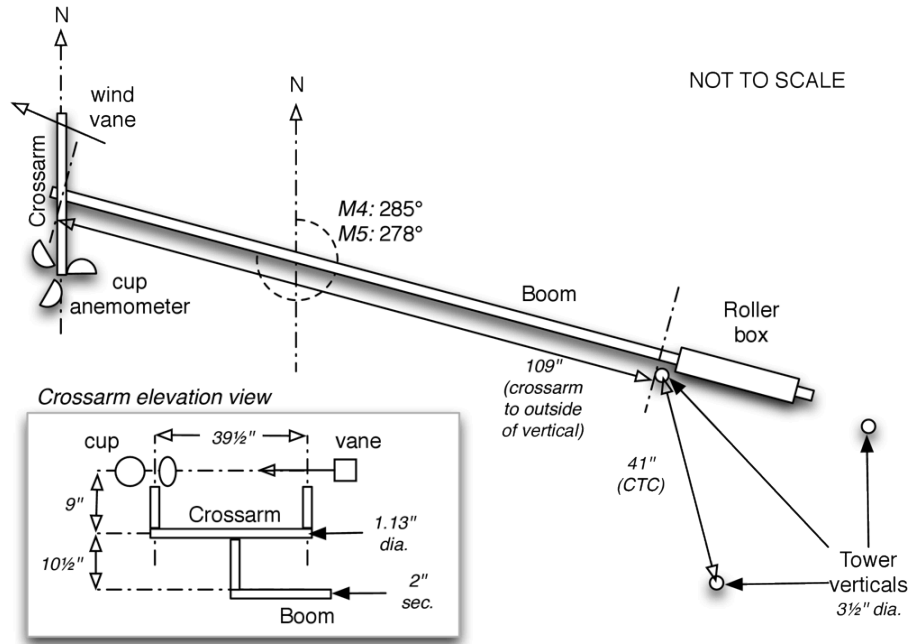
(a) Plan and elevation views of wind direction and wind speed sensors on short booms
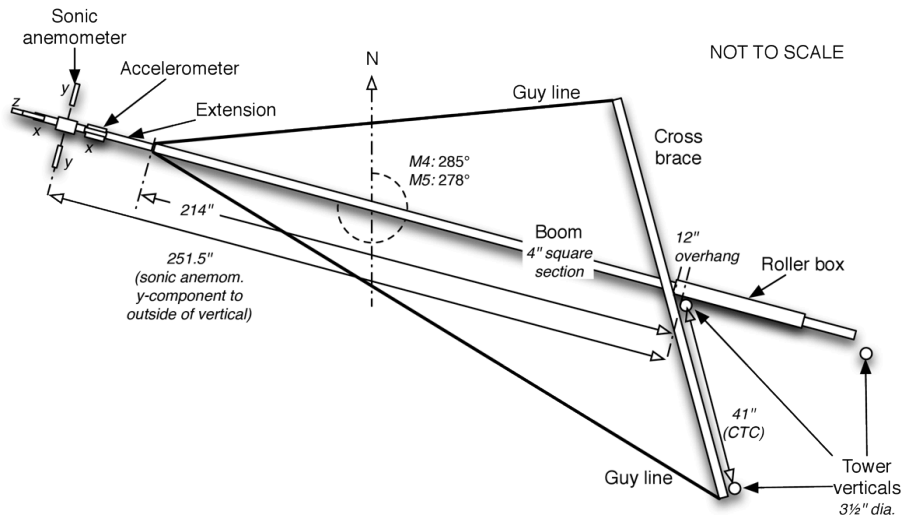
(b) Plan view of sonic anemometers on long booms

Figure 4. Instrumentation booms on the M4 and M5 towers. True north is designated in each schematic.
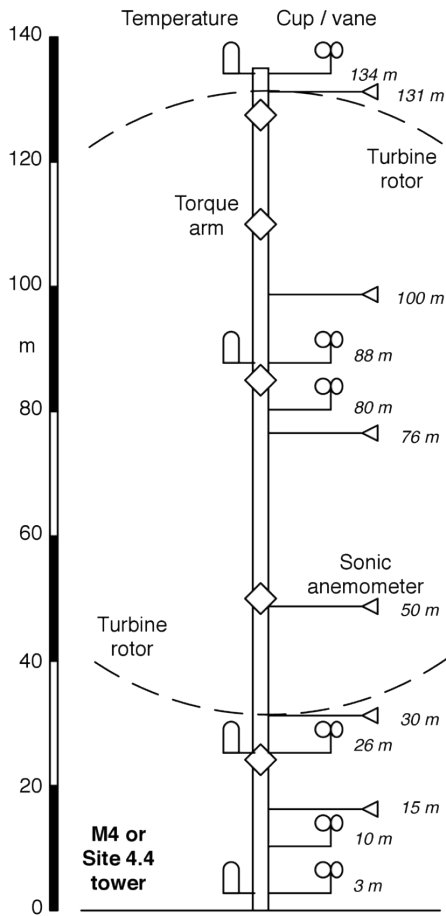
(a) Schematic of the NWTC M4 met tower showing locations of relevant geometry and instrumentation

(b) Instrumentation on the M4 mast

Height (m)	Measured Parameter	Boom Type
134	WD, WS, T_{dp}, ΔT	Short
131	Sonic (u_x, u_y, u_z, T_s), accn	Long
100	Sonic (u_x, u_y, u_z, T_s), accn	Long
88	WD, WS, T_{dp}, ΔT	Short
80	WS(1)	Short
76	Sonic (u_x, u_y, u_z, T_s), accn	Long
50	Sonic (u_x, u_y, u_z, T_s), accn	Long
30	Sonic (u_x, u_y, u_z, T_s), accn	Long
26	WD, WS, T_{dp}, ΔT	Short
15	Sonic (u_x, u_y, u_z, T_s), accn	Long
10	WD, WS	Short
3	WD, WS, T, T_{dp}	Short
3	P, precip	N/A

Figure 5. Detailed description of the M4 met tower and instrumentation

3.1.3 M5 Mast

The M5 mast (also known as the "site 4.0" mast) is 162.2 m away from a GE SLE 1.5-MW wind turbine (see the site map in Figure 1). A sketch of the mast design is shown in Figure 6a. Sensors are listed in Table 6b following the descriptions provided in Table 1. M5 is considered to be the best source of research-grade data currently operating at the NWTC due to its level of instrumentation. The results presented in the next section are derived from data streams provided by the instruments on M5.

3.2   Wind Speed and Direction Measurements

In-situ observations of the ABL velocity are made with sonic and cup anemometers located along the met masts. Cup anemometers provide wind speed observations, listed as "WS" in Tables 1, 5b, and 6b. Cup anemometers are co-located with wind vanes to provide wind direction measurements (listed as "WD") that complement the wind speed measurements. Sonic anemometers also provide wind speed and direction information, but convey that information in terms of wind velocity vector components u_x, u_y, and u_z. From
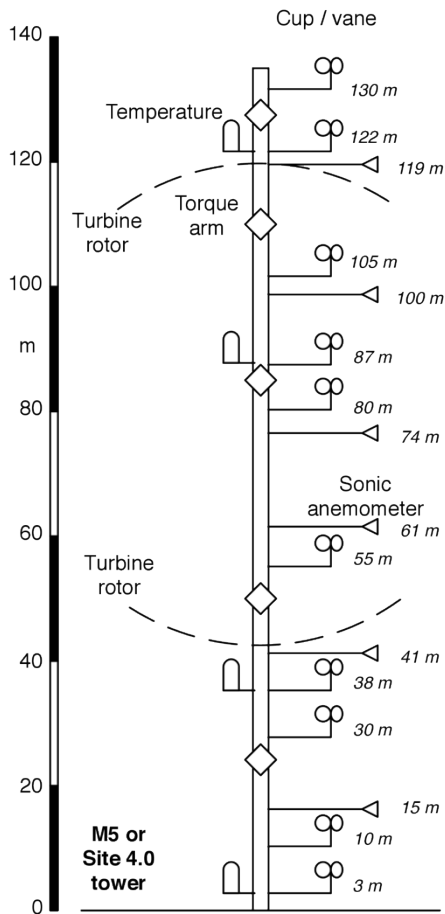
(a) Schematic of the M5 met tower at the NWTC showing locations of relevant geometry and instrumentation

(b) Instrumentation on the M4 mast

Height (m)	Measured Parameter	Boom Type
130	WS(1)	Short
122	WD, WS, T_{dp}, ΔT	Short
119	Sonic (u_x, u_y, u_z, T_s), accn	Long
105	WS(1)	Short
100	Sonic (u_x, u_y, u_z, T_s), accn	Long
92	—	Short
90	—	Short
87	WD, WS, T, T_{dp}, ΔT,	Short
80	WS(1)	Short
74	Sonic (u_x, u_y, u_z, T_s), accn	Long
61	Sonic (u_x, u_y, u_z, T_s), accn	Long
55	WS(1)	Short
41	Sonic (u_x, u_y, u_z, T_s), accn	Long
38	WD, WS, T, T_{dp}, ΔT,	Short
30	WS(1)	Short
15	Sonic (u_x, u_y, u_z, T_s), accn	Long
10	WD, WS	Short
3	WD, WS, T, T_{dp}	Short
3	P, precip	N/A

Figure 6. Detailed description of the M5 met tower and instrumentation

the vectorial components of the wind velocity vector, cup-equivalent wind speed and wind direction can be calculated. Wind speeds and directions are used interchangeably from all instruments on the met masts.

3.2.1 Sonic Anemometers

Working theory and operation of sonic anemometers are frequently measured against cup anemometers (Wyngaard 1981). Oncley, Friehe, Larue, Businger, Itsweire, and Chang (1996) offer a comprehensive overview of the data processing requirements for sonic anemometer data streams. Sonic anemometers affixed to the met masts provide time series of the three Cartesian components of the flow passing through the "open path" of the device, as shown in Figure 7. Wind speed is calculated in the open path by measuring the difference in the speed of sound in three directions through the domain. Current instrumentation at the NWTC includes Applied Technologies K-Type sonic anemometers installed on the M4 and M5 masts.

Sonic anemometers are located at the extreme positions along long booms of M4 and M5. At full boom extension, the sonic anemometers are approximately 6.4 m (5.7 times the tower face width) from the outside

of the mast tower structure. Boom motion is quantified with a three-axis accelerometer located near each device (Figure 4b and Figure 7). Accelerometer signals are used to quantify conditions under which sonic anemometer data may require correction. A route to ground for lightning (Figure 7) is offered through a grounding rod installed between the arms of the anemometer and a wire running down the mast.

(a) Schematic including the coordinate system of the "K- type" anemometer installed on the met mast

(b) ATI "K-type" sonic anemometer. The x and y wind components are measured with the arms on the top and bottom of the boom. The z wind component is measured with the arm on the end of the boom.
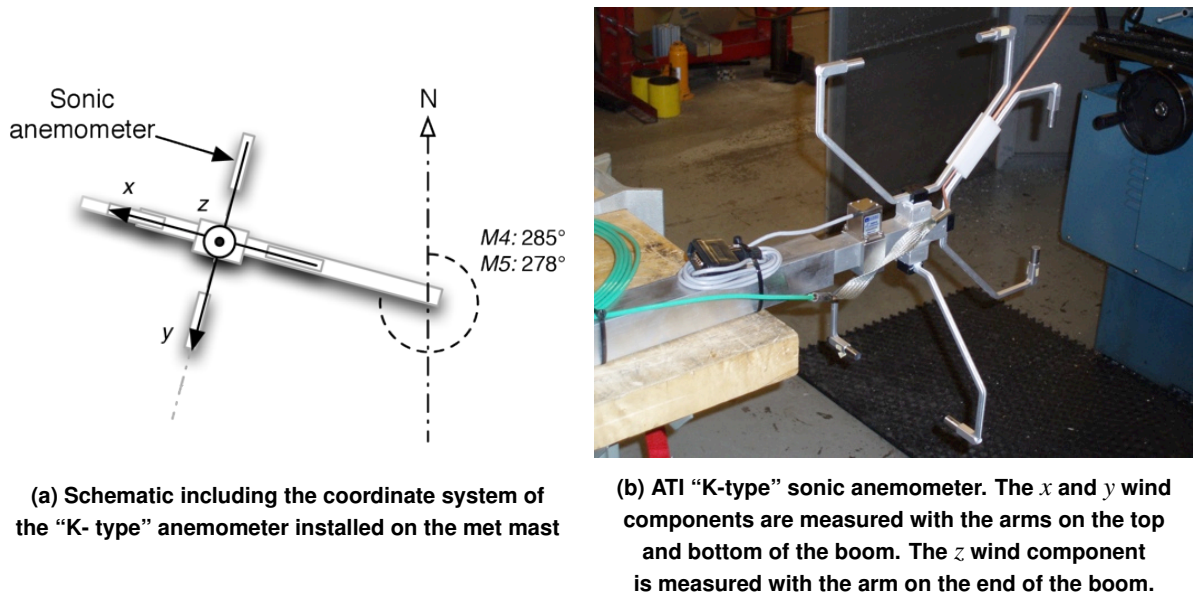
Figure 7. Example schematic and image of the sonic anemometers located on the M4 and M5 met masts. Image credit: Clifton (2014).

3.2.2 Cup Anemometers and Wind Vanes

Cup anemometers in use on the M4 and M5 masts are of two types (Figure 8). "Class one" anemometers reach the highest level of accuracy and repeatability laid out in the IEC's guidelines for anemometry specifically for power performance testing (IEC 2005). The anemometers used on the M4 and M5 masts are manufactured by Thies (Table 1). Combined cup anemometers and vanes are also installed on the masts and manufactured by Met One (model no. WS-201). The Met One device combines a cup anemometer (model no. SS-201) and wind vane (model no. SD-201).

3.3 Temperature Measurements

Other atmospheric quantities are measured along the met masts to fully characterize the conditions at the NWTC at any given time. Air and dew point temperature measurements are collected using a Met One 327C aspirated (ventilated) thermal radiation shield (see Figure 9). Within the radiation shield are sensors for air temperature and differential temperature, while the dew point sensor is in a separate enclosure (DP200B, Figure 9a). During operation, a flap in the tube is forced open by the flow of air, actuating a switch to initiate measurement. The operational status of the aspirator is checked automatically and reported as an element in the output data stream and ultimately factored into the quality control for air and dew point temperature.

Temperature measurements are co-located with the WS-201 Wind Sensors on many of the short booms, as shown in Figure 9b. Differential temperature measurements quantify the difference between temperature

(a) Met One cup anemometer   (b) Thies cup anemometer

Figure 8. Example cup anemometers from the met masts. Image credit: Clifton (2014).

signals at various heights along the met masts, amplified and converted to conventional engineering units. Handling the signal processing at the time of record gives a higher accuracy for temperature difference than would otherwise be possible using the difference in the engineering units directly.

3.4 Barometric Pressure

Barometric pressure is measured with an AIR AB-2AX sensor located near the base of the met masts in the data collection buildings. Pressure sensors are connected to a pressure tap outside the building 3 m above ground. Pressure sensors have been calibrated to the range 780–840 mBar, beyond the expected range of barometric pressure at the NWTC's altitude above sea level.

3.5 Precipitation

Precipitation is measured using a precipitation sensor mounted at the data collection building on the NWTC site 100 m from the base of the mast to the west of M5 (Figure 1). Precipitation is measured with a Vaisala DRD11A sensor, which responds to rain, snow, and hail. The sensor quantifies precipitation in the range of 0–3, with 0 meaning heavy precipitation and 3 meaning no precipitation.
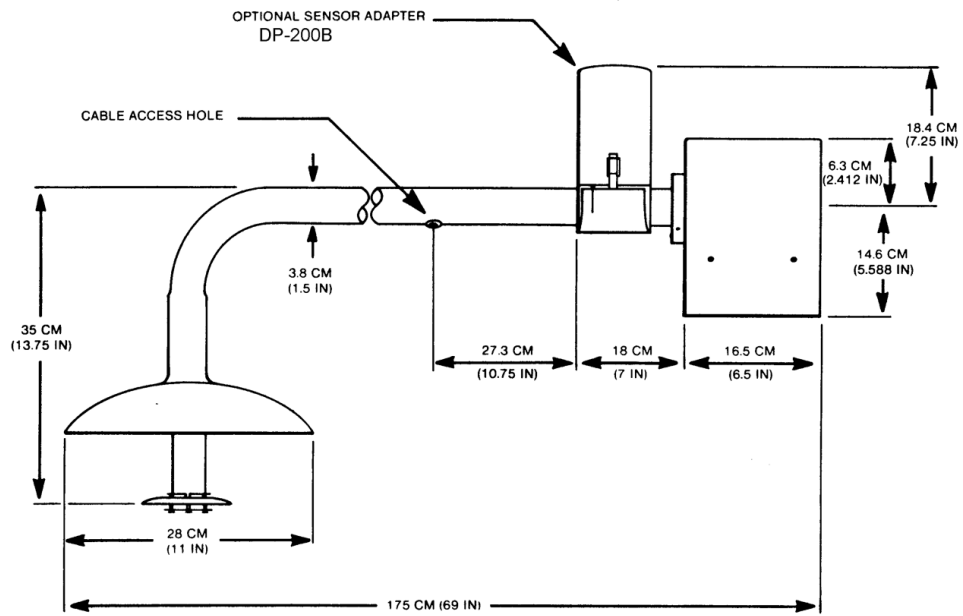
(a) Met One 327C aspirated thermal radiation shield, Met One instruments

(b) Co-located wind sensor WS-201 and aspirated thermal radiation shield M0327C at 3 m above ground on the M4 mast

Figure 9. Example cup anemometers from the met masts

4   Data Acquisition

Measurements made by sensors are collected and recorded in the data sheds near the base of each met mast. In each shed, a rack-mounted data acquisition system from National Instruments accepts voltage signals supplied as outputs of each instrument and reads serial signals where appropriate. The voltage signals are processed into engineering units by the National Instruments software and written to files containing 10 min of raw binary data.

All hardware is mounted in 19-inch racks in the data sheds at NWTC sites 4.4 and 4.0 for the M4 and M5 met masts, respectively. Each system is connected to a rack-mounted chassis that also contains a processing computer and PXI cards that accept inputs from instrument signals and transmit the data to the main processing center. Data acquisition hardware installed in the data sheds is listed in Table 2.

Data acquisition systems at the NWTC are designed specifically to comply with the requirements put into place by the American Association for Laboratory Accreditation (A2LA). Data acquisition systems include documentation for every device installed on the masts. Every measurement device used on the met masts was calibrated before installation and re-calibrated as required by the guidelines set forth by the A2LA. Calibration information is accessible through the web portal for data streams at the NWTC (nwtc.nrel.gov/135mData).

4.1   Software

Data streams from each instrument on the met masts are fed by the PXI chassis to a dedicated processing computer running a specialized virtual instrument constructed in LabVIEW. The LabVIEW virtual instrument reads voltage signals from the instruments, converts each one to the respective physical information in engineering units, and writes data to 10-min (min) formatted binary files synchronized to 20 Hz. Data acquisition rates are controlled using a global positioning system (GPS) clock, which is also used to generate the time stamp for each 20-Hz data record.

To summarize the data acquisition process (shown also in Figure 10):

1. Channels are defined from configuration files for each met mast, stored locally.

2. A trigger signal is generated at 20 Hz from the GPS timing unit. Each instrument signal is synchronized to the GPS timing signal.

3. For every signal read/write trigger at 20 Hz:

   a. The time stamp is recorded as `MM_DD_YYYY_HH_MM_SS_US`.

   b. All analog channels (cups, vanes, and temperatures) are measured.

   c. Sonic anemometers are triggered to record, and the 50-millisecond serial buffer is emptied.

   d. All data are appended to the file corresponding to the current 10-min bin.

4. At the end of the 10-min collection period, a new data file starts.

Table 2. Hardware Components in the Data Acquisition System

Function	Model	Description
Controller	PXI 8108	Embedded PC
GPS timing unit	PXI 6682H	Receive, interpret, and rebroadcast GPS timestamp
Serial interface	PXI 8431	Serial ports for sonic anemometer signal communication
Analog input/output (IO)	PXI 6225	Analog signals (e.g., wind directions from vanes)
Digital input/output (IO)	PXI 6624	Status of aspirator fans
Pulse counting	PXI 6624	Pulse counting (e.g., cup anemometers)
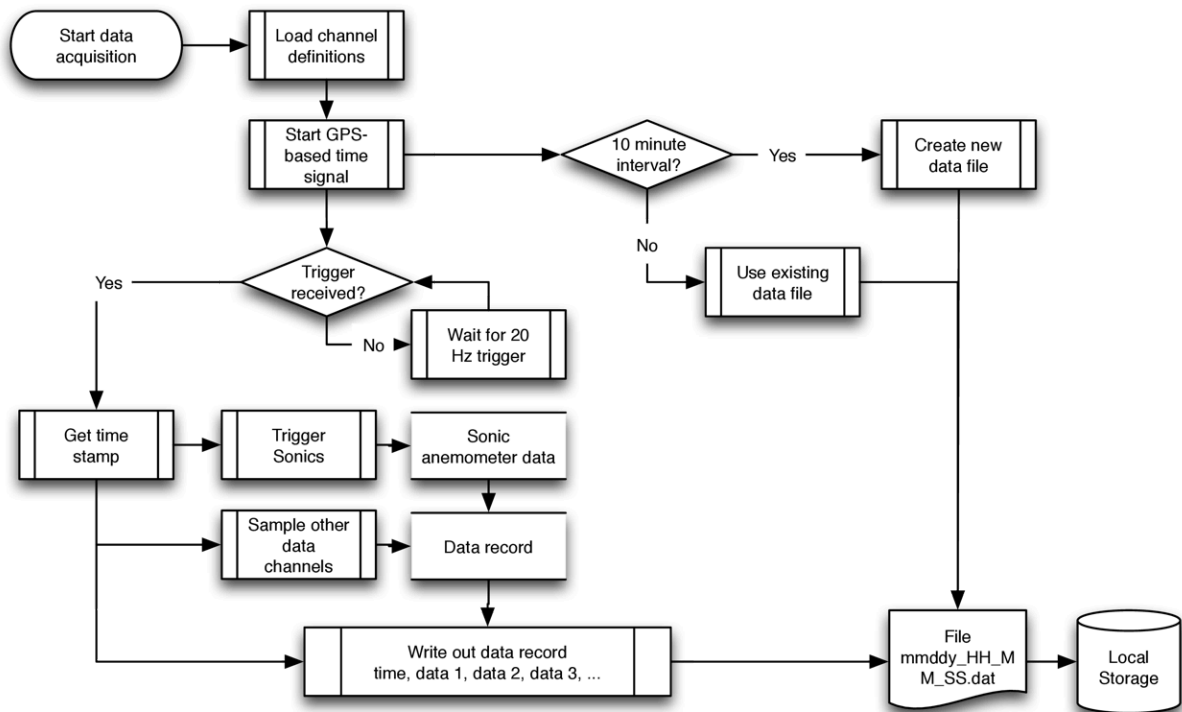
Figure 10. Data acquisition process diagram

4.2   Quality Control

All data streams processed by the data acquisition system described in Section 4 are subject to a quality-control (QC) algorithm that runs continuously. As part of the process, additional columns are written to the 10-min binned data files, paired to each data stream, that indicate the quality of the respective data. Results of the QC algorithm are recorded using numerical QC codes. Multiple QC flags exist to indicate a variety of channel status or data quality levels. A brief summary of the QC process follows:

- As data are recorded, they are checked for availability and consistency.

- If data quality is questionable, data are flagged even if they may still be useful. Flagging of data is triggered by:

- Irregular timing: The data acquisition system synchronized each data channel to 20 Hz and should provide new data every 0.05 s. If the timing becomes irregular (i.e. more than 1% of data are more than 5% from the ideal period) a QC code is set.

- Data rates: Manufacturers of each instrument provide suggested limits for data availability. If the number of points supplied by the data stream fall outside of the suggested limits, a QC code is set.

- Low standard deviation: In some cases, instruments freeze or stall and produce a single value for a time. If the standard deviation of a data stream is recorded at or below 0.01% of the mean, that channel is assumed to have stalled during the measurement interval and a QC code is set.

- A data channel is considered to have failed if data are definitely unusable. Reasons for failing data include:

  - Empty data channel: If a channel is empty, a QC code is set.

  - All bad values: If all data in a channel have known "bad" values (e.g. -999) a QC is set.

  - All "not a number" (NaN): If all data in a channel are NaN values, a QC code is set.

- If no quality code is recorded, data are considered to have passed the automated QC process.

The QC process produces many different QC codes that indicate the status of the data within a given 10-min bin and also indicate the cause for that code. A simplified QC code system is often more useful in practice. In the 10-min binned data available on the NWTC data portal, each bin is given one of three codes:

- 1: No QC or status code received, data are considered to be valid.

- 0: Data have been flagged for review, but may still be useful.

- -1: Data are considered to have failed and are unusable.

In the following review of atmospheric conditions at the NWTC, only data that have a status code of 1 are used. Any data that have failed or have been flagged for further review were omitted. In addition to the status codes mentioned earlier, the accepted data have been subject to a denoising algorithm as part of the acceptance protocol. This prevents egregious outliers or spikes from skewing statistics and derived results from the data channels. Figure 11 shows the availability of the quality-controlled data for M5 over the time range considered in the current report.

4.3   Raw Data

Raw data produced by the instrumentation on the met towers are collected through an automated data reporting system assembled by Andy Clifton. Measured values are converted into 10-min values and combined to calculate other properties. Where possible, data processing follows the same methods as used at the NWTC for the M2 met mast. A complete list of raw data channels for each met tower is provided in Appendix A, including the channel number used to record the data, a description of each variable, the variable name used in raw data files, and the height at which the instrument used to record the data is located on the respective met tower.

Data processing results in the following analysis of the atmospheric site conditions at the NWTC and takes place after the data acquisition and QC processes described in Section 4. The data acquisition process
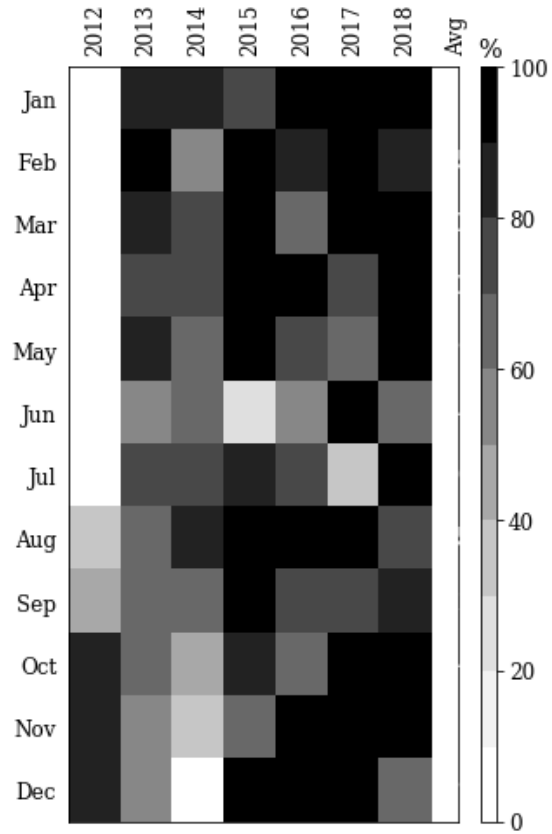
Figure 11. Data availability from M5 during the assessed time range
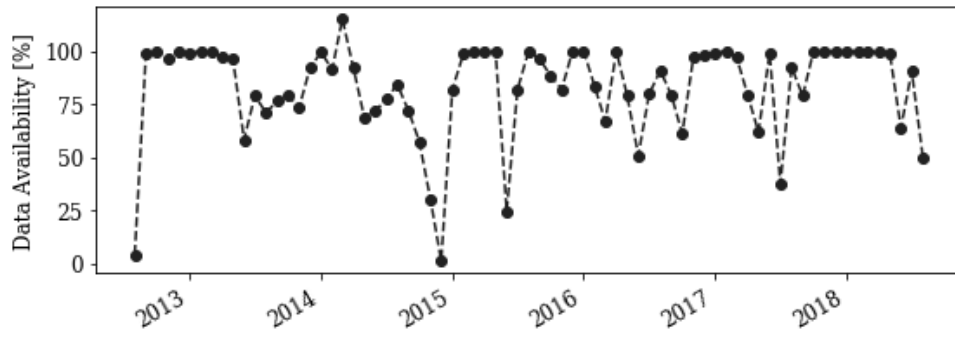
Figure 12. Data availability from M5 as time series

described in Section 4 writes binary archive files along with QC flags. "Raw" data read from the archive are those that have not been filtered according to the QC flags or any other method. The general process for data analysis can be summarized as:

1. Instrument data are read from binary data files containing 10-min blocks of 20-Hz data.

2. The QC procedure described earlier is applied to data, metadata are queried, and potentially "bad" data are flagged. Each instrument channel is compared to manufacturers' limits.

3. Basic statistical quantities (e.g., means, standard deviations) are calculated for each channel as an additional quality assurance step.

4. Statistics are generated for desired signals (e.g., wind speed, stability, turbulence intensity).

5. Signals are combined to quantify *derived* values that require more than a single information stream.

5 Theory

5.1 Mean Atmospheric Flow

Mean flow characteristics are calculated for each of the 10-min data files processed by the data acquisition system described above. Following the IEC standard 61400 for wind turbines (IEC 2005), a 10-min averaging period was chosen as the default interval over which ensembles are considered for statistics. Atmospheric quantities are assumed to be stationary within each 10-min block of data. During periods of rapid change in the atmospheric conditions, this assumption is not expected to hold. Extreme events outlined by the IEC standards occur over timescales on the order of 6–12 s, and are quantified in greater detail in Section 7.

The mean wind speed and direction are calculated at each level of the met masts containing wind speed sensors (either cup or sonic anemometers) by first converting the 20-Hz wind speed, WS, measured by the cup anemometers and direction, WD, measured by the vanes into 20-Hz orthogonal wind components in the meteorological zonal (west-east, u_m) and meteorological meridional (south-north, v_m) directions as:

$$u_m = -\text{WS}\sin\left(\frac{\pi \cdot \text{WD}}{180}\right) \tag{5.1}$$

$$v_m = -\text{WS}\cos\left(\frac{\pi \cdot \text{WD}}{180}\right) \tag{5.2}$$

where positive u_m and v_m correspond to the conventional Cartesian directions, indicating wind blowing to the east and to the north, respectively. Mean wind speed is calculated for each 10-min interval as the vector mean of the orthogonal wind components:

$$\overline{V} = \left(\overline{u_m}^2 + \overline{v_m}^2\right)^{1/2} \tag{5.3}$$

Wind direction is recorded using the compass convention with $0°$ corresponding to north and increasing in the clockwise direction and describes the direction of origin of the wind. In contrast, the Cartesian convention for vector direction begins $0°$ at the positive x-axis and increases counterclockwise, indicating the direction that the vector points. Here, wind direction follows the compass convention and is calculated from components of average wind speed as:

$$\overline{\text{WD}} = \text{atan2}\left(\overline{u_m}/\overline{v_m}\right) \cdot \frac{180}{\pi} \tag{5.4}$$

where the function atan2(x) is the inverse tangent that takes into account the quadrant of each signal $\overline{u_m}$ and $\overline{v_m}$ and has the default range of $\pm\pi$.

5.2 Turbulence

Turbulence broadly describes the variability inherent to the observed flow field and is quantified through the deviation of each velocity signal from its respective ensemble average value, $\overline{V}$. In this current report,

17

turbulent fluctuations (i.e., deviations of the instantaneous velocity signal from the ensemble average) are denoted by lowercase letters with a prime as:

$$u' = u(t) - \overline{U} \tag{5.5}$$
$$v' = v(t) - \overline{V} \tag{5.6}$$
$$w' = w(t) - \overline{W} \tag{5.7}$$

In most instances, the vertical component of the velocity is assumed to be null in ensemble $\overline{W} = 0$ and the frame of reference to the wind speed is rotated such that the transverse velocity is also null $\overline{V} = 0$. When implemented, this convention effectively enforces a one-dimensional mean flow field, although turbulence remains a three-dimensional phenomenon. Turbulence intensity, I, is the ratio that compares the standard deviation of the fluctuating velocity field to the mean flow:

$$I(u) = \frac{\sigma_{u'}}{\overline{U}} \cdot 100 \tag{5.8}$$

The description of the turbulent velocity fluctuations in frequency space indicates a wide range of relevant length and timescales in each velocity signal. Accordingly, measurement devices must be capable of resolving a wide range of wind speeds and have sufficient resolution in time to capture rapid changes. Sonic anemometers are used to make observations to quantify turbulence as they have no inertia, a small measurement volume, and take measurements at a high frequency. In contrast, the inertia of cup anemometers makes them unreliable for high-frequency turbulence measurements.

Sonic anemometers measure winds in three distinct directions and can then be used to calculate three Cartesian components of the velocity vector, rather than as separate and individual signals for wind speed and direction, as with cups and vanes. With the sonic anemometers, the mean wind vector is calculated from 10-min blocks of measurements and rotated into the prevailing wind direction during postprocessing. The rotation fits the measured data to find a three-dimensional wind vector with a stream-wise component, u; transverse component, v; and vertical component, w, for the 10-min interval. The mean stream-wise velocity is maximized, while the mean transverse and vertical components are vertical over the interval. Cup-equivalent wind speeds are calculated from the Cartesian components of velocity supplied by the sonic anemometers.

Turbulent fluid stresses are calculated by combining fluctuating velocity signals in the Reynolds stress tensor as:

$$\overline{u_i u_j} = \begin{bmatrix} \overline{u'^2} & \overline{u'v'} & \overline{u'w'} \\ \overline{v'u'} & \overline{v'^2} & \overline{v'w'} \\ \overline{w'u'} & \overline{w'v'} & \overline{w'^2} \end{bmatrix} \tag{5.9}$$

Turbulent kinetic energy (TKE) is a measure of the energy in the turbulent velocity fluctuations that includes all three velocity components, rather than the turbulence intensity that only includes the streamwise component. The mean TKE over a 10-min interval is defined as half of the trace of the Reynolds stress tensor:

$$\text{TKE} = \frac{1}{2}\left(\overline{u'^2} + \overline{v'^2} + \overline{w'^2}\right) \tag{5.10}$$

As a complementary quantification of turbulence, the coherent turbulent kinetic energy (CTKE) quantifies the energy telegraphed into the shear components of the turbulence stress tensor. The deviatoric of the Reynolds stress tensor plays a large role in wind energy as a significant contributor to turbine loads and a dominant contributor to turbulent energy fluxes in wind turbine wakes (Hamilton, Suk Kang, Meneveau, and Cal 2012; Ali, Hamilton, Cortina, Calaf, and Cal 2018). CTKE is defined as:

$$\text{CTKE} = \frac{1}{2}\left(\overline{u'v'} + \overline{u'w'} + \overline{v'w'}\right) \tag{5.11}$$

The strength of the turbulent shear in the atmospheric boundary layer is communicated through the local friction velocity, u_*, calculated from the turbulent velocity fluctuations measured by the sonic anemometers at each height as:

$$u_* = |\overline{u'w'}|^{1/2} \tag{5.12}$$

TKE is generated through a number of mechanisms and is typically associated with large-scale fluid motions and strong mean field gradients. Interaction between mean flow and terrain or other solid structures is responsible for mechanical turbulence production. Thermal gradients produce turbulence through buoyancy, and large-scale atmospheric motion leads to the turbulent mixing over geographic regions. Ultimately, the TKE generated at low frequencies is transferred through the turbulent spectrum through vortex interaction and is dissipated at high frequencies into heat through viscous dissipation. Interaction of turbulence at a range of scales is important for turbine design, as this influences the energy that is transferred into the turbine structure in terms of both aerodynamic performance and structural loads.

The integral length scale is an important quantification of turbulence, describing the length scale associated with the most energetic turbulent eddies in the flow. The integral length scale, (Λ), for a Cartesian component of a velocity vector is calculated from the time series of the turbulent velocity component. To arrive at the integral length scale, the temporal autocorrelation of a velocity component is calculated over a 10-min ensemble and normalized to provide the correlation coefficient. Integrating the correlation coefficient with respect to the time lag between observations provides the integral time scale, τ, of the observed velocity signal. Taylor's frozen field hypothesis is used to estimate the integral length by $\Lambda(u) = \overline{U} \cdot \tau(u')$. The integral length scale varies with height into the boundary layer and is on the order of magnitude as the measurement height. Accordingly, the characteristic time of flows at a turbine hub (around 80 m) and at rated speed [10 to 12 meters per second (m/s)] is approximately 10 s, which is easily resolved by the data acquisition system operating at 20 Hz.

the mean-squared difference between observations of the fluctuating velocity at a given separation in time δt:

$$D(\delta t) = \overline{[u'(t+\delta t) - u'(t)]}^2 \qquad (5.13)$$

Comparing the median value of the structure function to the cube root of the lag provides an alternate estimate of the strength of the turbulence along the met mast:

$$C_{v2}(\delta t) = \left[\frac{D(\delta t)}{(\overline{V}D(\delta t))^{2/3}} \right] \qquad (5.14)$$

from which the dissipation rate is estimated as:

$$\varepsilon = \left[\frac{C_{v2}}{2} \right]^{3/2} \qquad (5.15)$$

The dissipation rate is estimated from the inertial subrange of the turbulence spectrum by using $0.05 \leq \delta t \leq 2$, which corresponds to frequencies between 0.5 and 20 Hz at the NWTC.

5.3   Thermodynamic Properties of the Atmosphere

Thermodynamic exchanges between the atmosphere and the ground have a significant overall effect on the mean and turbulent flow fields from which energy is extracted by wind turbines. Most often, the thermodynamics of the atmospheric boundary layer are discussed in terms of thermal stratification or atmospheric stability. The stability profile in the boundary layer is quantified by the air temperature and humidity profiles. Absolute temperature, dew point temperature, and barometric pressure are measured at 3 m above ground, denoted as T_0, T_{d0}, and P_0, respectively.

The absolute temperature profile, $T(z)$, on the M5 tower is measured as the sum of the absolute temperature and temperature differences observed between different probe heights along the tower. Temperature measurements are compared at 3 and 26 m, 26 and 88 m, and 88 and 134 m above ground. Differential temperature measurements offer a higher accuracy by comparing multiple observations along the met mast. Differential temperature is accurate to approximately $0.1°$, whereas individual measurements of absolute temperature measurement offer a typical accuracy of $0.5°$.

Saturation vapor pressure, e_s, is calculated at each height from the air temperature, $T(z)$, in degrees Celsius through the empirical relationship:

$$e_s(z) = 6.11 \times 10^{[(T(z) \cdot A)/(T(z)+B)]} \qquad (5.16)$$

where $A = 7.5$ and $B = 237.3$ if $T(z) \leq 0°$ C, or $A = 9.5$ and $B = 265.5$ otherwise. The dew point temperature is used to calculate actual local vapor pressure, $e(z)$, from Eq. 5.16 rather than the absolute temperature.

The mass ratio of water vapor in the air is quantified through the specific humidity, q, and is calculated from the saturation and local vapor pressures using the empirical relationship:

$$q = 0.622 \frac{e}{P} \qquad (5.17)$$

20

where 0.622 is the ratio of the gas constants for dry air and water vapor, 287 J /kg K and 461.5 J /kg K, respectively. Virtual temperature, T_v, is written as:

$$T_v = T(1 + 0.61q) \tag{5.18}$$

The pressure gradient dP/dz is calculated from T_v and barometric pressure at the lowest probe height on the tower from the equation of state:

$$\frac{dP}{dz} = \frac{g \cdot P_0}{R \cdot T_v} \tag{5.19}$$

where g is gravitational acceleration (9.81 m/s^2) and R is the gas constant of dry air.

Pressure observed at other heights is collocated from the recorded barometric pressure and the pressure gradient as $P(z) = P0 + \Delta z \cdot dP/dz$. With the pressure profile in hand, the potential temperature, Θ, that is the temperature air at the ground would have if moved to a reference pressure level $P_{\text{ref}} = 100$ kPa and can be calculated as:

$$\Theta(z) = T(z)\frac{P_{\text{ref}}}{P(z)}^{R/C_p} \tag{5.20}$$

In Eq. 5.20, C_p is the specific heat capacity at constant pressure ($1{,}005$ J/kg K) and the ratio $R/C_p = 0.286$. Correcting for humidity, virtual potential temperature, Θ_v, is calculated as:

$$\Theta_v(z) = \Theta(z)(1 + 0.61q(z)) \tag{5.21}$$

where q is the specific humidity at each height from Eq. 5.17. Temperature, virtual temperature, and virtual potential temperature profiles are used in the calculation parameters that quantify the atmospheric stability.

5.4 Atmospheric Stability

Of the common methods to quantify stratification, the Monin-Obukhov length, L, is among the most frequently used and most successful in atmospheric science research. The Monin-Obukhov length is, in essence, a comparison of shear-driven turbulence to buoyancy-generated turbulence written as:

$$L = -\frac{u_*^3 \overline{\Theta_v}}{\kappa g \overline{w'\Theta_v'}} \tag{5.22}$$

Eq. 5.22 requires that a covariance be calculated from mean-centered fluctuations in the vertical velocity and instantaneous virtual potential temperature signals. The current work relies on co-located velocity and temperature observations from the sonic anemometers on the met masts to estimate $\overline{w'\Theta_v'}$. The time-averaged covariance of these signals is often referred to as the turbulent heat flux $\overline{w'\Theta_v'}$. By convention, the Monin-Obukhov length is often normalized by the height at which virtual potential temperature and velocity are measured, z (in this case the sonic anemometer height) to give the ratio $\zeta = z/L$. The atmospheric stability is then estimated as being locally convective when $z/L < 0$, and stable when $z/L > 0$. Neutral conditions occur when the shear-driven turbulence dominates contributions from buoyancy and $L \to \pm\infty$ (Table 3).

There are other methods used to quantify atmospheric stability, including the gradient Richardson number Ri:

$$Ri = \frac{g}{\Theta_v} \frac{d\overline{\Theta_v}/dz}{(d\overline{u_m}/dz)^2 + (d\overline{v_m}/dz)^2} \tag{5.23}$$

where the mean virtual potential temperature between two heights (z_1 and z_2) is $\langle \Theta_v \rangle = \frac{1}{2}[\Theta_v(z_1) + \Theta_v(z_2)]$. Here, Ri is calculated from 10-min average temperatures and vertical gradients of the wind velocity vector and Θ_v. These estimates rely on observations at multiple heights throughout the boundary layer and are considered to describe the atmospheric conditions between those heights.

The "speed" Richardson number, Ri_S, is also used to estimate atmospheric stability and considers only the gradient of the mean wind speed, U, rather than including directional shear, as in Eq. 5.23.

$$Ri_S = \frac{g}{\Theta_v} \frac{d\overline{\Theta_v}/dz}{(d\overline{V}/dz)^2} \tag{5.24}$$

Businger, Wyngaard, Izumi, and Bradley (1971) developed empirical relationships between the speed Richardson number and the Monin-Obukhov length. Under unstably stratified conditions $z/L \approx Ri_S$. Ri_S approaches a constant and finite value as $z/L \to \infty$:

$$Ri_S = \begin{cases} 0.74\zeta \frac{(1+15\zeta)^{1/2}}{(1+9\zeta)^{1/2}} & \text{if } Ri_S < 0 \\ 0.74\zeta \frac{(1+6.35\zeta)^{1/2}}{(1+4.7\zeta)^{1/2}} & \text{if } Ri_S > 0 \end{cases} \tag{5.25}$$

Several classes of atmospheric stratification are designated in Table 3, defined using both the Richardson number and Monin-Obukhov length. Note that the Monin-Obukhov length, L, is used directly in the classification rather than the normalized stability parameter ζ. Limiting values of both Ri and L are derived from previous work relating the operation of utility-scale wind turbines to various stability classes (Wharton and Lundquist 2012; Barthelmie and Jensen 2010). Garratt (1994) specifically identified a correlation between the very stable regime and production of CTKE. In the very stable regime, where $Ri > 0.25$, the buoyancy term in the Navier-Stokes equations acts as a sink of TKE. Similarly, in the strongly unstable regime, this same term acts as a source of TKE. A range of L has been used by different authors to define neutral conditions. Considering flow at the hub height of a typical wind turbine (say $z = 80$ m for the GE 1.5 MW at the NWTC), the relationship between Ri and L can be deduced from Eq. 5.25.

Table 3. Stratification Classes Using Richardson Number and Monin-Obukhov Length

Stratification	Ri	L
Very stable	$Ri \geq 0.25$	$-200 < L < 0$
Stable	$0.01 < Ri \leq 0.25$	$-500 < L < -200$
Neutral	$\lvert Ri \rvert \leq 0.01$	$\lvert L \rvert > 500$
Unstable	$-0.01 < Ri \leq -0.25$	$500 < L < 200$
Very unstable	$Ri < -0.25$	$200 < L < 0$

6 Review of Atmospheric Conditions

Atmospheric conditions at the NWTC share many characteristics with the Front Range of the Colorado Rockies, combining high elevation, midlatitude, and interior continental geography. The resulting climate is typically cool and dry with large seasonal and diurnal swings in temperature and wind conditions. Summer months are characterized by hot days and reduced wind speeds, often punctuated by afternoon thundershowers. The high wind season at the NWTC is largely associated with the winter months, typically beginning in October and persisting though April.

Due to the particular location of the NWTC, atmospheric conditions can vary considerably depending on the flow direction. The prevailing wind direction overall is generally from the west, with the strongest winds associated with flows that come off the mountains, channeled through Eldorado Canyon, which forms a gap in the Front Range and directs winds toward the NWTC. Throughout the year it is not unusual to see wind speeds on the order of 9–15 m/s from the west, although winds at these speeds become less consistent and less frequent during summer months. Figure 13 shows a wind rose and a turbulence intensity rose generated from 10-min averaged data from a sonic anemometer near the top of the M5. No filtering beyond the QC process described in Section 4.2 was applied to the data, yielding an overall view of the winds at the NWTC. The wind rose in Figure 13a demonstrates that wind speeds greater than 9 m/s come almost exclusively from the west and that wind speeds below 6 m/s are more frequently observed from the north or south. Turbulence intensity shown in the TI rose in Figure 13b is more evenly distributed than wind speed. It is possible to see high TI from any direction, although the most frequent observations remain from the west.

(a) Wind rose at 122 m   **(b) TI rose at 122 m**
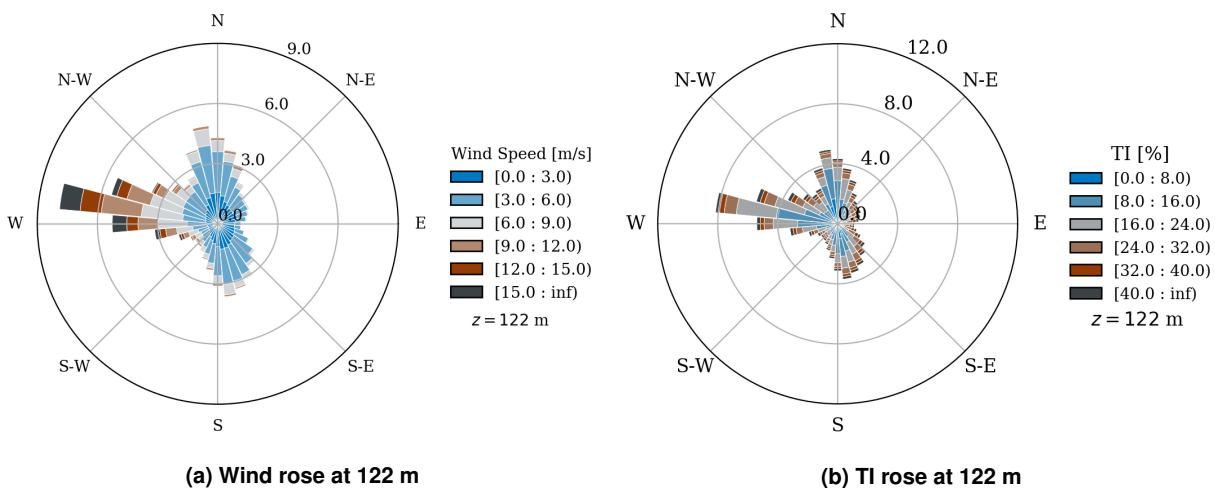
Figure 13. NWTC wind and TI roses from the top of M5

Wind and turbulence intensity roses are provided in the following figures only at selected probe locations, for brevity. The authors have made the codebase used to read met mast data and generate figures available for general use at https://github.com/NREL/MetMastVis. Interested parties are encouraged to explore the M5 data record and generate particular visualizations of interest at any probe height along the met mast.

Figure 14 shows wind direction and variability for instruments located at 3 m and 87 m, corresponding to the measurements closest to the ground and hub height of the GE wind turbine. These heights were selected for data availability and to show the range of behaviors across the height of the measurement domain. It should be noted that when the wind is generally from the east or south, the instrumentation on the met masts may

be affected by the presence of wind turbines onsite or by the tower itself. Data from these sectors have not been excluded in order to demonstrate a more complete picture of the atmospheric behavior at the NWTC, but results pertaining to easterly or southerly winds are expected to carry additional uncertainty.

Previous work documenting the site conditions at the NWTC (Clifton and Lundquist 2012) used a K-means clustering algorithm to divide the atmospheric flows into four categories: southerly, northerly, weak westerly, and strong westerly flows. This report aims to provide context on the atmospheric conditions at the NWTC in a way that is easily interpreted by researchers and wind turbine original equipment manufacturers interested in work at the NWTC. The following sections detail the flow in a cumulative sense, without any a priori sorting or filtering, and later endeavors to distinguish features and trends in the atmospheric resource by daily, monthly, or seasonal trends and conditions distinguished by stability class.

The NWTC is classified according to the IEC (2005) standards as a Class I_A for wind turbine testing, with peak 50-year wind speeds at more than 50 m/s and TI greater than 16% recorded at a wind speed of 15 m/s. The NWTC is further distinguished as a special case due to the frequency of rapid changes in flow conditions. Although the NWTC is denoted a Class I_A site, during much of the year wind speeds and turbulence are lower, making the NWTC a viable site for validating the performance of Class II and Class III turbines. A review of extreme events delineated by the IEC standards is provided in Section 7. Raw data recorded at 20 Hz are used for identification and characterization of extreme events, given that most IEC extreme events occur on a timescale of 6–12 ss. Raw data are not subjected to the QC protocol described in Section 4.2 but are validated in a separate process described in Section 7. Low-turbulence conditions are also isolated from the full set of observations due to the interest they hold for wind turbine validation work. Here, low turbulence is considered to be any set of observations where the TI at hub height (87 m) is less than 10%.

(a) Wind rose at 87 m

(b) TI rose at 87 m

(c) Wind rose at 3 m

(d) TI rose at 3 m
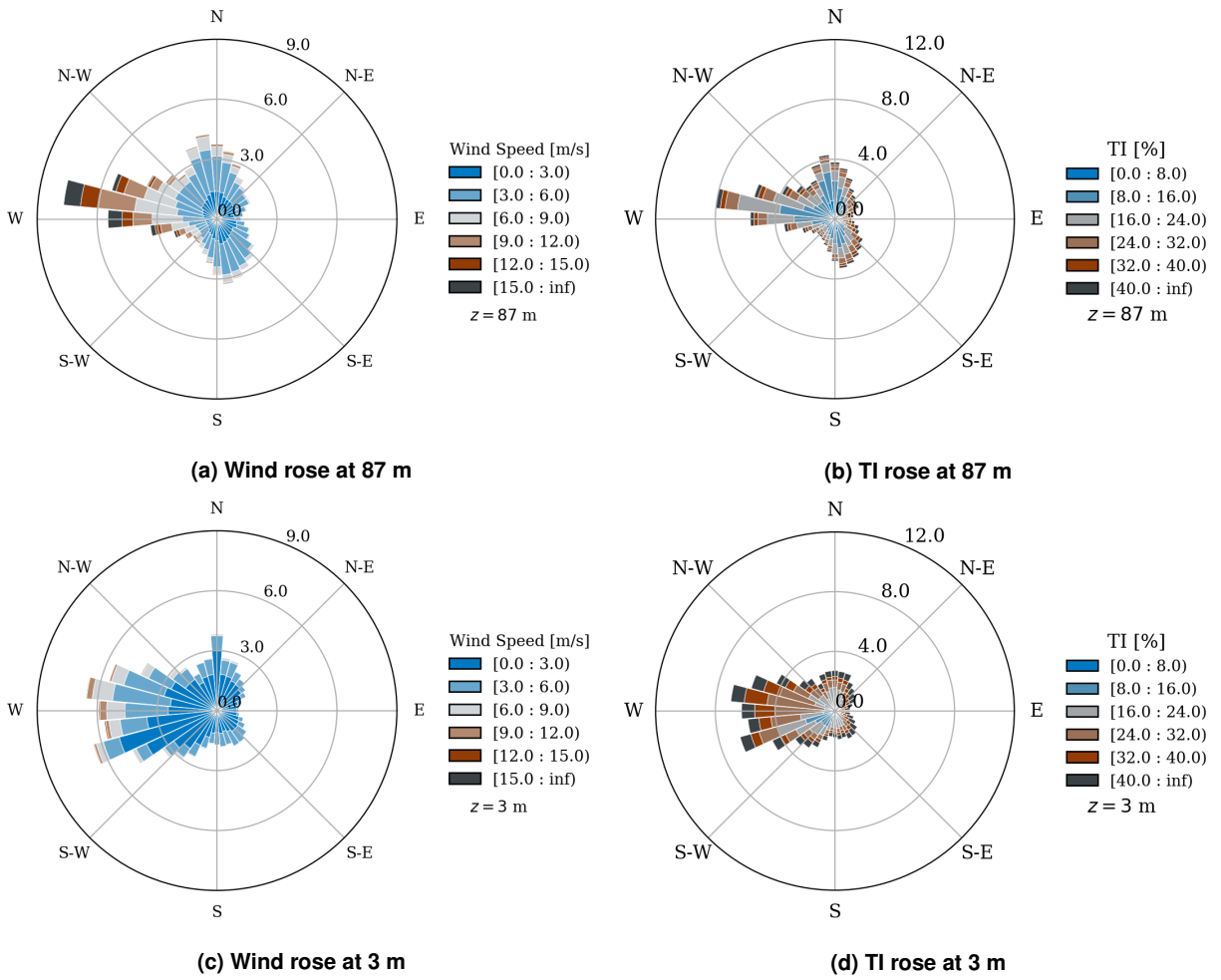
Figure 14. Wind and TI roses at stations nearest the ground (3 m) and hub height (87 m) of M5

6.1 Cumulative Atmospheric Conditions

The atmospheric conditions at the NWTC are subject to strong diurnal and seasonal variations, detailed in Sections 6.2 and 6.3. What follows is a top-down look at the conditions at the NWTC *without* accounting for sources of variation, either known a priori or deduced through statistical exploration of the information channels produced by M5. The term "cumulative" is applied to any quantification or visualization that includes observations to the full time range of data collected from the met mast included in the current report (March 2012–December 2018). It should be noted that data collection from M5 is ongoing and that the results discussed here may not reflect the most recent events. Additionally, no data were excluded from the current analysis based on the wind direction sectors that may include influence of the met mast structure or neighboring wind turbines (Section 2.2). If met mast instrument data are used for further analysis, additional steps should be taken to account for uncertainty added to data channels from the identified sectors.

Cumulative distribution of wind speed and direction (shown in Figure 15) are composed from a cup anemometer and wind vane at 87 m. The histograms in Figure 15 essentially combine the information contained in Figure 14a separated onto multiple axes. The wind speed distribution shown in Figure 15a shows the frequency of observation of a given wind speed binned to 0.5 m/s, without regard to wind speed or direction. Many of the wind speed histograms are shown with a two-parameter Weibull distribution,

$$F(V) = 1 - \exp\left[-(V/A)^k\right] \tag{6.1}$$

where the scale and shape parameters (A and k, respectively) are sought through least-squares error minimization. Fitting a Weibull distribution to the histogram of cumulative wind speeds yields a shape factor of 1.44 and a scale parameter of 5.6. The wind direction indicates the relative frequency of observations made at 87 m in a particular wind sector, here divided into 36 bins of $10°$ each. The three regions of increased observation frequency correspond to the west, north, and south in decreasing order. Wind speeds are tabulated for each quarter of the year in Figure 16 to illustrate the season variability of the site. Elevated winter wind speeds are evident in the thicker high wind speed tails for Q1 and Q4.

(a) Wind speed at 87 m

(b) Wind direction at 87 m
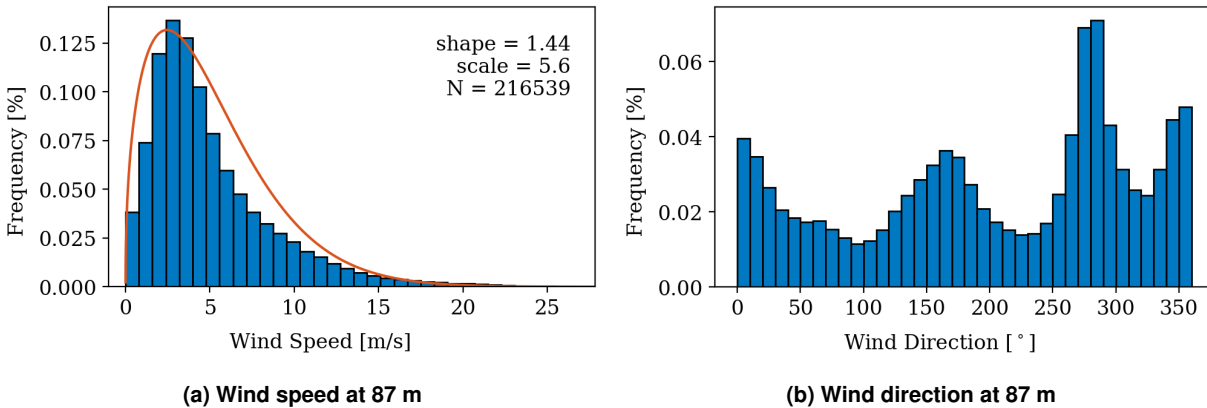
Figure 15. Wind speed and direction data from the sonic anemometer at 87 m

Atmospheric quantities for the cumulative set of observations are shown in Figure 17, including the air density, barometric pressure, and potential temperature. Atmospheric quantities have been fit against a skewed Gaussian distribution following the formulation:

$$f(x; A, \mu, \sigma, \gamma) = \frac{A}{\sigma\sqrt{2\pi}} e^{-(x-\mu)^2/2\sigma^2} \left(1 + \mathrm{erf}\left(\frac{\gamma(x-\mu)}{\sigma\sqrt{2}}\right)\right) \tag{6.2}$$

26
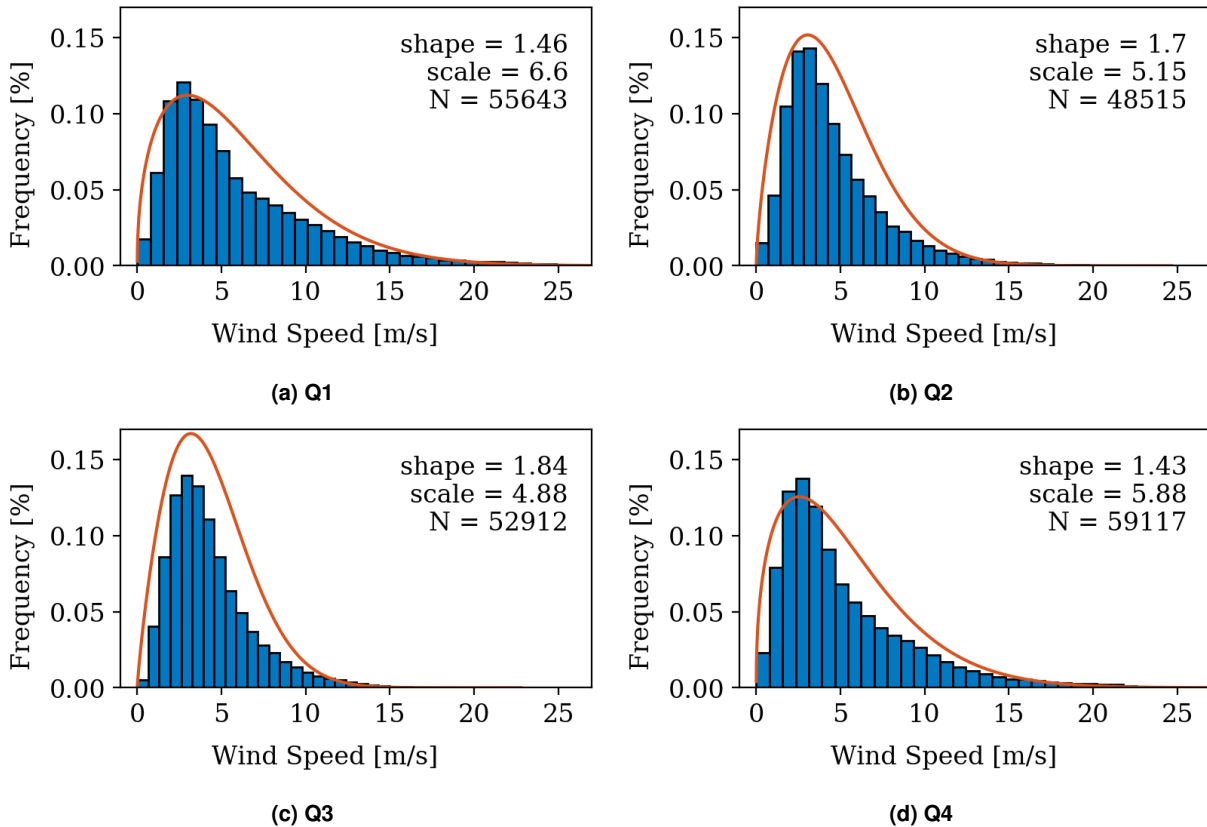
Figure 16. Wind speed distribution by quarter

Model parameters A, μ, σ, and γ correspond to the amplitude, mean, standard deviation, and skewness of the fit and are supplied in the figures, where appropriate. As shown in Figure 17a, the air density has a distribution that is slightly positively skewed, with the tail to the right decreasing more gradually. In contrast, the air pressure and temperature both show negatively skewed distributions. In the case of air temperature in Figure 17c, observations below the mean of 20.4° C are distributed over a larger range, extending below -20° C, whereas observations above the mean fall off relatively quickly.

It should be noted that there was a period of questionable calibration for the air pressure signal from December 2014 through May 2015. During that period, an alternate pressure transducer was used in the data acquisition system that had a different range of operation and required a different numerical offset for correct operation. Because the pressure at all heights along the met mast is derived from the pressure tap at 3 m, an offset in the calibration at that station affected all pressure signals identically. The offending data have been modified in all results presented here by adjusting the signal offset by a constant value. The offset was calculated in order to ensure that the mean pressure period from December 2014 through May 2015 matches with the mean pressure for the respective time period from the rest of the data history.

Wind shear and veer are shown in Figure 18, calculated between observations at 3 m and 122 m along the met mast. These particular instrument stations were selected as covering the greatest separation distance, and thus providing the most extreme observations of shear and veer. Data for wind shear and wind veer are available between different stations but are not included here for brevity. The interested reader is referred to the online met mast data and visualization tools.

27

(a) Air density observed at 122 m

(b) Atmospheric pressure observed at 122 m

(c) Air temperature at 122 m
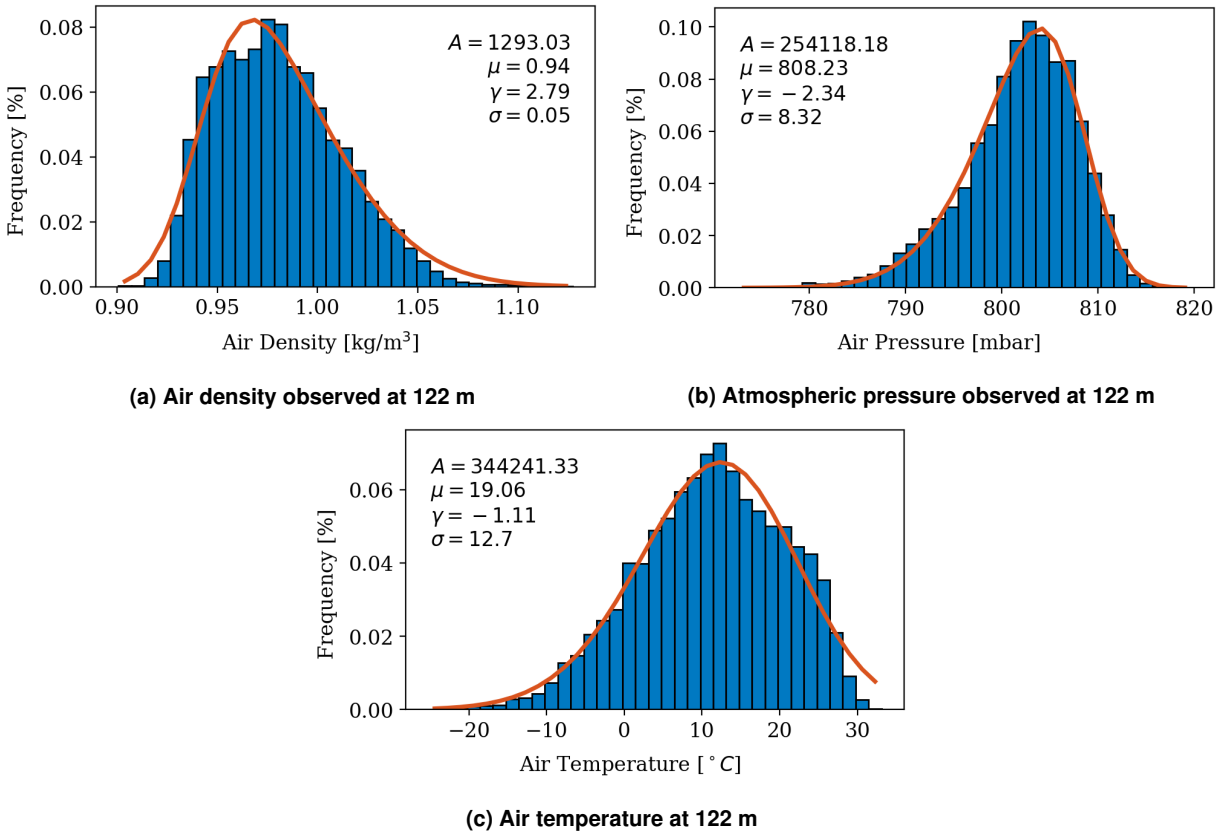
Figure 17. Bulk atmospheric data from M5

Wind shear shown in Figure 18a has a distribution largely concentrated in the range of $0.05 \leq \alpha \leq 0.4$. Nearly 92% of wind shear observations occur within this range, taking a mean value of 0.19 and a standard deviation of 0.14. These values line up fairly closely with the IEC standard value of wind shear ($\alpha = 0.2$). The tails of the distribution of α are quite flat, indicating that extreme shear conditions are relatively infrequent. Integrating the histogram where $\overline{\alpha} - \sigma_\alpha < \alpha < \overline{\alpha} - \sigma_\alpha$ (greater than one standard deviation from the mean) leaves only 9% of the total observations.

Wind veer between 3 m and 122 m is more symmetrically distributed than shear. In the northern hemisphere, the anticipated wind veer is considered to be a positive value, where positive values increase with measurement height, but this is highly dependent on the site and local thermal gradients (Clifton 2014).

6.2 Hourly Trends

The cumulative conditions described in Section 6.1 provide only a broad overview of atmospheric behavior at the NWTC. In reality, the atmospheric conditions at the NWTC are subject to strong diurnal and annual cycles. The following figures endeavor to demonstrate daily trends in bulk atmospheric and thermodynamic quantities recorded by M5.

6.2.1 Atmospheric Quantities

(a) Wind shear observed between 38 m and 122 m by M5

(b) Wind veer observed between 38 m and 122 m by M5
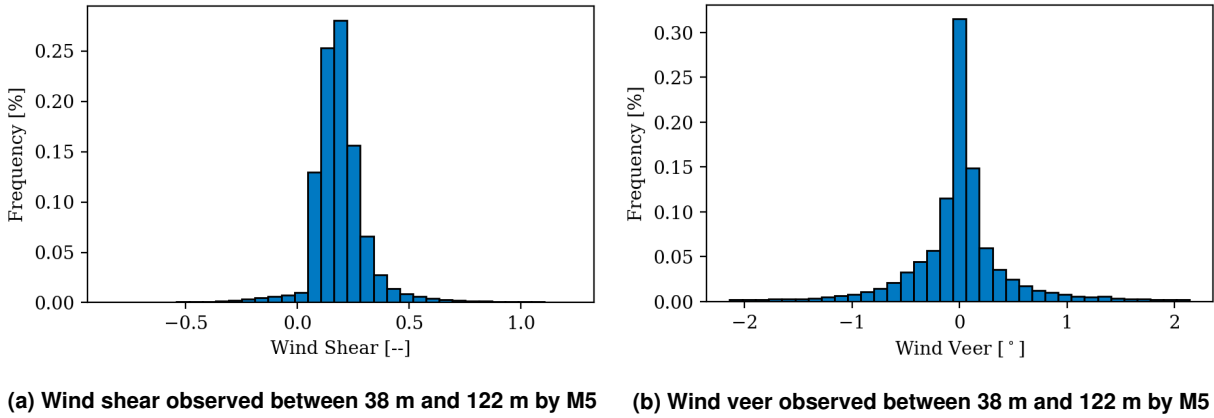
Figure 18. Cumulative wind shear and veer distributions

Daily averaged wind speed and direction are shown in Figure 19 and demonstrate clear periodic trends. The wind speed, shown at all heights along M5, ramp up beginning around 7:30 a.m. At lower probe heights, the ramp lasts only until mid-day, where peak daily average wind speeds are just over 3.1 m/s. Higher along the met mast, the wind speed continues to ramp up until mid-afternoon. This trend is largely influenced by distinct behavior seen in the fall months (discussed more in Section 6.3).

Wind direction in Figure 19b shows great agreement all along the met mast. Throughout the night, daily averaged winds at the NWTC are recorded as coming from the southwest, moving toward the S during the middle of the day. The shift in direction in the mid-morning occurs quite quickly, shifting by as much as $90°$ in about 4 hours. In the afternoon, the shift back to the southwest direction sector occurs over 9–10 hours. Instruments located at or below 61 m on the tower observe a distinct transition around 7 p.m. where the wind direction levels off to about $240°$. Again, the average daily trend in wind speed and direction do not communicate the full range of time dependence at the NWTC. A more complete picture of the atmospheric conditions merits a review of seasonal variations.

(a) Hourly average wind speed trends

(b) Hourly average wind direction trends
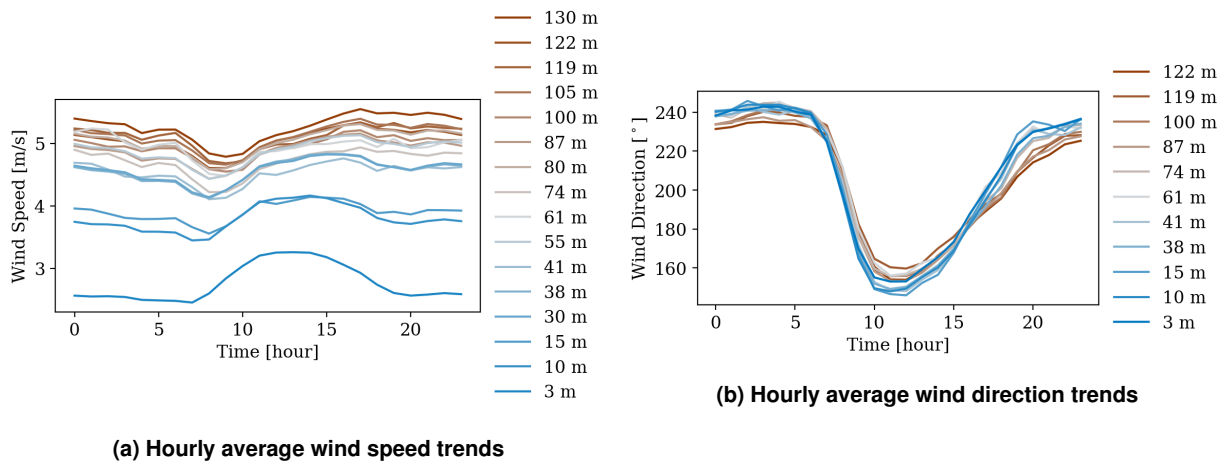
Figure 19. Average daily bulk flow speed and direction

Thermodynamic properties of the atmosphere are largely regulated by the presence and absence of solar

radiation as a source of energy. The most intuitive demonstration of this is that the air temperature (Figure 20a) increases beginning around 6 a.m., especially at stations near to the ground. The daily averaged temperature measurement at 3 m shows the greatest change in extremes, from 6.5° C to 13 ° C, and is most influenced by the temperature of the ground itself. At greater heights above teh ground, the air temperature varies less, although the diurnal cycle is still clearly visible.

Variations in the air temperature are the driving mechanism behind the changes in air density shown in Figure 20b. As the air increases in temperature until early afternoon, the air density drops until a minimum that depends on height above the ground is reached around 2 p.m. As with the temperature, the most extreme changes in air density occur near the ground, where the difference in the maximum and minimum daily averaged air density is around 20 g/m^3.

Daily averaged observations of air pressure show different behavior than temperature and density. There is less variation in the daily averaged air pressure, and there appears to be two periods of variation during the daily cycle. Trends in air pressure follow the absolute value of the gradient of air temperature; when daily averaged temperature is changing the most quickly (either increasing or decreasing), the air pressure reaches a local maximum. Conversely, when the air temperature is at its respective extremes, the daily averaged air pressure is at its minimum.

(a) Hourly average air temperature trends

(b) Hourly average air density trends

(c) Hourly average air pressure trends
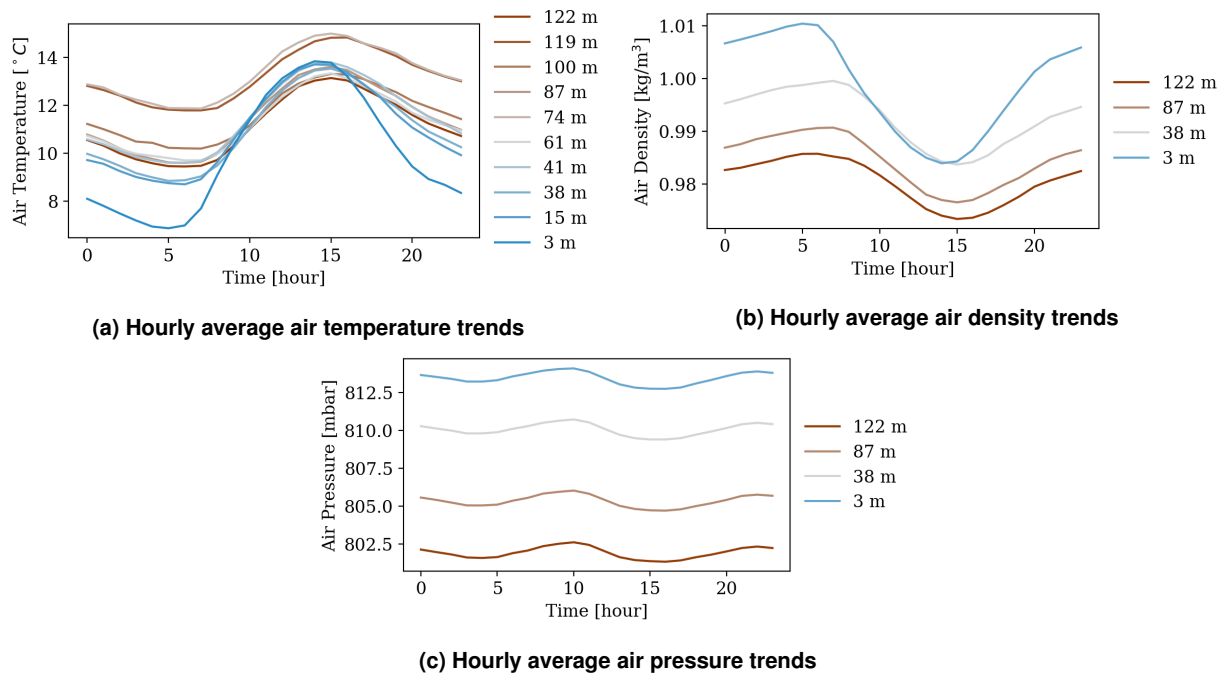
Figure 20. Bulk atmospheric conditions

6.2.2 Trends in Atmospheric Stability

Stability is a powerful descriptor of the overall atmospheric character and is a key factor in wind turbine wake dynamics. Atmospheric stability is largely governed by temperature gradients vertically from the ground; when the temperature increases with height, the atmosphere is considered to be stably stratified, and when temperature decreases with height, it is considered to be unstably stratified. Gradients in temperature appear

in the Navier-Stokes equations as a source (or sink, for stably stratified flow) of TKE. Here, atmospheric stability is quantified through the Monin-Obukhov length scale, L, calculated at several stations along the height of M5, shown in Figure 21a.

Recalling the comparison of atmospheric stability classifications in Table 3, one can see that the daily averaged trends in Monin-Obukhov length delineate a regular period change from strongly stable to strongly unstable conditions and back each day. During the night, the daily averaged temperature of the air increases with height of observation, reflected by the relatively high values of L; daytime hours show the opposite trend. L compares the relative contributions to TKE from mechanical shear production to those of buoyant production. Thus, when the buoyant contributions are negligible compared to the mechanical contributions as for neutral conditions, $L \to \pm\infty$. Conversely, when the buoyant contributions to the TKE are dominant, $L \to 0$, where the sign of L is determined by the sign of the temperature gradient.

(a) Hourly average Monin-Obukhov length

(b) Cumulative trends in atmospheric stability by hour of day
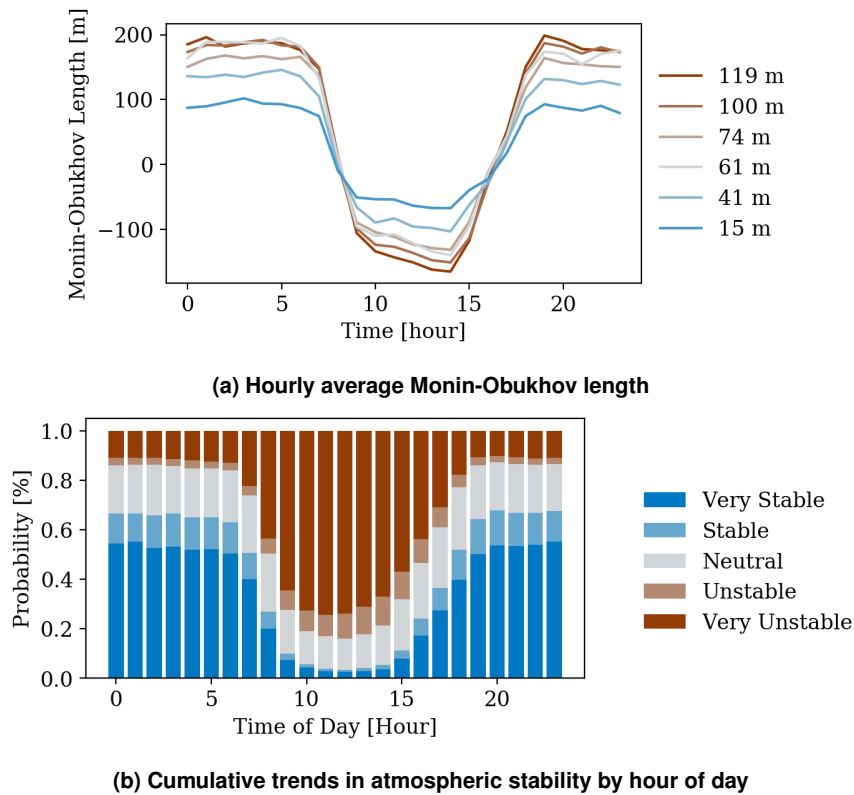
Figure 21. Atmospheric stability trends over the average diurnal cycle

Figure 21b shows a normalized daily averaged histogram of the stability class observed at the NWTC. The figure draws data from L calculated at 74 m. Each bar in the figure indicates the likelihood of observing a particular stability condition during a specific hour of an average day at the NWTC. The figure indicates that atmospheric stability is dominated by very unstable conditions between the hours of 9 a.m. and 4 p.m. Nighttime conditions are slightly more evenly distributed, but are are more likely to be classified as stable or very stable, representing approximately 65% of the cumulative observations.

Given that both wind speed and atmospheric stability exhibit strong daily variations, it is to be expected that they show some correlation. Figure 27 shows wind speed profiles against probe height distinguished by stability class. The profiles indicate that in a general sense, lower wind speeds are expected to be correlated

with unstable conditions and higher wind speeds with stable conditions. The observed wind shear also varies with stability. Increased TKE is seen during unstable conditions (buoyancy acts as a source of TKE), which leads to increased mixing throughout the ABL and less variation of wind speed with vertical position.
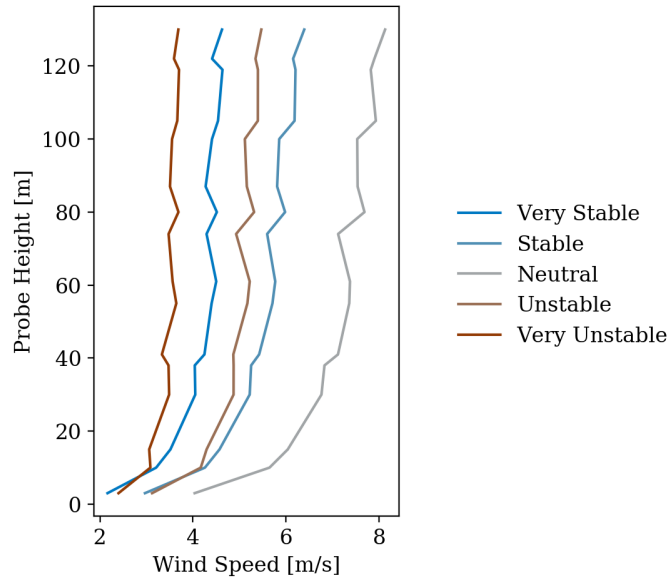
Figure 22. Profiles of wind speed along M5 separated by stability class

6.2.3 Turbulence

Influence of the buoyant contributions to the overall energy balance is seen in the daily averaged trends of TKE and CTKE. Unstable periods between 9 a.m. and 4 p.m. are associated with an increase of TKE peaking around 1:30 p.m. TKE and CTKE require high-frequency observations of the wind velocity vector, and thus are available only from the sonic anemometers. CTKE is smaller in magnitude matching with boundary layer theory, from which one would expect the Reynolds stress tensor to be dominated by the diagonal elements, especially the autocovariance of the streamwise velocity fluctuations. The CTKE also shows a greater dependence on probe height than the TKE. The shear terms of the Reynolds stress tensor are expected to be more evenly distributed through the boundary layer than the Reynolds normal stresses and reach maxima further from the ground.

Other turbulence quantities of interest that are within reach of the measurement system on M5 include turbulent fluxes of heat and momentum. Both quantities correlate directly with the diurnal evolution of the atmospheric flow and changes in stability. Turbulent flux of momentum (Figure 24a) is typically associated with the Reynolds shear stress derived from velocity fluctuations in the streamwise and vertical directions $\overline{u'w'}$. This covariance is important to wind turbine wake physics and is a large contributor to turbulent transport phenomena that are part of wind turbine wake recovery. Turbulent heat flux (Figure 24b) is quantified through the covariance of vertical velocity fluctuations and variations in the local temperature field. The daily trend of mean heat flux indicates that heat is moved toward the ground during the night, when $\overline{w'\Theta'_v} < 0$, and that during the day turbulent mixing moves heat from the ground into the atmosphere, in agreement with the diurnal trend of stability shown in Figure 21b.

(a) Hourly average turbulent kinetic energy

(b) Hourly average coherent turbulent kinetic energy
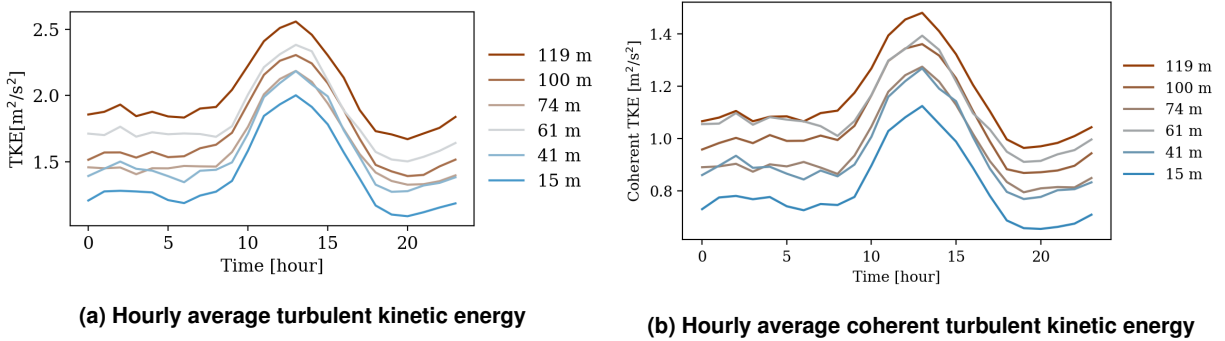
Figure 23. Average trends of energy within the turbulence observed by M5

(a) Hourly average momentum flux

(b) Hourly average heat flux
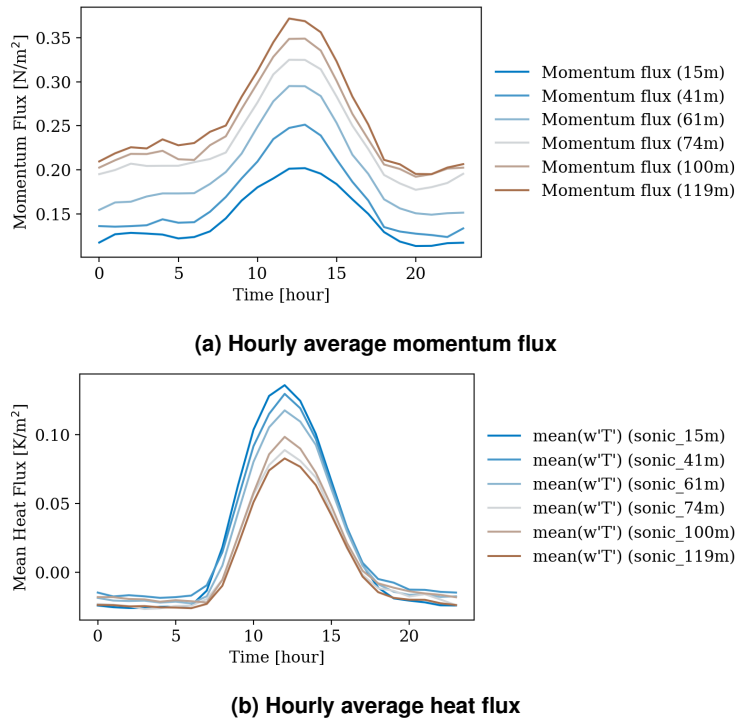
Figure 24. Average daily momentum and heat flux trends

6.3 Monthly Trends

Atmospheric conditions at the NWTC are subject to strong seasonal or annual variation. Taking both the annual and diurnal cycles into account offers a more complete view of the flow behavior onsite. Figure 25 shows that both the time of year and time of day are key predictors in the overall picture of atmospheric stability. The months from December to February show that the occurrence of unstable or very unstable conditions is much less common during the winter. They also indicate that the likelihood of observing neutrally stratified flow conditions are significantly increased. In contrast, the period from April to September shows relatively few contributions of observations during neutral conditions. During the day, the spring, summer, and autumn months exhibit very few observations of stable or strongly stable atmospheric conditions.
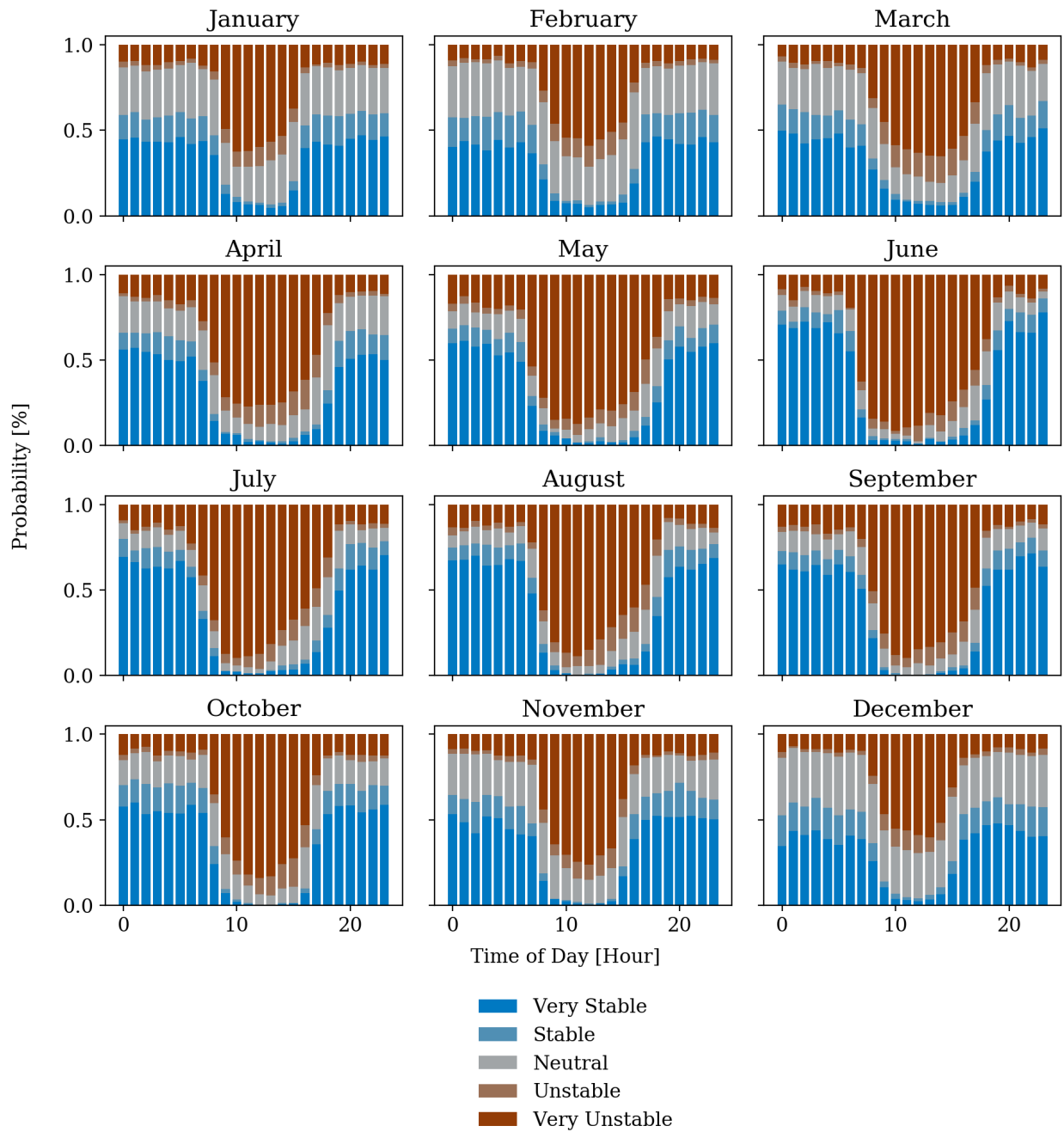
Figure 25. Monthly trends in atmospheric stability by hour of day

Variations in wind speed also follow a distinct cycle over the calendar year (see Figure 26). Winter months indeed show higher average wind speeds (ranging from 3–7 m/s) than in the summer months (2–5.5 m/s) and are also much more consistent. The daily averaged wind speed at 3 m above the ground shows an increase in wind speed beginning mid-morning and ending mid-afternoon (shown as a hump in the darkest blue line). From June to September, there is a distinct ramp in wind speed seen at higher instrument locations during the daytime hours. This sharp increase in wind speed is not evident in other months (October–April); rather,

the wind speeds are much more consistent throughout the day.
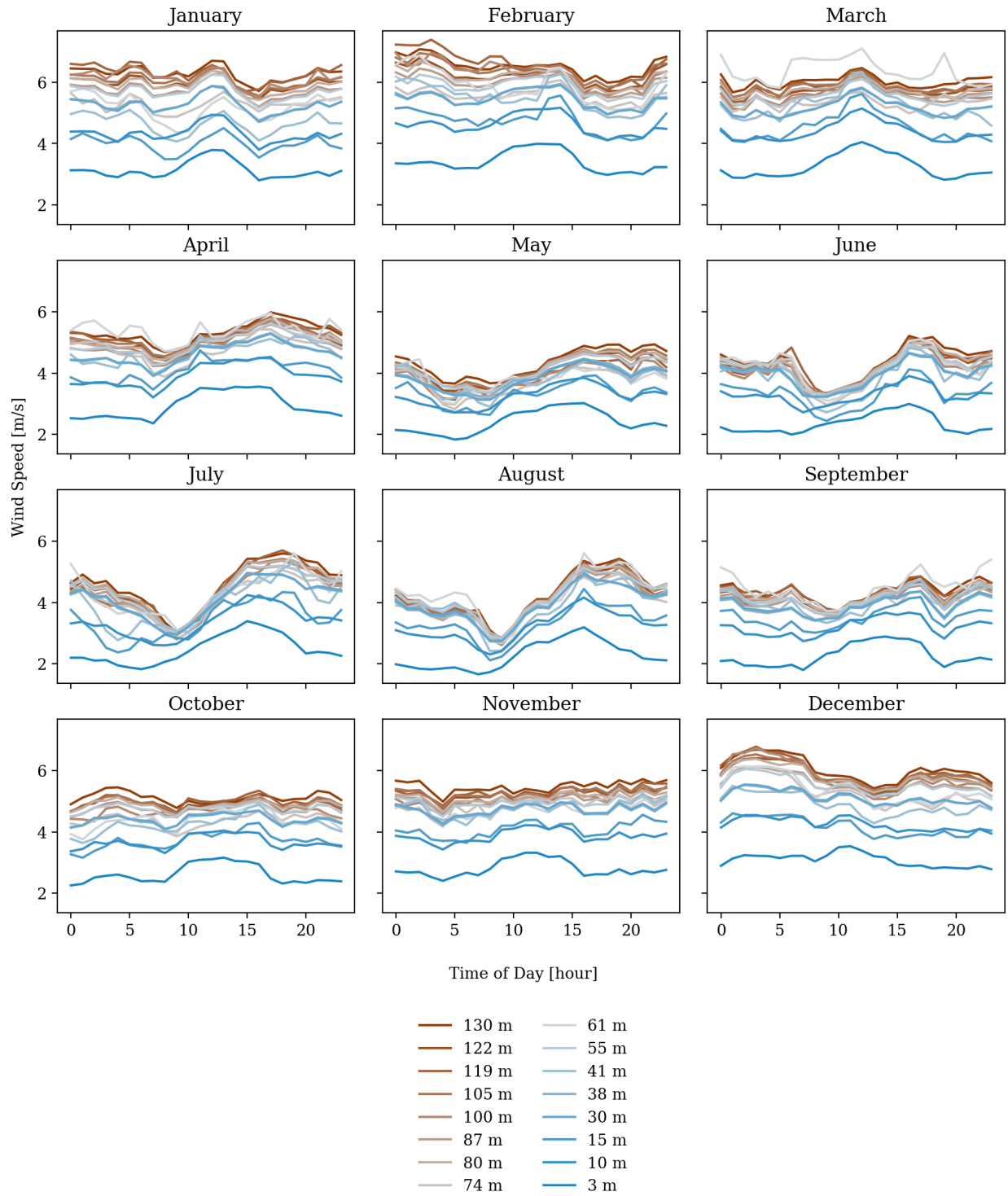
Figure 26. Average daily wind speed by month at each probe height
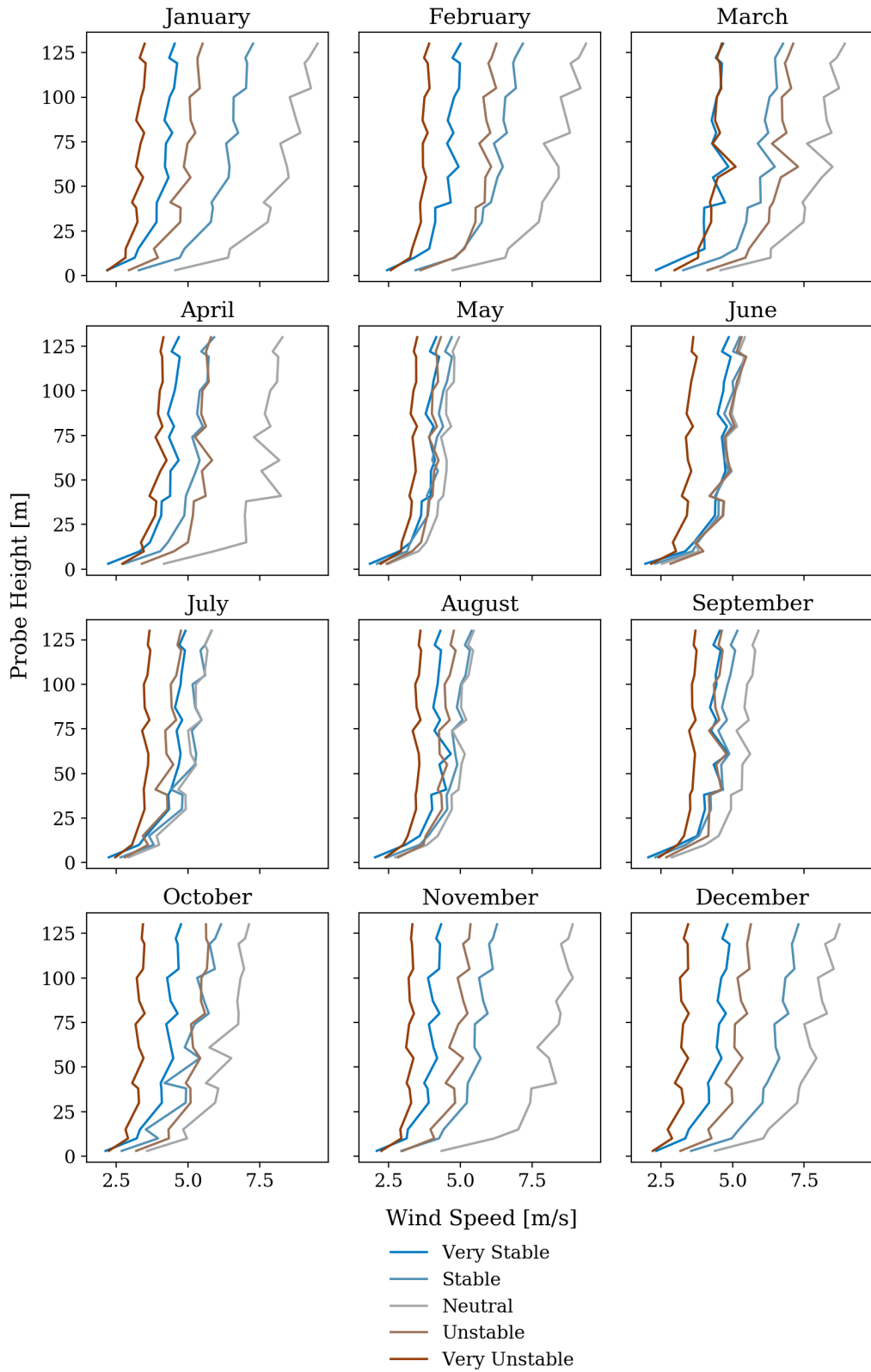
Figure 27. Profiles of wind speed along M5 for each month separated by stability class

Adding the consideration of atmospheric stability to the annual variation in wind speeds at the NWTC shows a further level of distinction between the windy and calm seasons. Figure 27 shows mean wind speed profiles recorded along M5 grouped by the month of observation and the atmospheric stability at the time of each record. The figure indicates that stability is not necessarily a relevant factor in the mean wind speed profile, with the exception of very unstable conditions where wind speeds are lower in general. The windy season from October to April shows consistent wind speed behavior according to stability conditions. In each month, the wind speeds are greatest during neutrally stratified conditions, corresponding with the expectation that mechanically driven turbulence dominates contributions by buoyancy.

The distribution of wind direction recorded by M5 also shows strong dependence on the annual cycle and atmospheric stability (see Figure 29). Most notably, the strongest winds, those coming through Eldorado Canyon, are most prevalent in the windy season and are also the most frequent instances of stable and very stable conditions. Unstable and very unstable conditions during fall and winter months are most likely to come from the north or south, arising from weather patterns that follow the Front Range. The wind direction during the summer months is much more uniformly distributed throughout all wind direction sectors and stability classes. Figures 30 and 31 combine wind speed and direction information sorted by month. Wind roses drawn for each month make it clear that high wind speeds at the NWTC are only really observed during the winter months and are from the west. For example, during January approximately 8% of the total observations at 87 m are from between 280° and 290° and above 9 m/s. The TI roses in Figure 31 indicate that most of the observations of the wind resource at NWTC correspond to high turbulence conditions. Approximately 72% of recorded observations of TI are above the IEC standard of 16% for a Class I_A site. Conditions of low turbulence are of particular interest for wind turbine testing and are discussed at length in Section 6.4.
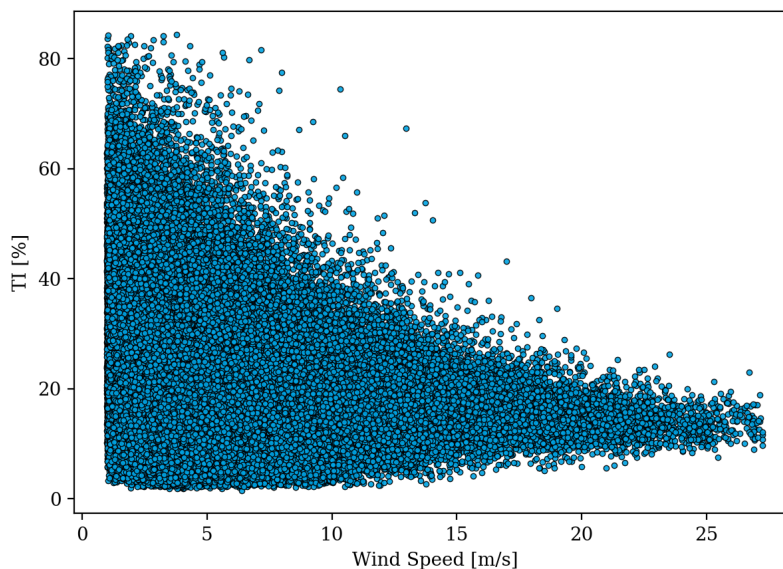
Figure 28. Distribution of speed against TI observed at 87 m
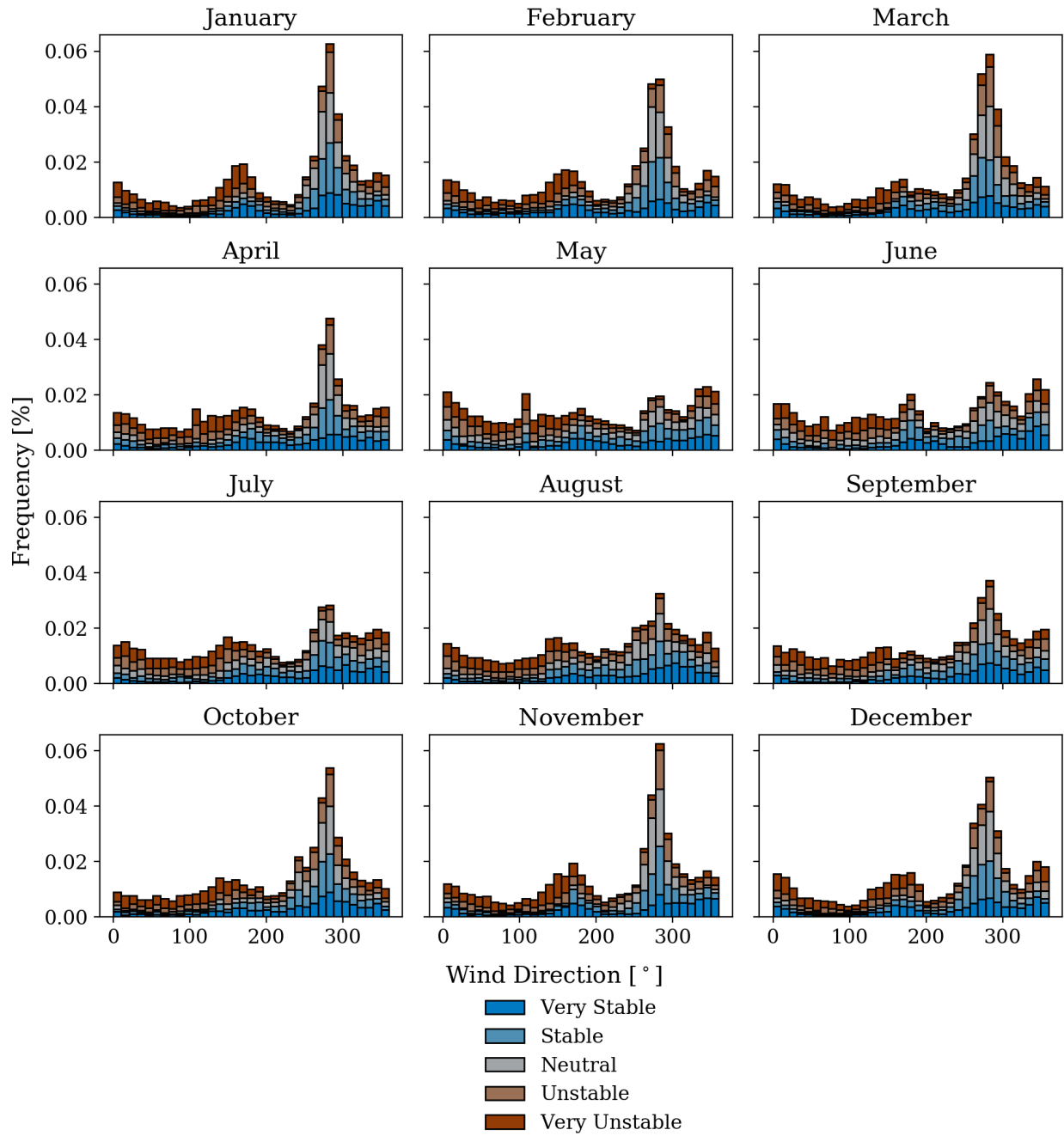
Figure 29. Histogram of wind direction by month at each probe height separated by atmospheric stability condition
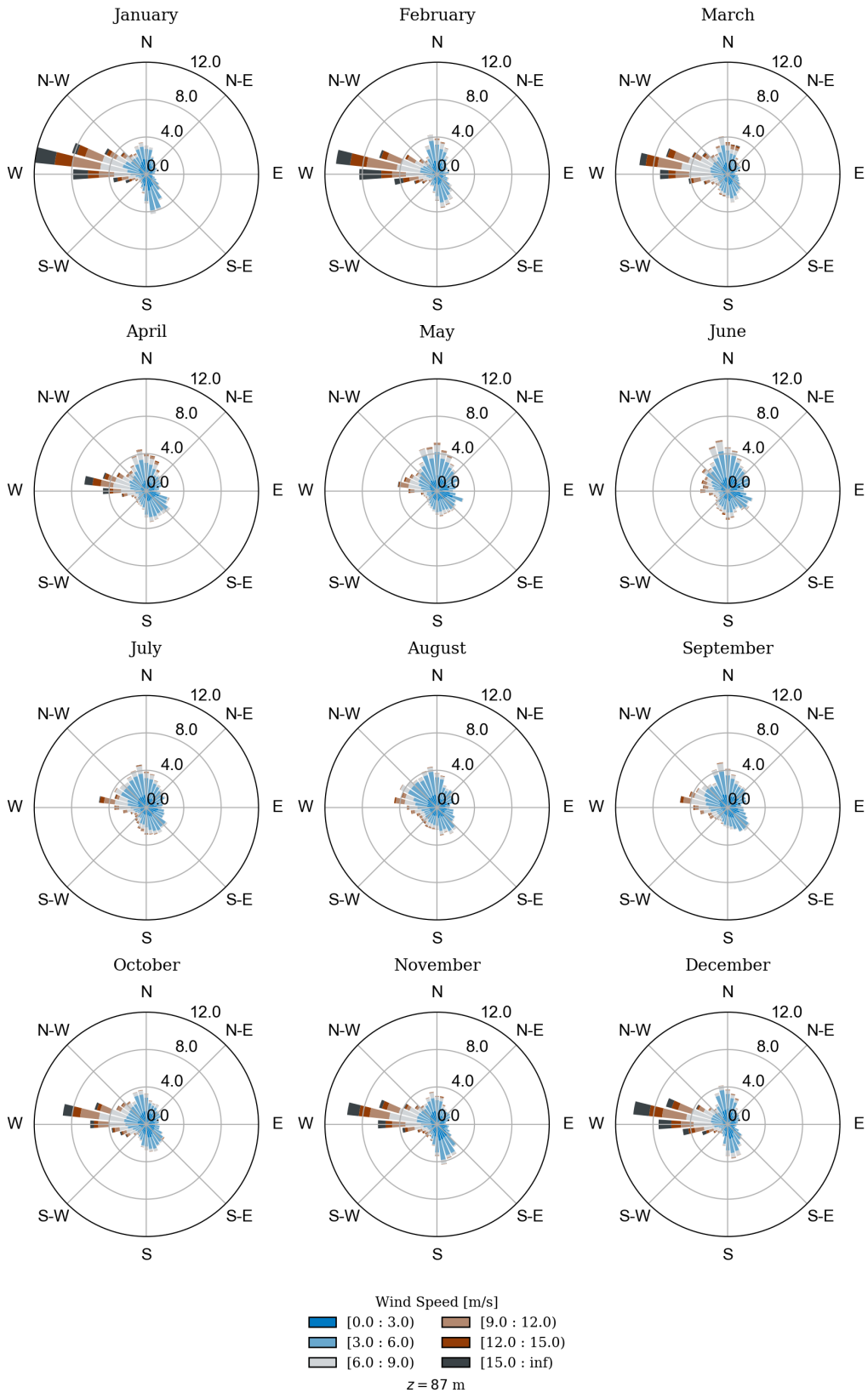
Figure 30. Wind rose by month from atmospheric data at 87 m
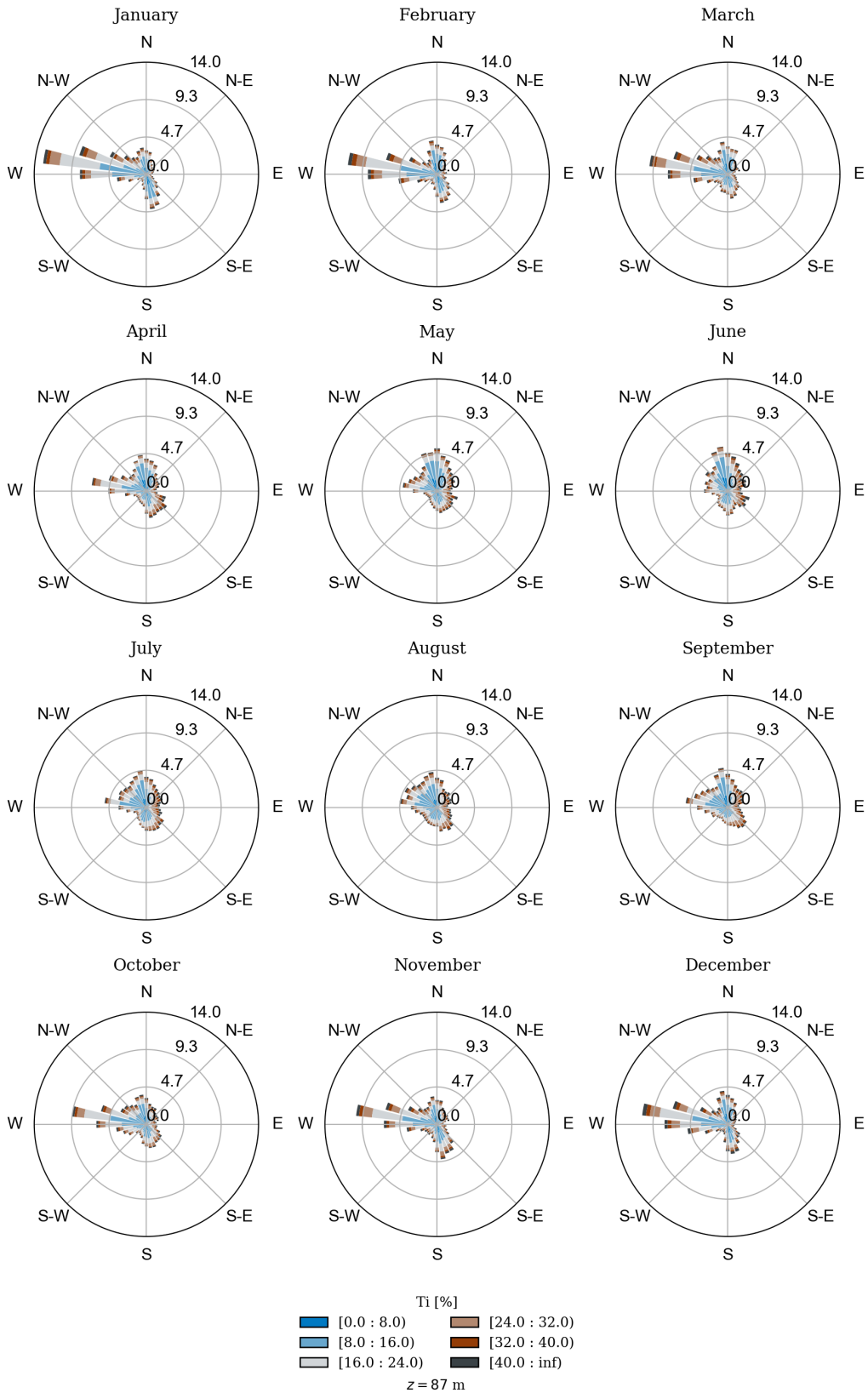
Figure 31. TI rose by month from atmospheric data at 87 m

6.4 Low-Turbulence Conditions

Periods of low turbulence ($TI \leq 10\%$) are relatively infrequent at the NWTC, but represent an attractive range of conditions for testing and validation of wind turbine design and performance. Characterization of the low-turbulence periods at the NWTC is explored in the following section, beginning by identifying the bulk atmospheric conditions that correlate with low turbulence and under what conditions they are likely to occur. Figures 32 and 33 demonstrate trends of turbulence each day of the year, averaged over the 144 10-min bins per day for the 6 years of collection at the M5 tower.
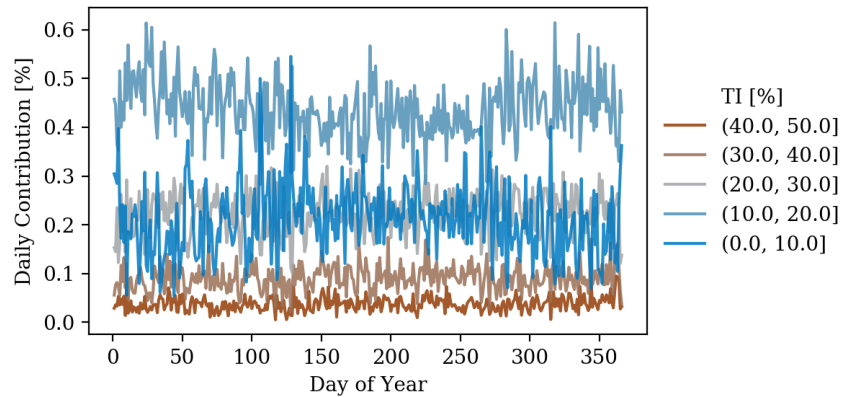
Figure 32. Relative frequency of observations at a given level of TI by day of year

The average-year time series in Figure 32 shows the relative frequency of observing the indicated ranges of TI. For each day, the sum of the contributions of each of the five turbulence classes represents 100% of the observations. The figure indicates that the five brackets of turbulence intensity remain roughly constant throughout the year, although they contribute different amounts to the total observations. Table 4 indicates the average contribution and standard deviation of each range of turbulence intensities shown in Figure 32. The figure indicates that turbulence in the range of $10\% < TI \leq 20\%$ is the most common bracket at the NWTC, accounting for an average 43.7% of the 10-min observations in a given day and as much as 60% of the conditions in days occurring in the winter months. More extreme turbulence is shown to be a consistent contributor to the overall site conditions, although they represent far less of the overall daily mix of turbulence: 9.1% for turbulence in the range of $30\% < TI \leq 40\%$ and 3.7% for turbulence in the range of $40\% < TI \leq 50\%$. Low-turbulence events, $TI \leq 10\%$, represent an average of 21.2% of the daily observations and are consistently observed throughout the year.

Table 4. Daily Average Contribution of Each Range of Turbulence Intensities

TI Range [%]	Average Daily Contribution [%]	Standard Deviation [%]
(0.0, 10.0]	21.2	7.19
(10.0, 20.0]	43.7	6.02
(20.0, 30.0]	22.3	4.14
(30.0, 40.0]	9.1	2.60
(40.0, 50.0]	3.7	1.48

Figure 33 reorganizes the daily representation of each range of TI into histograms. Each turbulence range is represented with the same coloring convention used (e.g., Figures 25 and 29) and is centered on the

average daily contribution indicated in Table 4. Figure 33 further confirms that, in general the NWTC exhibits moderately high turbulence intensities but that more extreme cases make a fairly small contribution to the overall conditions. The aggregation of periods of low-turbulence intensity (TI $\leq$ 10%) are shown in dark blue in the forefront of the figure and show a flatter distribution than the other TI brackets, with a standard deviation of 7.19%. Shown in Table 4, increasing the value of turbulence intensity corresponds with a decrease in standard deviation, indicating that the least turbulent events also make the most variable contribution to the daily site conditions.
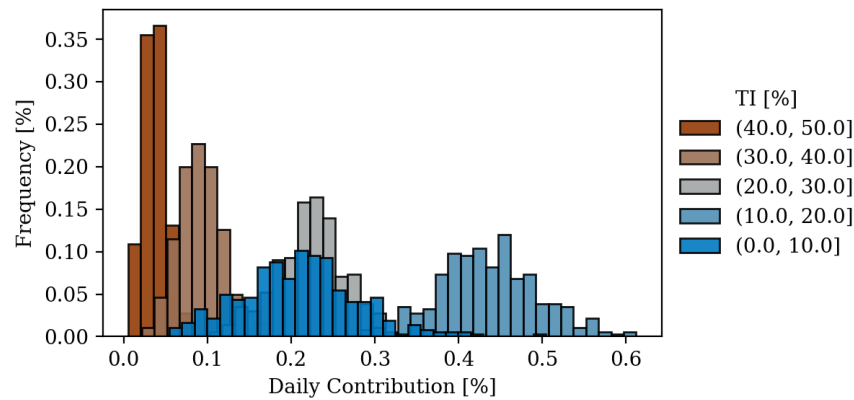
Figure 33. Histograms of daily representation of turbulence ranges

Figures 32 and 33 indicate that low-turbulence conditions are not isolated to any particular time of year. In order to determine what atmospheric conditions correlate to periods of low turbulence, the atmospheric properties corresponding to TI $\leq$ 10% are compared to the cumulative statistics in Figures 34 through 36. Figure 34 compares thermodynamic properties of the atmosphere from the full range of data to the low-turbulence conditions from the instrumentation closest to hub height of the GE wind turbine at the NWTC. The figure shows that the atmospheric properties do not vary significantly in overall character between cumulative and low-turbulence conditions. Filtering the observations to include only periods when TI $\leq$ 10% correlates with slightly increased air density and pressure (Figures 34a and 34b, respectively) and a slightly more evenly distributed histogram of air temperature (Figure 34c). The same characteristic bimodal distribution of air pressure is observed for low TI and the standard deviations of air density and temperature are slightly greater.

Comparison between the bulk flow conditions of wind speed and direction shown in Figure 35 make the low TI conditions more distinct from the overall conditions at the NWTC. The distribution of wind speed shown in Figure 35a indicates a higher overall wind speed than the cumulative data, as well as a sharper decrease toward both the high and low wind speed tails. The Weibull distribution shape parameter changes from 1.45 to 2.06 when considering only the periods of low turbulence.

The wind direction histograms compared in Figure 35b demonstrate the distinct differences in bulk flow parameters between the cumulative and low TI conditions. The overall site conditions feature prevailing winds from the west and, to a lesser degree, along the north-south axis throughout the year (refer to Figures 29 and 30). Considering only periods of TI $\leq$ 10% strongly emphasizes northerly and southerly winds. The histogram for low TI (red) in Figure 35b shows that the frequency of northerly winds is on the order of 10%, approximately twice that of northerly winds observed in a cumulative sense (blue). Similarly, the frequency of southerly winds increases from 3.5% to 6% when considering only low TI conditions. The cumulative site

conditions favor winds from the west representing approximately 7.5% of the total observations, although none of the 10° wind direction sectors distinguished by bins in the histogram contribute less than 1.8% to the total observations. The low TI histogram effectively shows zero observations of easterly winds and sharply attenuated westerly winds, approximately 2.8% down from 7.5%.

(a) Air density distribution

(b) Air pressure distribution

(c) Air temperature distribution
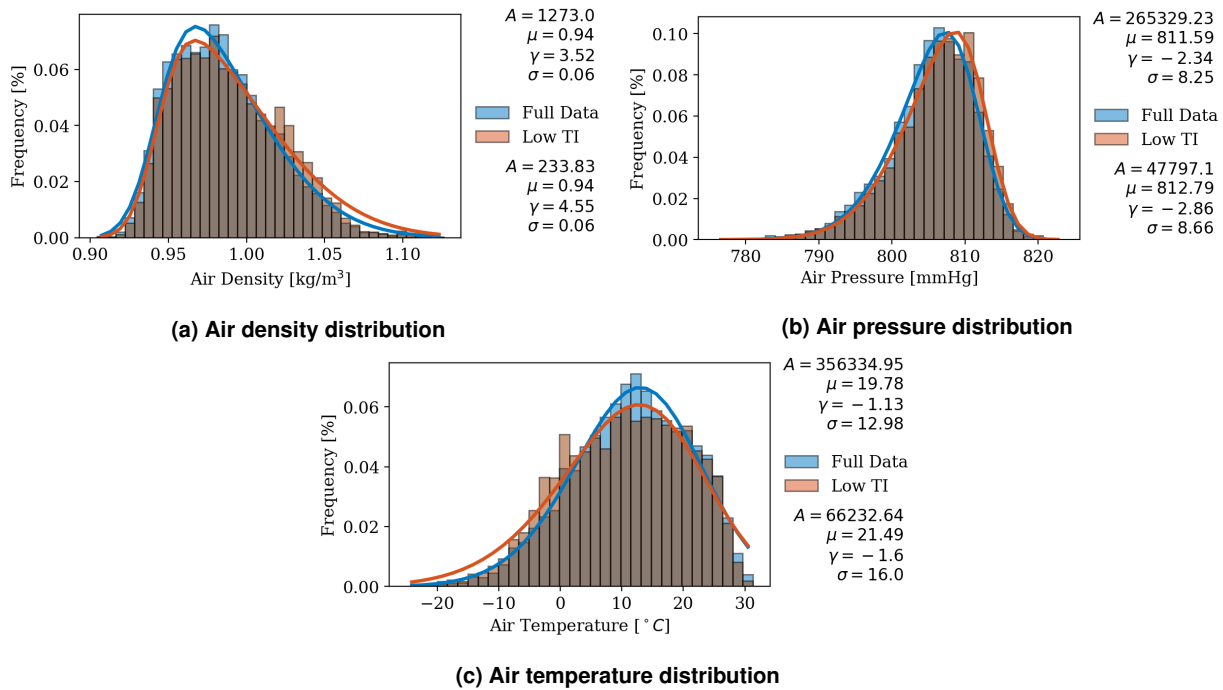
Figure 34. Bulk atmospheric conditions occurring when TI<10%

(a) Wind speed distribution

(b) Wind direction distribution
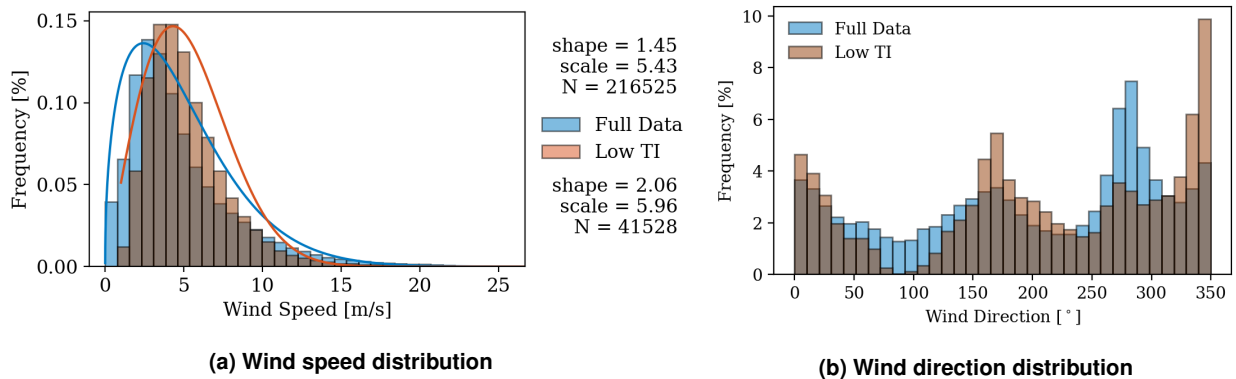
Figure 35. Wind speed and direction distributions of TI<10%

A more granular look at the low TI wind conditions is provided in the wind roses by month shown in Figure 37. Slicing the data by month further specifies the conditions in which periods of low TI are more commonly observed at the NWTC. Autumn and winter months (October–February) show relatively frequent observations of northerly and southerly winds, from sectors including $330° \leq WD \leq 360°$ and $150° \leq WD \leq 180°$, respectively. Each of these months also include a less frequent, but distinct, contribution of westerly winds in the range of 7–12 m/s. Springtime months (March–June) exhibit prevailing winds from the North

(a) Wind shear under low-turbulence conditions

(b) Wind veer under low-turbulence conditions
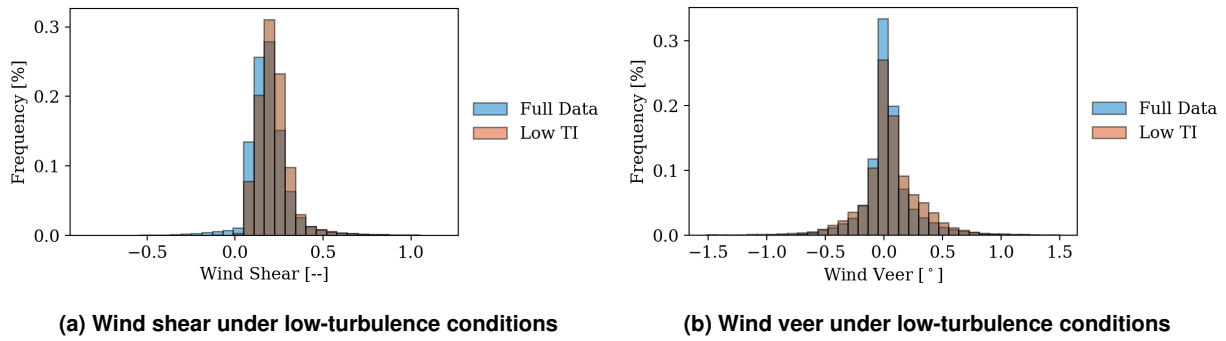
Figure 36. Wind shear and veer for TI<10%

under low TI conditions but do not demonstrate the same contribution of southerly winds. Winds during the summer months do not show the same distinct preference for prevailing wind direction, but the relative contribution of westerly winds is greater than those observed in the other seasons. Note that this figure is not a direct comparison to the monthly wind roses for the cumulative data in Figure 30. The radial axis denoting frequency of observations has the same limits in both figures, but the colors denoting brackets of wind speed have been modified for the low TI observations to better demonstrate the distribution of wind speeds.
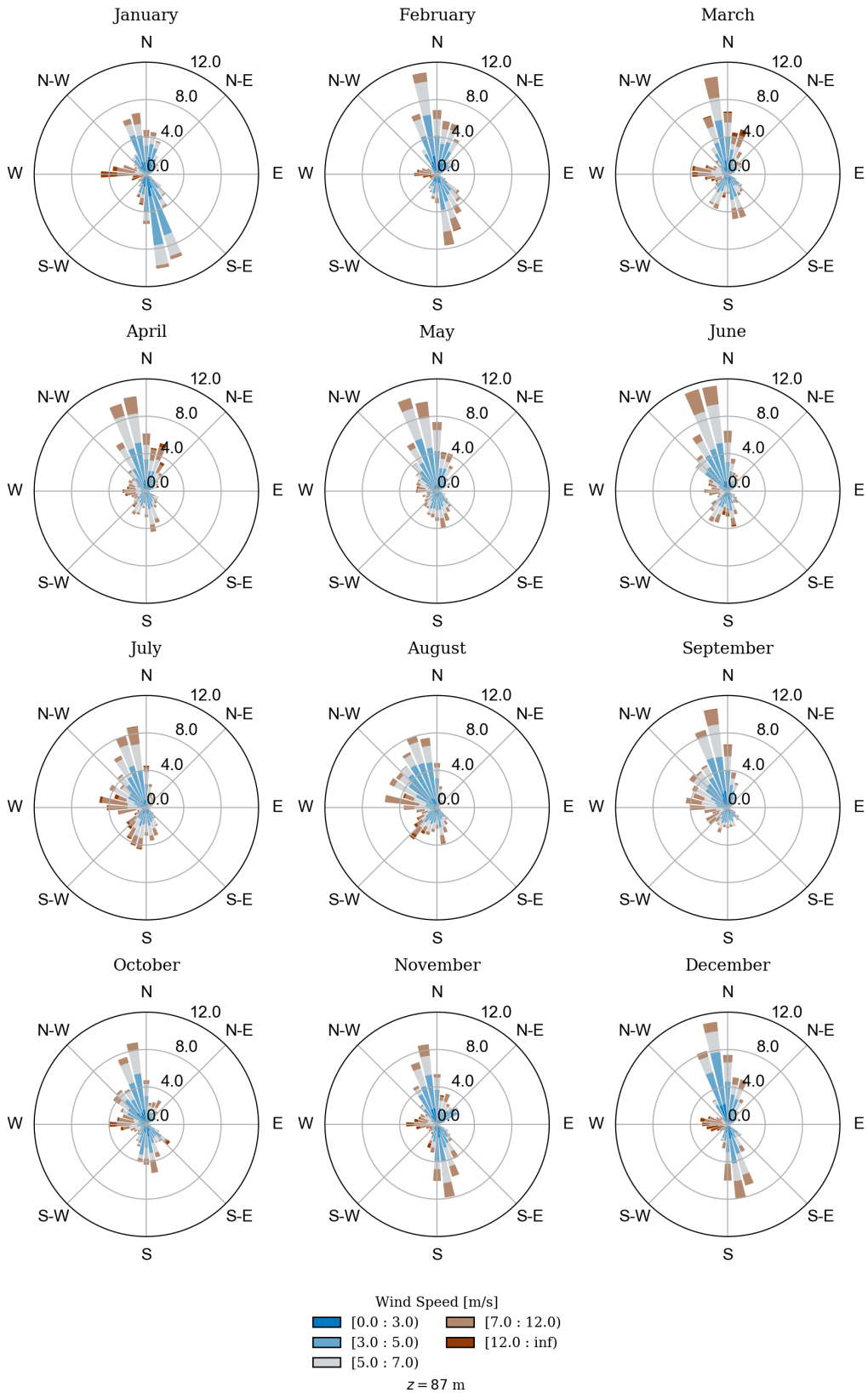
Figure 37. Wind roses by month for TI<10%

6.5 Wind Turbine Power Performance Testing

In terms of wind turbine validation and testing, wind speeds are evaluated for an entire generic power curve according to the IEC (2005) standards. The wind speed is normalized by a reference air density averaged over 10 min, ρ_{10min}. The 10-min average air density is calculated from 10-min average pressure and temperature data collected at 87 m, according to Eq. (6.3):

$$\rho_{10min} = \frac{P_{10min}}{R_o T_{10min}} \tag{6.3}$$

where T_{10min} is the measured absolute air temperature averaged over 10 min, V_{hub} is 10-min averaged hub height velocity, P_{10min} is the measured air pressure averaged over 10 min, and R_o is the gas constant of dry air. It should be noted that a portion of the pressure data of year 2015 contained a constant bias introduced by a questionable calibration of the instrumentation. Noted in Section 6.1, the pressure signal was corrected by adding an offset that corresponds to the difference between mean pressure during that period and the valid pressure signals from the respective part of the year (Figure 38). The derived 10-min average density is shown in Figure 38 along with the pressure and temperature. The 10-min average density, ρ_{10min}, exhibits peak values in January, whereas temperature, T_{10min}, in the same month is the lowest for any given year. The 10-min average density, ρ_{10min} is an average of 10% lower during the months of June and July.
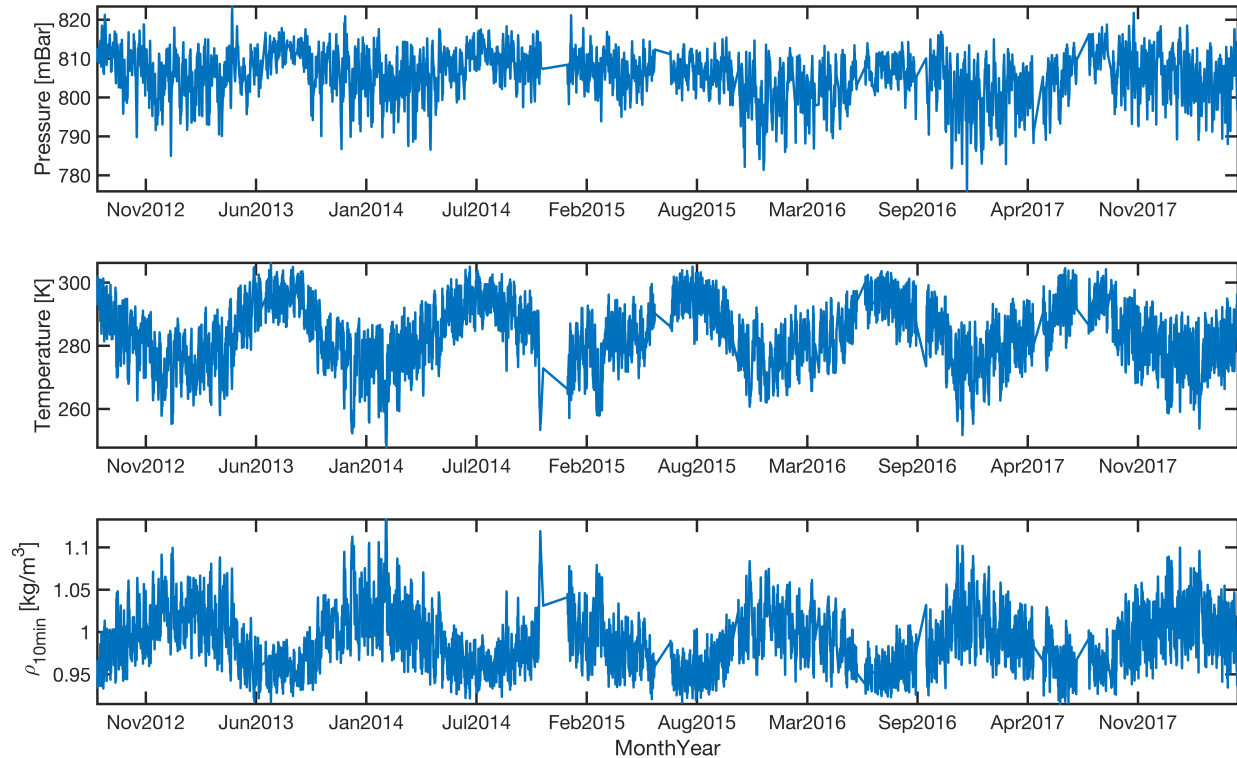
Figure 38. 10-min average density, ρ_{10min} (bottom), calculated from pressure (top) and temperature (center)

Normalization of the wind speed is accomplished following Eq. (6.4)

$$V_n = V_{hub}\left(\frac{\rho_{10min}}{\rho_o}\right)^{1/3} \tag{6.4}$$

46

where ρ_o is a reference density with a value of 1.225 kg/m^3. According to the IEC 61400-12-1 standard, wind speed is distributed according to the "method of bins." The wind speed range is divided into 0.5-m/s contiguous bins centered every 0.5 m/s. The IEC standard maintains a wind speed range extending from 1 m/s below the cut-in velocity of a given turbine to 1.5 times the nominal wind speed at 85% of the rated power of the wind turbine. For a given generic wind turbine that reaches rated power at 12.0 m/s, the highest bin for wind speed would be 16.0 m/s. These values also correspond exactly to those for the DOE-owned GE 1.5-MW turbine at the NWTC. For the presented power curve, wind speed bins range from 2.5 m/s to 16 m/s.

Power performance tests outlined by the IEC standard should be done with a "complete" database. A database may be considered complete if:

- Each bin includes a minimum of 30 min of sampled data.

- The full database includes a minimum of 180 hours of sampled data.

Following the convention of binning data in 10-min blocks, 30 min of data represent three samples of 10-min averaged data and 180 hours of sampled data represent 1,080 samples. Normalized wind data for each quarter are checked following the IEC requirements based on the number of 10-min average samples in each bin. Averaged quarterly data are shown in Figure 39 along with the total number of samples included in the quarter and the minimum number of samples included in a bin. The first quarter, Q_1, second quarter, Q_2, and fourth quarter, Q_4, each have 8,963; 6,800; and 7,311 samples, respectively, far greater than the required minimum of 1,080 samples. Additionally, each bin has more than three samples, meeting the second criterion in the IEC requirements. The third quarter, Q_3, has 6,831 total samples, but several bins have fewer than the three required samples. Suggested by the IEC standard, when a single bin has less than three samples, a simple linear interpolation over the incomplete bin is sufficient to complete the wind speed observations.

Given the data reported by M5 at the NWTC, it is recommended to start power performance testing in either Q_1, Q_2, or Q_4. In addition to the quarterly analysis, the time required to complete a power performance test starting at the beginning of each month of the year is reported in Figure 40b. The figure indicates the time that would be required to complete a power performance test starting in each month from 2012, during the years that data have been recorded with M5. Averaging the time requirements over the 6 years of data indicates that beginning a test on January 1 would require only 16 days, while starting on May 1 requires 144 days to meet the IEC requirements. Lower wind speeds in summer months do not contribute to the higher wind speed bins required for the tests, effectively extending the required testing time. Figure 40a shows the availability of 10-min samples for each month used in power performance testing.
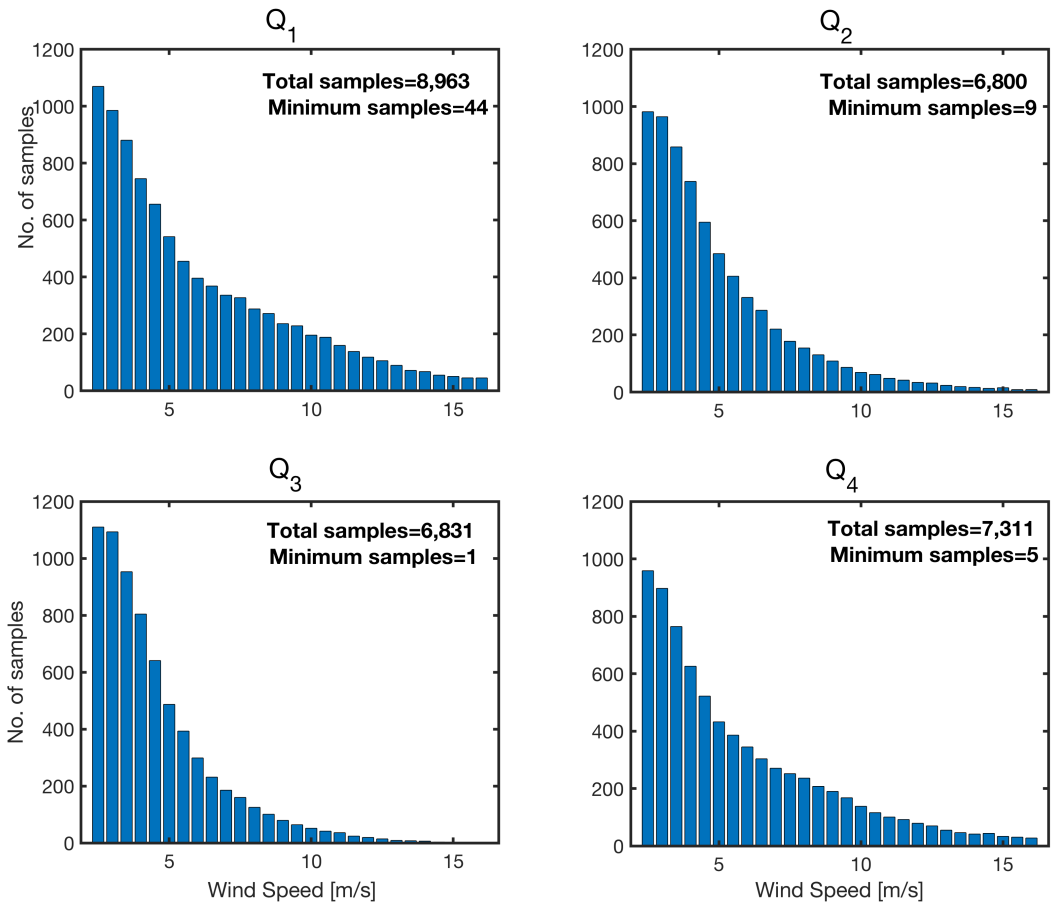
Figure 39. Normalized wind speed, V_n, shown with the total number of samples considered and minimum number of samples in the bins
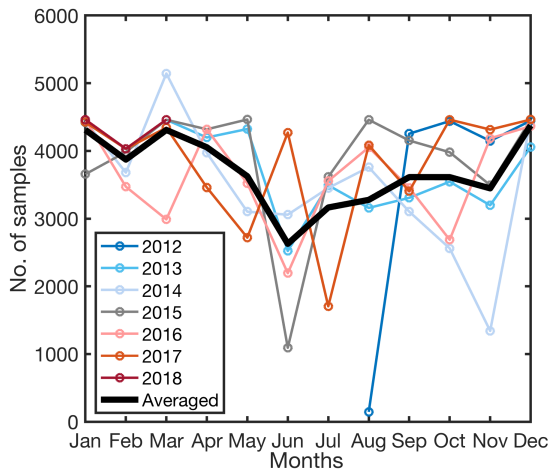
(a) Number of samples available per month for power performance test
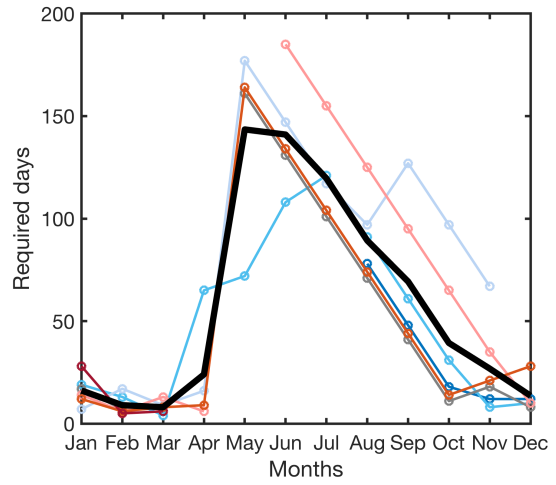
(b) Number of days required to meet the IEC requirements if experiment starts from the beginning of each month

Figure 40. Number of available samples per month for power performance test, and required days to meet the IEC requirements

49

7 Extreme Atmospheric Conditions

Wind turbine designs are often driven by extreme wind and atmospheric events anticipated and experienced over their design life cycles. These events can greatly impact reliability and costs of operational wind plants. Such extreme conditions are described by the IEC standards, designating several event types including peak extreme wind speed, change in wind direction, wind shear, and gusts, among others (IEC 2005). One of the main features of the NWTC is the relatively high frequency of extreme atmospheric events. Due to its placement, the NWTC is subject to strong seasonal wind patterns and weather events that arise at the interface of high-plains and mountainous regions. Additionally, Eldorado Canyon, an opening in the front range of the Rockies, sits to the WNW of the NWTC and acts to direct winter storms and Chinook winds across the site.

The IEC has designated atmospheric operating conditions for the design of particular wind turbine classes and has established metrics to identify and characterize extreme atmospheric events. According to the IEC standards, the NWTC is considered to be a viable site for testing Class I_A turbines, having a 50-year peak wind speed in excess of 50 m/s and turbulence intensity greater than 16% at an operating wind speed of 15 m/s. Results in the current section compare those assumptions to the available observations. The following development and notation is reproduced from the IEC (2005) guidelines for identifying extreme operating conditions. Throughout this chapter, V_{hub} is used to signify the 10-min average wind speed at 87m, the location of the cup anemometer closest to hub height of the DOE GE 1.5-MW turbine. Each type of extreme event relies on standard values determined by the site classification, including a reference velocity:

$$V_{ref} = 50 \ \ \text{m/s} \tag{7.1}$$

a reference turbulence intensity at 15 m/s:

$$I_{ref} = 0.16 \tag{7.2}$$

a longitudinal turbulence scale parameter:

$$\Lambda_1 = \begin{cases} 0.7z & z \le 60\text{m} \\ 42 & z > 60\text{m} \end{cases} \tag{7.3}$$

and a normal turbulence standard deviation:

$$\sigma_1 = I_{ref}(0.75V_{hub} + 5.6) \tag{7.4}$$

From these parameters, standardized "normal" operating conditions are derived. It should be noted that the normal operating conditions do not necessarily reflect the actual atmospheric resource at the NWTC but rather conform to the set of conventions used to assess the suitability of a given wind turbine for testing at a given location. With the IEC reference parameters defined above and the velocity, (V_{hub}), at a given hub height, (z_{hub}), the IEC standards estimate wind speeds can be represented by a Rayleigh probability distribution function (D_R) and cumulative distribution function (P_R) as:

$$\begin{aligned} D_R(V_{hub}) &= V_{hub}/(V_{ave}^2)\exp\left[-\pi V_{hub}^2/(2V_{ave})^2\right] \\ P_R(V_{hub}) &= 1 - \exp\left[-\pi(V_{hub}/2V_{ave})^2\right] \end{aligned} \tag{7.5}$$

where the average wind speed is assumed to be $V_{ave} = 0.2V_{ref}$. Figure 41a shows the Rayleigh probability and cumulative distribution functions defined in Eq. (7.6). For reference, Figure 41b shows a normal log-law wind profile for the reference velocity V_{hub} and a shear exponent of 0.2. Figure 41c shows the turbulence intensity expected for a given wind speed. As suggested by Eq. (7.4) and shown in Figure 41c with the black line, the IEC defines the the normal standard deviation of velocity to be a linear function of the average observed wind speed.

(a) Rayleigh probability and cumulative density functions

(b) Normal wind profile

(c) Turbulence standard deviation and TI
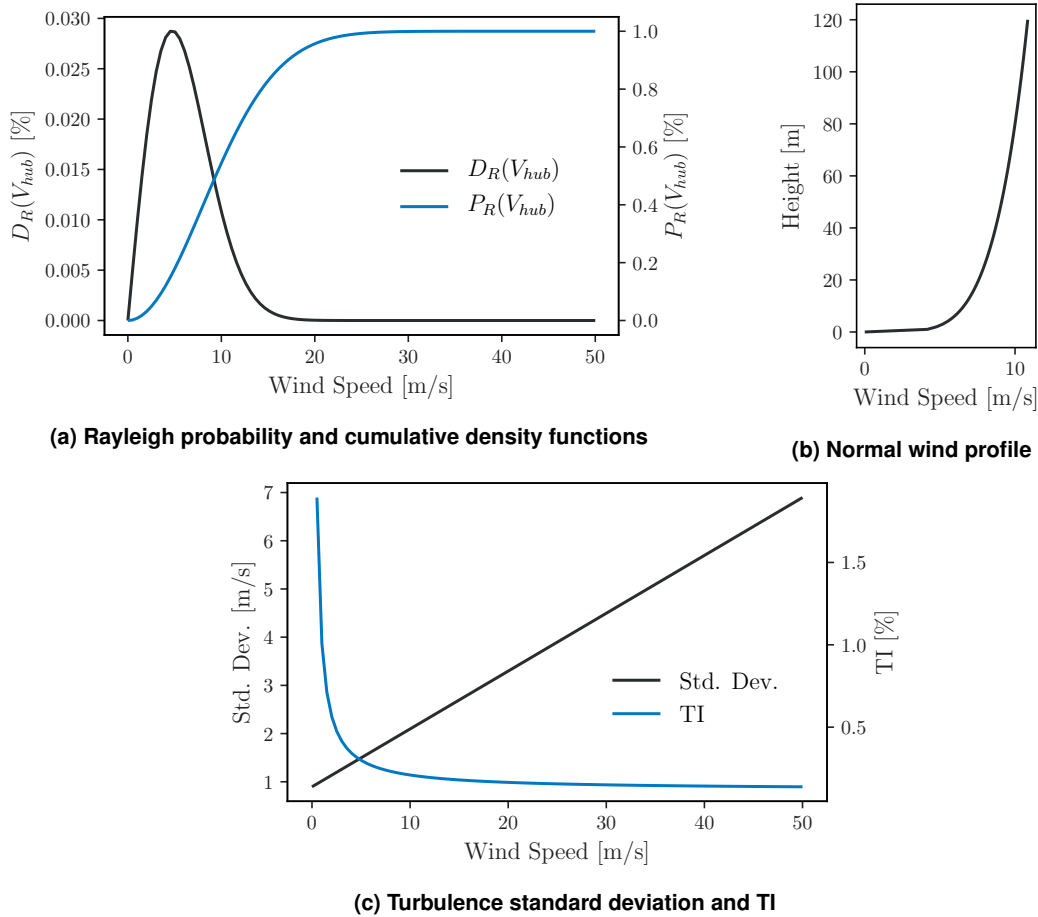
Figure 41. Profiles and distributions defined by IEC 61400-1 given the designation of Class I_A and setting $V_{hub} = V_{ave}$

Data recorded by the M5 tower from August 2012 to December 2018 are plotted to visualize the actual behavior of the fluctuating wind speed against the IEC requirements (Figure 42). Observations within 10-min time periods are averaged with a bin width of 1.0 m/s, showing comparatively lower turbulence intensity than suggested for an IEC class I_A site (Figure 42). However, variability of the wind speed fluctuations is relatively high, demonstrated by the spread of the blue points, and the broad spectrum of the wind speed characteristics should be taken into account while considering the identification of extreme events.

Frequency analysis performed on the observed wind speed data using 10-min averaged data from 2013, see Figure 43. The spectrum of 10-min averaged data shows higher energy spikes at low frequencies, corresponding to events occurring roughly every 30 days, 3 days, and 1 day, indicated by vertical lines in the figure. Low frequency events with higher energy confirm that the site is likely subject to mesoscale influences as well as strong diurnal variability.

(a) Standard deviation

(b) Turbulence intensity
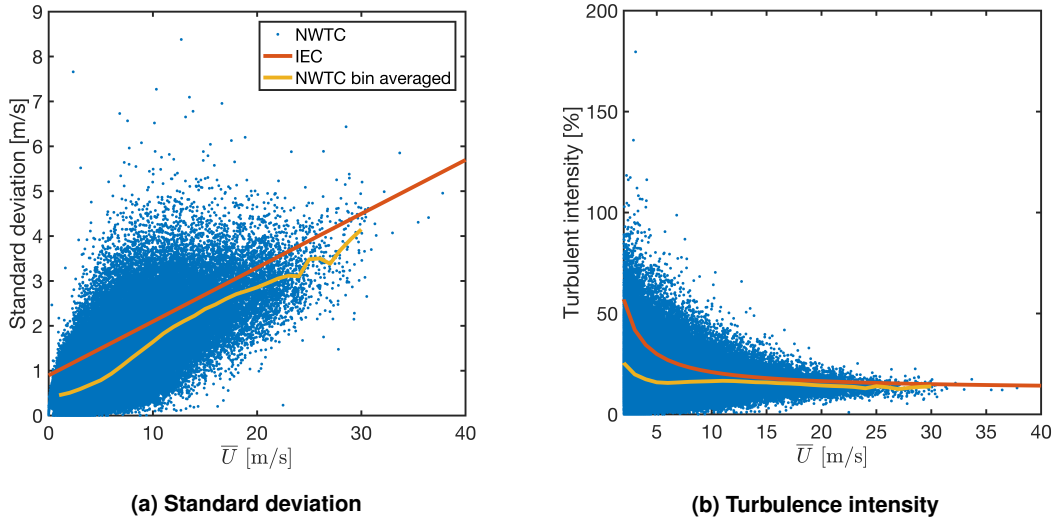
**Figure 42. 10-min averaged wind speed observations compared to
IEC definitions. Data were collected by the cup anemometer at 87m.**

Extreme events defined by the IEC Standard are separated into six types, each of which are associated with dynamic events that occur over relatively short time scales. Table 5 relates each of the event types to its expected time scale and the quantity or quantities of interest (QOI) in its definition. Extreme event type acronyms are defined in the table and reflect the definitions in the IEC standard. Each of the extreme event

Table 5. Extreme events from IEC 61400-1

Event Type	Acronym	Time Scale	QOI	Reference Value
Extreme Wind Speed Model	EWM	3 s/10 min	V_{hub}	$V_{e1}, V_{e50}, V_1, V_{50}$
Extreme Operating Gust	EOG	10.5 s	V_{hub}	V_{gust}
Extreme Turbulence Model	ETM	n/a	Std. Dev. of V_{hub}, σ	σ_1
Extreme Direction Change	EDC	6 s	Wind Direction $\Delta\theta$	$\Delta\theta_e$
Extreme Coherent Gust with Direction Change	ECD	10 s	$V_{\text{hub}}, \Delta\theta$	$V_{cg}, \Delta\theta_{cg}$
Extreme Wind Shear	EWS	12 s	α	α_+, α_-

types is detailed in the development below including the definition of limiting values or thresholds. Notation associated with QOIs and reference values are defined in Table 6 and defined to match the notation in the IEC standards as closely as possible.

Extreme events observed at the NWTC are more frequent during fall and winter months, as shown in Figure 44. The exception to this generalization is that EDC (extreme direction change) events occur much more consistently throughout the year, at a rate of approximately 262 events per month. Extreme wind speed model (EWM) events are not shown in the figure because the M5 data record lasts just over six years.

7.1   Extreme Wind Speed Model (EWM) Events
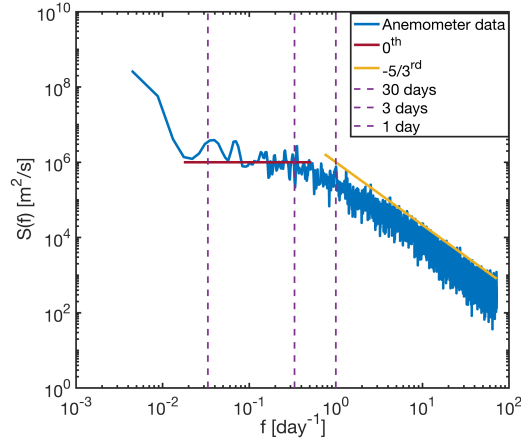
Figure 43. Spectrum of 10-min averaged data of a year

Table 6. Nomenclature and unit associated with quantities of interest and reference values used in the detection of extreme events.

QOI or reference value	Event Type	Description	Units
V_{hub}	All event types	Hub-height velocity	m/s
V_{e1}	EWM	Steady extreme wind speed with a recurrence period of 1 year	m/s
V_{e50}	EWM	Steady extreme wind speed with a recurrence period of 50 years	m/s
V_1	EWM	Turbulent extreme wind speed model with a recurrence period of 1 year	m/s
V_{50}	EWM	Turbulent extreme wind speed model with a recurrence period of 50 years	m/s
V_{gust}	EOG	Hub-height gust velocity magnitude	m/s
σ	ETM	Measured standard deviation of longitudinal velocity component	m/s
σ_1	ETM	Representative value of the turbulence standard deviation (Eq. (7.4))	m/s
$\Delta\theta$	EDC	Measured wind direction change	degrees ($^\circ$)
$\Delta\theta_e$	EDC	Wind direction change threshold	degrees ($^\circ$)
V_{cg}	ECD	Extreme coherent gust velocity magnitude	m/s
$\Delta\theta_{cg}$	ECD	Extreme coherent gust wind direction change	degrees ($^\circ$)
α	EWS	Measured shear exponent	(unitless)
α_+	EWS	Positive shear exponent threshold	(unitless)
α_-	EWS		
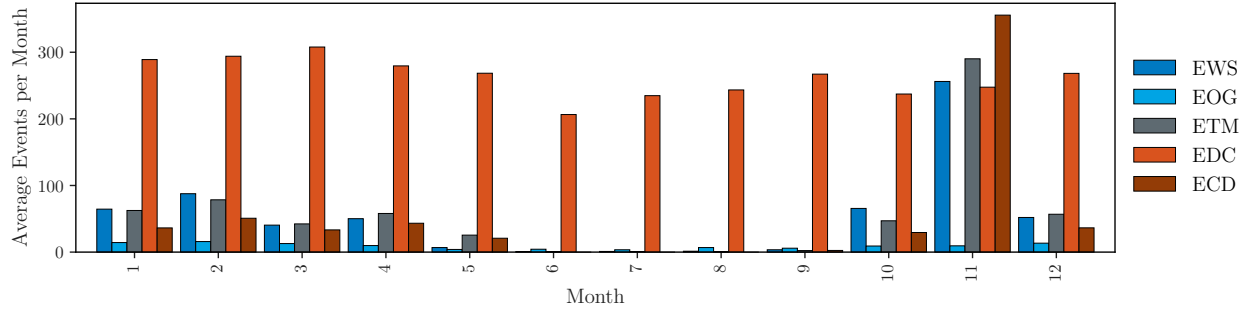
Figure 44. Average monthly occurrence of IEC events observed at the NWTC

ularly true for the 50-year extreme. Noted in the previous section, the IEC guidelines distinguish between EWM events, calculated from high-frequency data averaged in 3-s intervals, and *turbulent* EWM events, which are detected in 10-min averaged data and are considered to account for turbulent variations within a 10-min interval. Each type of EWM event has a distinct set of thresholds for detection in addition to a distinct pre-treatment of the raw wind speed data. Averaging of the data amounts to low-pass filtering, which reduces the effects of instrument noise and spurious spikes from the raw data and provides a cleaner estimate of wind speed while retaining the dynamic quality of the signal. The velocity thresholds corresponding to EWM events with a recurrence period of one year or 50 years are respectively defined as,

$$
\begin{aligned}
V_{e50}(z) &= 1.4 V_{\text{ref}} \left(z/z_{\text{hub}} \right)^{0.11} \\
V_{e1}(z) &= 0.8 V_{e50}(z)
\end{aligned}
\tag{7.6}
$$

where $V_{\text{ref}} = 50$ m/s is the reference wind speed for a Class I$_{\text{A}}$ site.

Turbulent EWM events are distinguished from standard events with a different threshold and are sought in 10-min average velocity data. A longer averaging period includes a greater span of observed instantaneous wind speeds and is assumed to include normal turbulent variation in the velocity signal. Accordingly, the thresholds for detection of turbulent EWM events are lower than those for the standard EWM events,

$$
\begin{aligned}
V_{50}(z) &= V_{\text{ref}} \left(z/z_{\text{hub}} \right)^{0.11} \\
V_1(z) &= 0.8 V_{50}(z)
\end{aligned}
\tag{7.7}
$$

Notation for EWM and turbulent EWM thresholds are distinguished by the use or absence of an *e* in the subscript, respectively. The recurrence periods of one or 50 years related to each threshold correspond to the frequency of observation of a given wind speed in the two-parameter Weibull distribution defined in Eq. (7.8). Direct observation of wind speeds above the EWM velocity thresholds is not common given that extreme wind speeds occur only rarely and because the sensors shut down for safety under certain conditions. Sonic anemometers on M5 shut down when wind speeds are above 30 m/s; cup anemometers (used in the following analysis) have a larger operating range up to 90 m/s but shut down or produce unreliable wind speed estimates under icy conditions.

Distributions of the observed wind speed with the 3-s average filter are shown in Figure 45 for each year in the data record. Data used for EWM event detection are from the cup anemometer located at 87m on M5. Shape and scale parameters are derived for the wind speed distribution of each year between 2012 and 2018. Distribution parameters are derived by least-squares fit to a two-parameter Weibull distribution,

$$
F(V) = 1 - \exp\left[-(V/A_0)^k \right]
\tag{7.8}
$$

where A_0 is the Weibull scale parameter and k is the Weibull shape parameter. Weibull distribution parameters are summarized in Table 7. The scale and shape parameters calculated for each yearly distribution of 3-s mean wind speed do not vary substantially over the data record, indicating that there is little year-to-year variability of the 3-s mean wind speed distribution within the M5 data record.
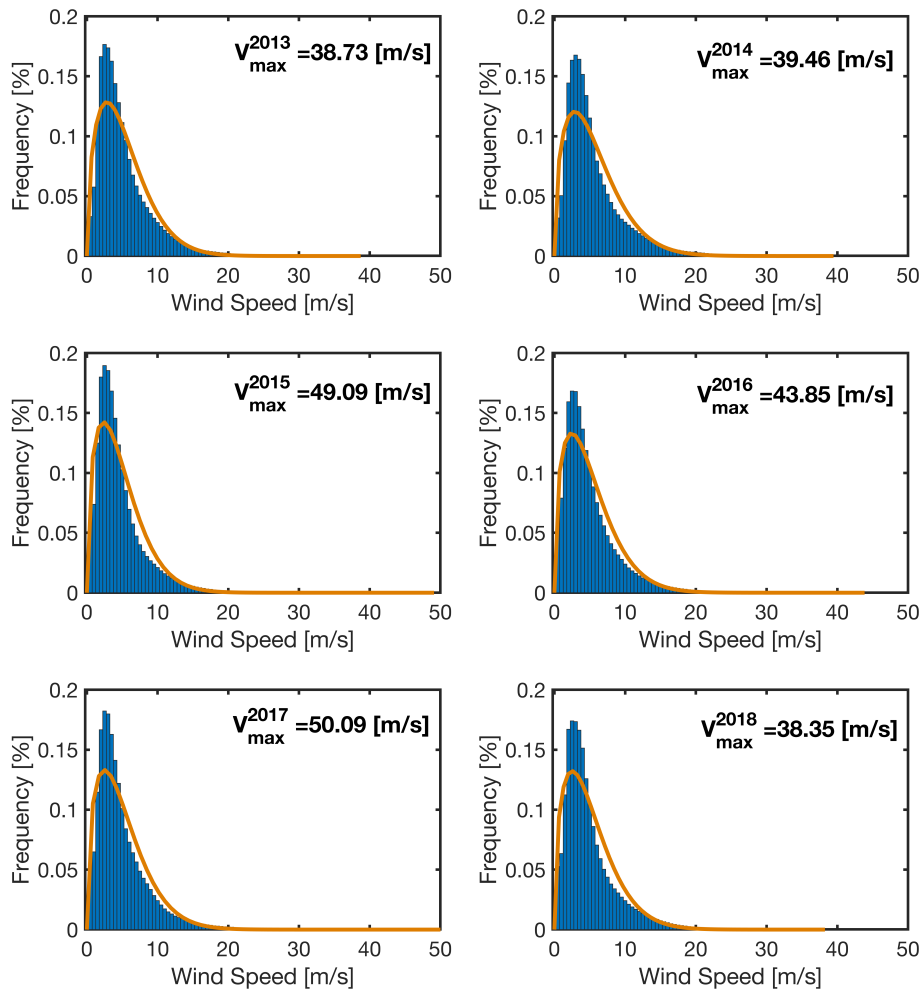
Figure 45. 3-s mean wind speed distribution per year. Left column is years 2013, 2015, and 2017 and right column is years 2014, 2016, and 2018

Due to limited direct observation of EWM events, the occurrence rate of high wind speeds must be estimated. Several methods of direct estimation are compared to extrapolation of Weibull and Gumbel distributions fit to data above a given threshold. Direct estimation methods are based on the annual maximum wind speeds observed by the cup anemometer at 87m on M5, whereas extrapolations with statistical distributions are based on daily maximum wind speeds. In either case, the wind speeds used to estimate the recurrence rates of EWM events rely on the averaging conventions outlined above. Estimated recurrence rates are summarized in Table 9 and compared to IEC recommendations below.

Table 7. Weibull distribution parameters of 3-s mean wind speed

Year	Scale (A) [m/s]	Shape (k)
2013	5.81	1.51
2014	6.16	1.48
2015	5.20	1.46
2016	5.55	1.44
2017	5.55	1.45
2018	5.60	1.45
Average	5.66	1.465

The two direct methods of estimating the recurrence rate of EWM events use a subset of observations from M5 and formulations found in the literature to arrive at estimates of the wind speeds that occur at an exceedance rate of 50 years. Although both the "peak-over-threshold" and "annual-maxima" methods must extrapolate to the 50-year recurrence rate, they are distinguished from statistical extrapolation methods used below which fit common statistical distributions to observational data and extend those distributions to the desired rates of recurrence. Because the historical record of data from M5 extends only as far back as 2012, estimates of the true EWM occurrence rates remain highly uncertain.

7.1.1 Direct Estimation

The accumulated probability of extreme wind speeds is well-described by a double-exponential Gumbel distribution formulation,

$$F(V_{\max}) = \exp\left(-\exp\left[\frac{V_{\max} - C_\beta}{C_\alpha}\right]\right) \tag{7.9}$$

where $V_{\max}$ is the maximum wind speed calculated per annual cycle. The constants, C_α and C_β, describe the distribution of the data (Mann, Kristensen, and Jensen 1998; Pryor, Barthelmie, Clausen, Drews, MacKellar, and Kjellström 2012), which are themselves estimated with the probability-weighted moment method (Hosking, Wallis, and Wood 1985):

$$C_\alpha = \frac{2b_1 - \overline{V}_{\max}}{\ln 2}; \quad C_\beta = \overline{V}_{\max} - C_\alpha \gamma_E; \quad \gamma_E \approx 0.578 \tag{7.10}$$

where, γ_E is Euler's constant and $\overline{V}_{\max}$ is the mean of the maximum annual wind speeds during the considered record. In the current case, the data record spans six years, and $\overline{V}_{\max}$ is the maximum realization of the set of six annual-maximum velocities.

The "annual-maxima" method, estimates the T-year extreme wind speed from the Gumbel distribution as:

$$V_T = C_\alpha ln(T/T_p) + \beta \tag{7.11}$$

where T_p is the base period (one year) used to estimate the maximum wind speed. With the annual-maxima method, estimates of the 50-year extreme wind speed are reached with a generalized extreme value distribution.

The "peak-over-threshold" method is used to estimate the recurrence rate of extreme wind speeds based on a generalized Pareto distribution (Gusclla 1991; Cook 1982). In the peak-over-threshold method, the extreme wind speed is estimated from the *smallest* observed value of the annual-maximum velocities (Hansen,

Larsén, Kelly, Rathmann, Berg, Bechmann, Sempreviva, and Jørgensen 2016; Larsén, Mann, Rathmann, and Jørgensen 2013). For M5, the smallest annual-maximum value of 10-min averaged wind speed in the data record is 23.9 m/s. This value is considerably lower than the EWM thresholds established by the IEC standards, but is used as a reference to estimate the relative frequency of extreme events.

According to Larsén, Mann, Rathmann, and Jørgensen (2013), the extreme wind after T years found with the peak-over-threshold method is,

$$V_T = V_{thresh} + A_o ln(\lambda_o T) \tag{7.12}$$

where λ_o is the observed exceedance rate over a given wind speed threshold, V_{thresh}. A_o is the average rate of exceedance over the threshold, $A_o = \langle V_i - V_{thresh} \rangle$, and angle brackets indicate an average in time. The threshold velocity used in the peak-over-threshold estimation can be any of the four EWM threshold velocities, V_{e1}, V_{e50}, V_1, or V_{50} The main benefit of the peak-over-threshold method is the consideration of the exceedance rate, which is not provided by the annual-maxima method above.

Based on the annual maxima method, V_{50} and V_{e50} (filtered by a window of 10 min or 3 s) are estimated to be 34.3 m/s and 57.3 m/s, respectively (the 10 min V_{50} is shown in Figure 46). The peak-over-threshold method estimates the 50-year steady and turbulent extreme wind speeds to be 37.5 m/s and 58.8 m/s, respectively. Differences between the two estimation methods depend on the threshold of the wind speed, data filtering and pretreatment, and distribution parameters. More detail about the sensitivity of these analyses can be found in Larsén, Mann, Rathmann, and Jørgensen (2013).
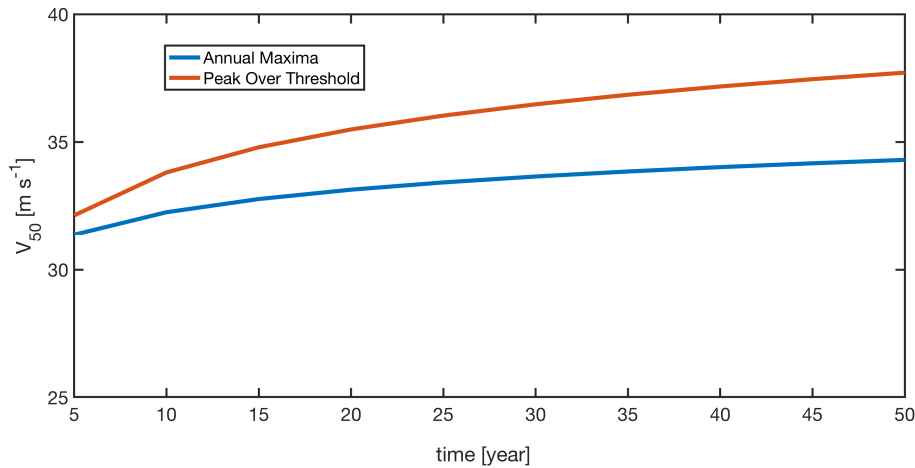
**Figure 46. 50-year wind prediction with annual maxima method
and peak-over-threshold method with 10-min averaged data**

7.1.2 Statistical Distributions

Statistical extrapolation methods rely on fitting either a two-parameter Weibull or a Gumbel distribution (Eqs. (7.8) or (7.9), respectively) to the wind speed observation data, and extending the fitted distribution to the recurrence rates or velocity thresholds of interest. The probability distributions resulting from least-squares fitting do exhibit some sensitivity to the particular data considered. Because the distributions are being used to estimate the recurrence of extreme events, the data that provides the most value for fitting come from the tail of the distribution corresponding to higher wind speeds.

Least-squares fitting and extrapolation using either distribution relies on daily maximum values of wind speed, subjected to averaging windows of either 3-s or 10-min for standard and turbulent EWM events, respectively. The tail of the distribution corresponding to higher wind speeds is emphasized in the fitted distributions by considering only data above selected wind speed thresholds. Thresholds are chosen as portions of the standard deviation (σ) above the mean (μ) wind speed from each distribution. Fitted distributions provide estimates of either V_{e50} or V_{50} (using 3-s or 10-min averaged wind speeds, respectively) from observations 0, 0.7, 1.4, 2.0, or 2.5 σ above μ. Establishing thresholds for data to consider emphasizes physics underlying elevated wind speeds. Given the strong seasonality to the wind resource at the NWTC, thresholding the data has a similar effect as considering only data from the winter months, when winds are generally higher.

Figures 47 and 48 show the wind speed extrapolation methods using Weibull and Gumbel distributions. The top subplot in each figure compares distributions fitted to data over the thresholds described in the paragraph above. In each figure, the colored lines denote the various velocity thresholds used in the least squares fits

Table 8. Threshold values used to fit Weibull and Gumbel distributions

Color		Threshold	
		3-s Data [m/s]	10-min Data [m/s]
purple	μ	15.93	11.19
yellow	$\mu + 0.7\sigma$	21.20	14.83
gray	$\mu + 1.4\sigma$	26.47	18.50
blue	$\mu + 2.0\sigma$	30.98	21.59
black	$\mu + 2.5\sigma$	36.75	24.19

Vertical dashed lines indicate the threshold values reported in Table 8. Solid and dashed curves indicate the Gumbel and Weibull distributions that arise from the corresponding thresholds. The round and diamond markers indicate estimated values of velocity with a probability of exceedance of 50 years using the specified thresholds. Estimated velocities with a 50-year recurrence rate show some sensitivity based on the data threshold, especially when using a Weibull distribution. A Gumbel distribution is by nature an extreme value distribution, which is based on generalized extreme value (GEV) distribution, and leads to reduced variability in the estimates of extreme wind speeds across all thresholds.

The lower subfigures (Figure 47b and Figure 48b) show fitted distributions with the threshold $\mu + 1.4\sigma$. This is the threshold for which the estimates provided by the Weibull and Gumbel distributions are in the greatest agreement and is recommended by Moriarty, Holley, and Butterfield 2004. Fitted statistical distributions can be used two ways: they can provide estimates of wind speeds with a given probability of exceedance (black dashed lines) or they can provide estimates of the recurrence rate of the velocity thresholds recommended by the IEC standards for a Class I_A site (blue dashed lines). Using either the 3-s averaged data to estimate V_{e1} and V_{e50} or using 10-min averaged data to estimate V_1 and V_{50} result in wind speeds that are far below the IEC standard values.

The two direct estimation methods described in Section 7.1.1 and the extrapolation methods used in Section 7.1.2 arrive at different estimates of the wind speed corresponding to a recurrence rate of 50 years. Resulting '50-year velocities' are summarized in Table 9, including comparison to the IEC standard values and the time window used for averaging velocity signals for each value. Results provided by all methods lean toward lower wind speeds than the recommendations listed in the IEC standards, regardless of data pretreatment or

Figure 47. Extrapolated wind speed distributions using 10-min averaged data. a) 50-year wind speed prediction based on the observations with different thresholds; b) IEC specified and estimated wind speeds (V_1 and V_{50}) and their respective rates of recurrence

statistical distribution. Estimated values of wind speeds with the recommended recurrence rates consistently fall 20-25% below the IEC recommendations, arising in part from the sensitivity and uncertainty associated with the estimation methods used here. Noted previously, wind turbine design parameters provided by the IEC standards, including EWM event thresholds, are guidelines that were generalized from a set of observations in northern Europe and are not expected to reflect the exact conditions at the NWTC. Additional information regarding the distribution of extrapolated estimates of EWM recurrence rates can be found in Appendix B.

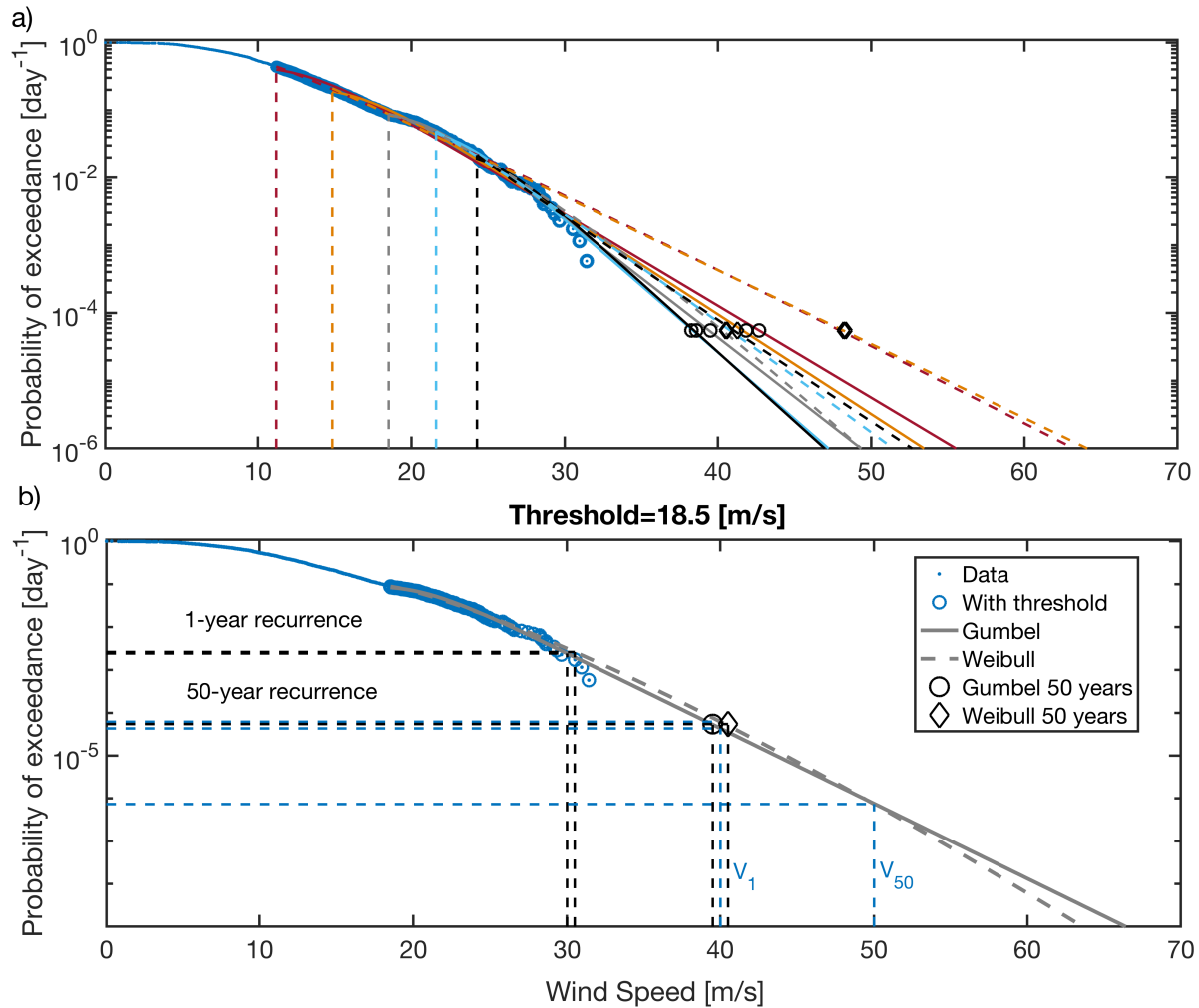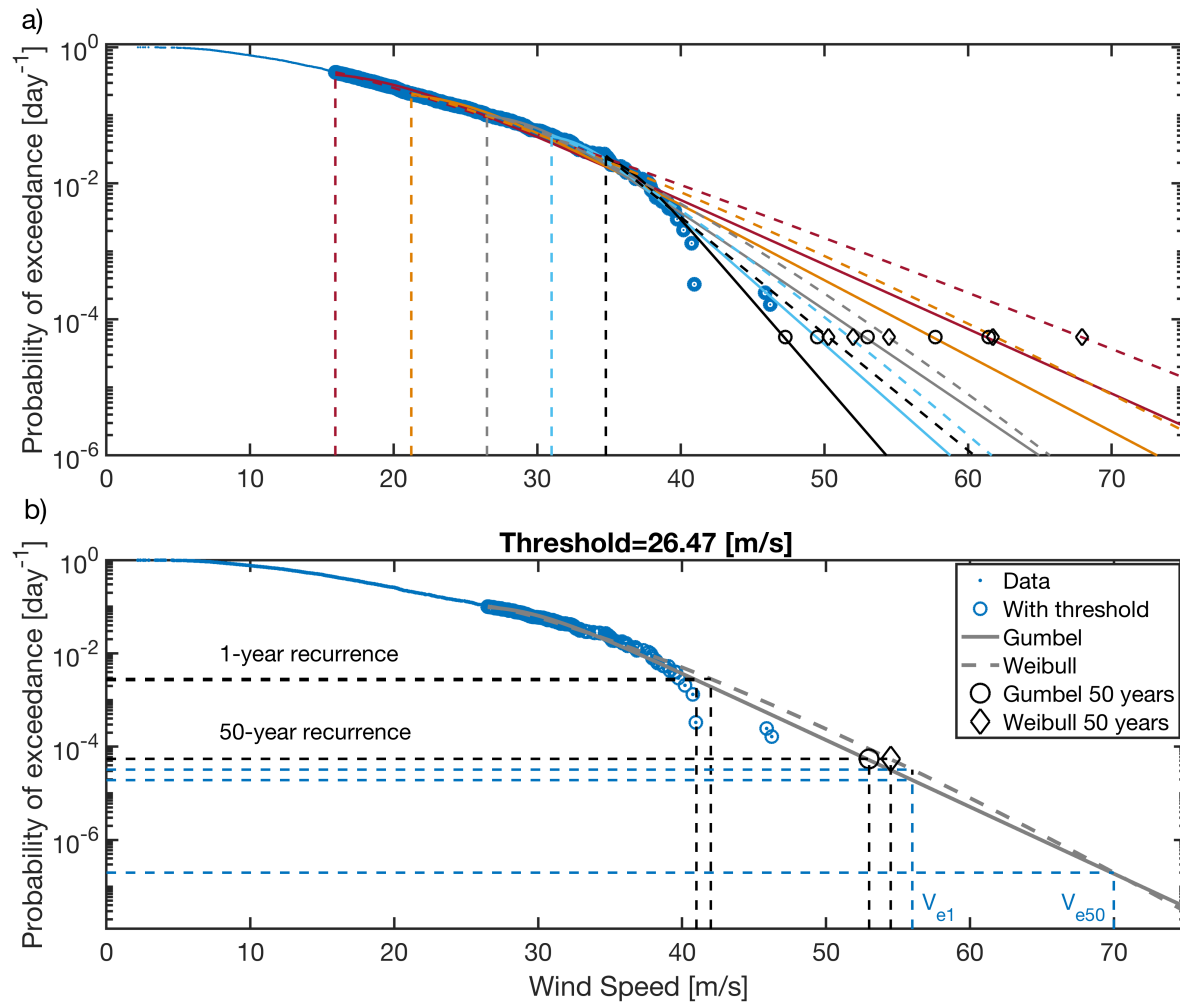**Figure 48. Extrapolated wind speed distributions using 3-s averaged data. a) 50-year wind speed prediction based on the observations with different thresholds; b) recommended and estimated wind speeds (V_{e1} and V_{e50}) and their respective rates of recurrence**

Table 9. Estimation of wind speeds with a 50-Year recurrence rate from M5 data based on annual maxima or daily maxima

7.2 Extreme Operating Gust (EOG) Events

The extreme operating gust can be a wind turbine design driver and often turbine controllers are tuned to accommodate them at specific sites. In a general sense, wind gusts are defined by a peak of wind speed over the mean or background wind speed that persists for only a short duration. Characterizing wind gusts at the NWTC, as with all of the IEC extreme events, requires several levels of quality control and filtering for the raw 20 Hz data. After filtering the wind speed data for lost signals and near zero wind speeds, a Hampel filter (Pearson, Neuvo, Astola, and Gabbouj 2016) with a 1-min window and filter width of 5 standard deviations from the median wind speed is used to remove outliers from the 20 Hz signal. This filtering step removes noise from the raw data, and ensures that gusts are not falsely identified and reported. After this procedure, 10 min averages are calculated and retained only if 80% of the 20 Hz data within the 10 min is valid. This quality control process is independent of the one described in Section 4.2 that was used to assess the quality of the 10-min binned data, and is used only for the high-frequency data used in quantifying extreme events.

The time period over which a gust is calculated has a significant influence on the observed value. For example, a storm may have wind speeds higher than the value of V_{gust} from Eq. (7.13), but generally storm events persist longer than what is typically associated with a gust. As noted in Table 5, the time scale for identifying EOG events is $T = 10.5$ s. Events that persist for a longer time are difficult to classify as gusts, and are more readily associated with weather fronts or meso-scale meteorological events. Therefore, for the classification of extreme operating gust events, selection is done based on the IEC-61400-1 (Section 6.3.2.2) recommendations. Taking the IEC reference case, the velocity amplitude used in the identification of a gust, V_{gust}, is defined as:

$$V_{\text{gust}} = \min\left[1.35\,(V_{e1} - V_{\text{hub}}); \quad 3.3\left(\frac{\sigma_1}{1+0.1(D/\Lambda_1)}\right)\right]$$

(7.13)

where, V_{hub} is the 10-min average wind speed at hub height and V_{e1} is estimated extreme wind speed for a single year. The normal turbulence standard deviation, σ_1, is defined in Eq. (7.4). The gust magnitude, V_{gust}, defines the threshold of velocity magnitude used to identify extreme operating gusts according to Eq. (7.14), which scales with the mean 10-min wind speed V_{hub}.

Finally, the reference dynamic wind gust event is:

$$V(t) = V_{\text{ave}} - 0.37V_{\text{gust}}\sin(3\pi t/T)\,(1 - \cos(2\pi t/T))$$

(7.14)

The characteristic EOG event defined in Eq. (7.14) is shown in Figure 49
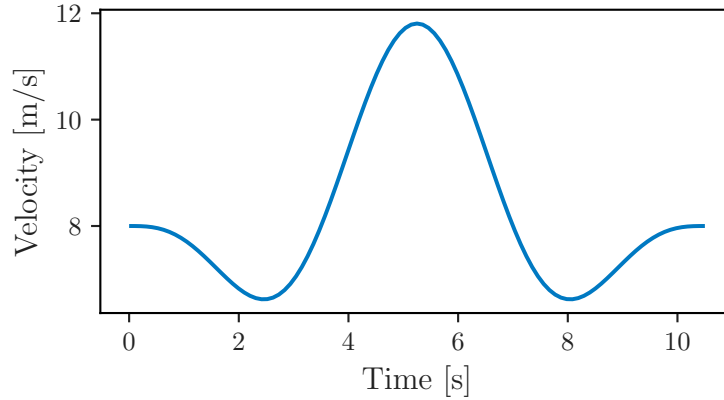
Figure 49. Characteristic EOG event with $V_{\text{hub}} = 8$ m/s
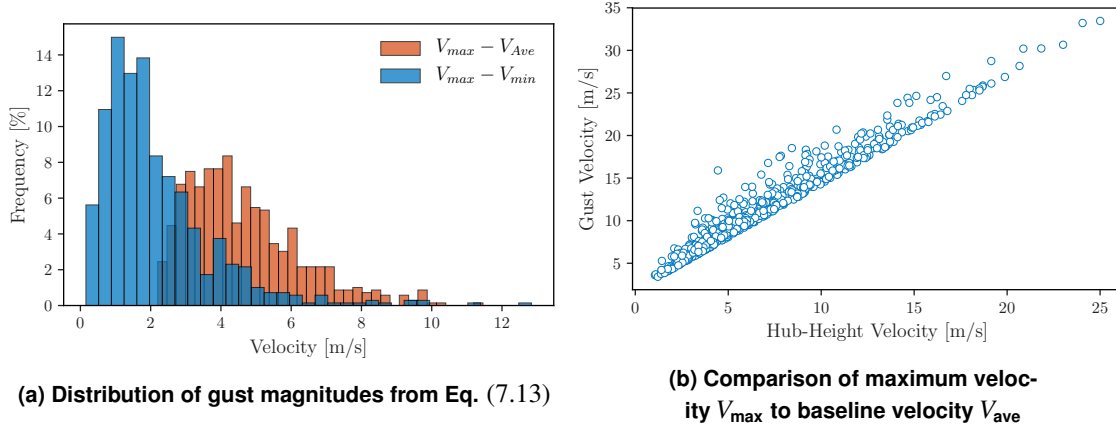
(a) Distribution of gust magnitudes from Eq. (7.13)

(b) Comparison of maximum velocity V_{max} to baseline velocity V_{ave}

Figure 50. EOG events recorded by M5

The NWTC experiences approximately 110 EOG events per year on average, largely associated with bulk wind flows from the prevailing wind direction of WNW (Figure 51). It should be noted that the IEC definition of EOG events considers the deviation of the 3-s peak velocity above the 10-min baseline average velocity. If one considers the deviation of peak velocities from the average within the dynamic event itself ($T = 10.5$ s), many more gust events may be identified. In that case, the gust of maximum intensity was observed to begin from a base velocity of 12.0 m/s and reached a peak velocity of 47.9 m/s.

7.3 Extreme Turbulence Model (ETM) Events

The extreme turbulence model event defined by the IEC is simply any observation in which the turbulence standard deviation defined in Eq. (7.4) exceeds a threshold defined as,

$$\sigma_1 = c \, I_{\text{ref}} \left(0.072 \left(\frac{V_{\text{ave}}}{c} + 3 \right) \left(\frac{V_{\text{hub}}}{c} - 4 \right) + 10 \right) \tag{7.15}$$

where $c = 2$ m/s. ETM events occur 430 times a year on average; most ETM events (about 300) are observed in the month of November, and they are rarely in the summer months between May and September.

Figure 51. EOG event rose showing prevailing wind direction and V_{max} from Figure 50

Figure 52 shows the distribution of ETM events by the direction of the prevailing wind during observation, against the background wind speed, and terms of the strength of each event. The distribution of ETM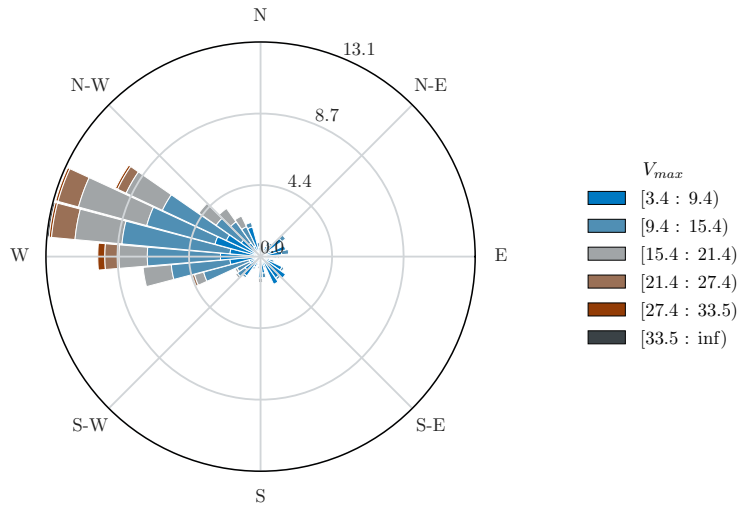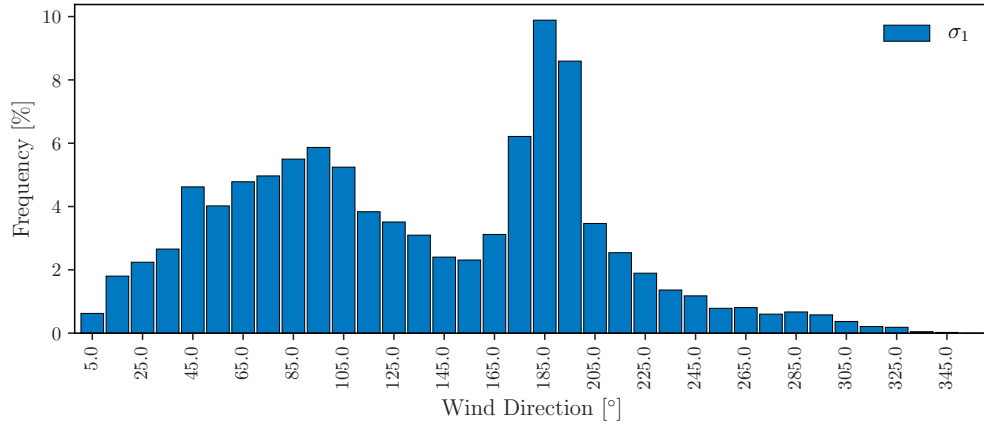 events against wind direction (Figure 52a) shows that ETM events are largely associated with wind from the south and, to a lesser degree, from the east.

When considering ETM events it is important to recall that the 'normal standard deviation' (Figure 52b) of wind speeds is not a direct statistical calculation, but rather is derived from the empirical relationship in Eq. (7.4). Turbulence intensity is another common quantification of the importance of the variability in wind signals, and is discussed at length in Section 6.4. The histogram in Figure 52c indicates that ETM events are largely associated with a standard deviation of velocity $\sigma_1 = 8 \pm 3$ m/s. ETM events with $\sigma_1 > 13$ m/s represent less than 1% of observations.

7.4   Extreme Direction Change (EDC) Events

An extreme direction change event is defined by the IEC standards as a sudden shift in the bulk flow direction beyond a threshold value that depends on the mean wind speed at hub height. The time span for a dynamic extreme direction change event to occur is only $T = 6$ s (as opposed to the $T = 10.5$ s window employed for extreme operating gusts). Instantaneous wind direction is calculated from high-frequency (20 Hz) data subjected to a 3-s moving-average low-pass filter. Low-pass filtering of the velocity signals helps to remove outliers from high-frequency data. Wind direction changes, $\Delta\theta$ are calculated over each 6-s interval. Within each 10-min record of atmospheric data, only the maximum value of $\Delta\theta$ is retained in the following results. Thus, a 10-min record provides a single value $\Delta\theta$ to be considered.

The maximum of the wind direction change within any given 10-min period $\Delta\theta$ is plotted against the average hub-height velocity at the time of observation in Figure 53a

(a) ETM events by average wind direction
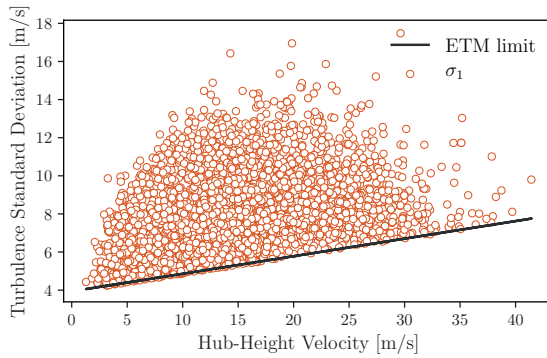
(b) ETM events against V_{hub}
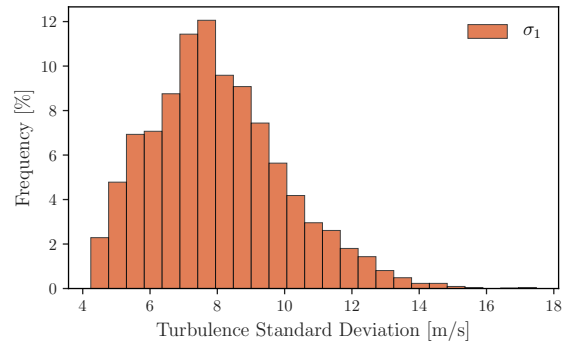
(c) Histogram of ETM events

Figure 52. ETM events recorded by M5

reproduced in Eq. (7.16) defining the extreme wind direction change magnitude, $\Delta\theta_e$, as,

$$\Delta\theta_e = \arctan\left[\frac{\sigma_1}{V_{hub}\left(1 + 0.1\frac{D}{\Lambda_1}\right)}\right] \quad (7.16)$$

According to Eq. (7.16), the threshold for the extreme wind direction change depends on the mean and variance of hub-height wind speed, where lower wind speeds correspond to a higher threshold of direction change. If the absolute value of the calculated wind direction change is higher than the threshold defined in Eq. (7.16) for a given hub-height velocity, $\Delta\theta > \Delta\theta_e$, the change is flagged as an EDC event.

Figure 53b shows the reported EDC events against the wind direction at the beginning of the observed EDC event. Figure 53b indicates that EDC events are more commonly observed when the bulk flow issues from the north or north-northwest, and are relatively rare from the south. On average, EDC events are observed during nearly 3,000 10-min periods per year, with an average magnitude of direction change greater than $110°$ in either the clockwise or counterclockwise direction (where $\Delta\theta > 0$ or $\Delta\theta < 0$, respectively).
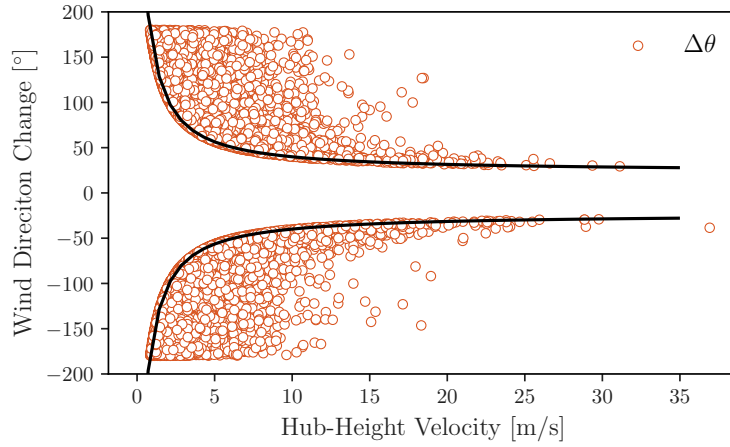
(a) EDC events,V_{hub} against $\Delta\theta_e$
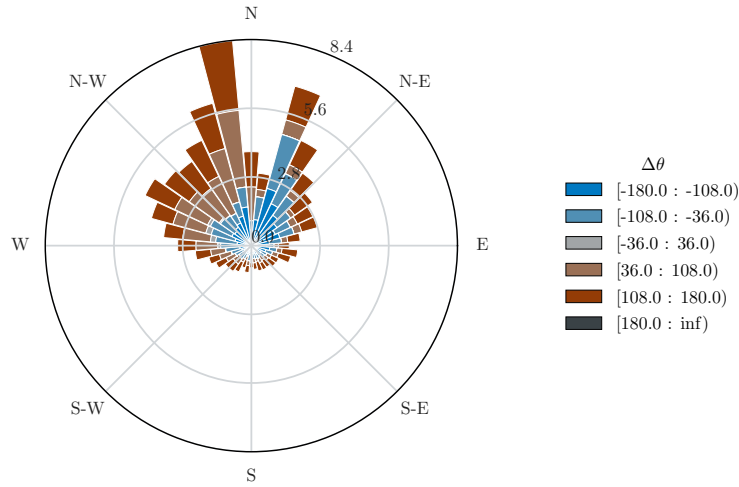
**(b) EDC event rose comparing wind direction change
against prevailing wind direction during observation**

Figure 53. EDC events recorded by M5

7.5 Extreme Coherent Gust with Direction Change (ECD) Events

Events including simultaneous shifts in wind speed and wind direction above a specified threshold are considered to be ECD events. Both the wind speed and wind direction are associated with characteristic dynamic events that must occur within the same 10-s window. The definition of an ECD event relies on a constant coherent gust velocity, $V_{cg} = 15$ m/s and a variable coherent gust direction change. The ECD velocity dynamic follows the form,

$$V(z,t) = V(z) + 0.5V_{cg}(1 - \cos(\pi t/T)) \tag{7.17}$$

where $V(z)$ is the standard normal wind profile shown in Figure 41b. In the current case, only hub-height velocity is being considered. With the velocity defined in Eq. (7.17), the coherent gust direction change is

defined as,

$$V(z,t) = \begin{cases} 180° & \text{for } V_{\text{hub}} < 4 \text{ m/s} \\ \dfrac{720°}{V_{\text{hub}}} & \text{for } 4 \text{ m/s} < V_{\text{hub}} < V_{\text{ref}} \end{cases} \tag{7.18}$$

(a) ECD events by average wind direction

(b) Scatter plot of qualifying wind speed
and direction changes ECD events

(c) Histogram of ECD events
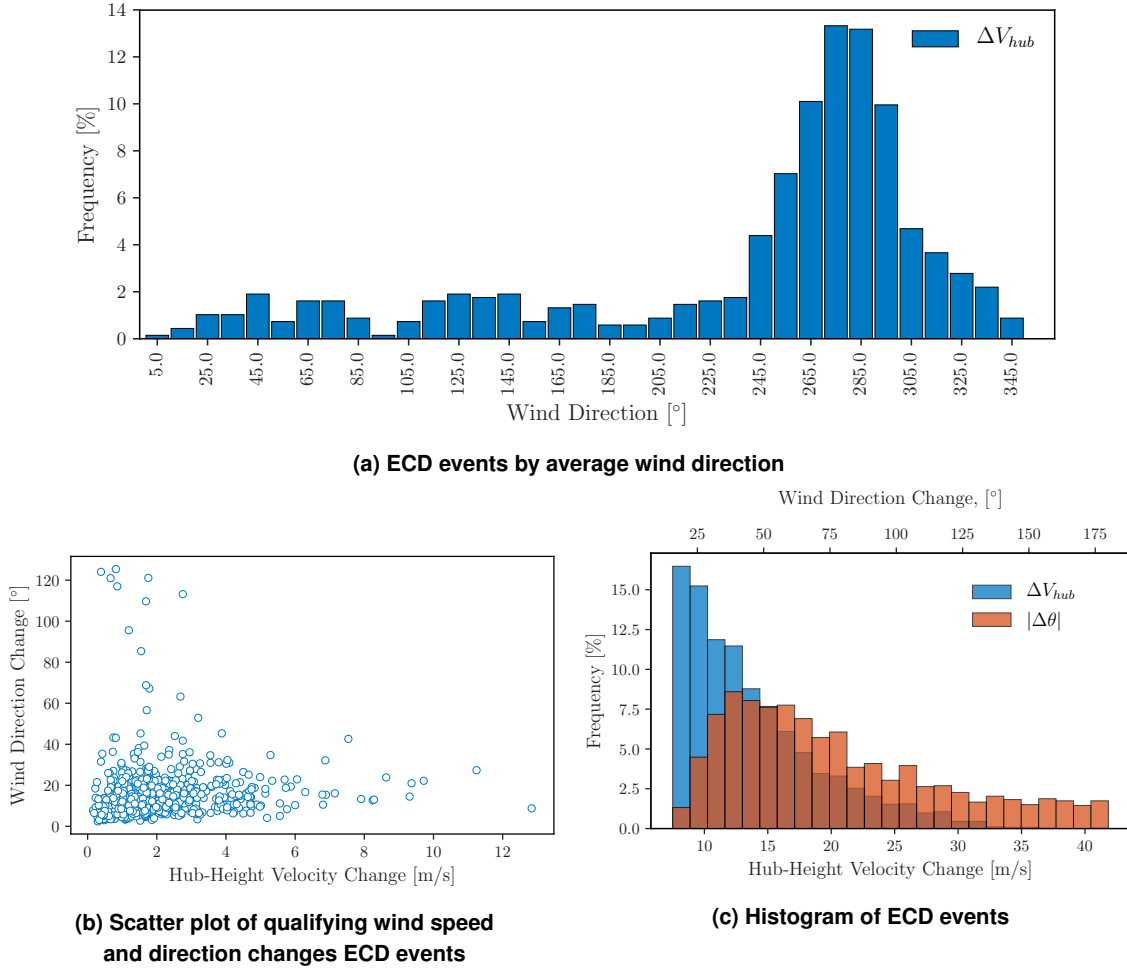
Figure 54. ECD events recorded by M5

ECD events represent potential scenarios of significant structural loading on a wind turbine and occupy the cross section of both EOG and EDC events. Accordingly, extreme coherent gusts occur less frequently than either extreme operating gusts or extreme direction changes on their own. Because ECD events require simultaneous wind speed and wind direction changes, the respective thresholds outlined by Eqs. (7.17) and (7.18) are lower than for each event type individually. As with most other extreme events observed at the NWTC, ECD events are most common in November, and virtually unobserved in the summer months. Figure 54a indicates that ECD events are most commonly associated with winds from the prevailing flow direction at the NWTC.

Figure 54b compares the qualifying deltas of wind speed and wind direction for each ECD event recorded at the NWTC. The scatter plot indicates that the largest observed wind direction change part of a ECD event is greater than 12 m/s and is associated with a direction change of approximately 12°. The figure (and the

66

formulation in Eq. (7.18)) treats changes of the wind direction in either a clockwise or a counterclockwise sense identically. Figure 54c contains histograms of both ΔV_{hub} (blue) and $|\Delta\theta|$. The histograms indicate that ECD events are more commonly ($\approx 92\,\%$) associated with gusts of 6 m/s or less. ECD events associated with gusts stronger than 10 m/s represent less than 5% of those observed by M5. The wind direction change is less concentrated in a specific range, but the red histogram in Figure 54c indicates that most ECD events are associated with wind direction changes between $5°$ and $50°$.

7.6 Extreme Wind Shear (EWS) Events

The IEC defines extreme wind shear (EWS) events as periods wherein the shear exponent exceeds a pre-scribed level either above or below a nominal value. Both vertical and horizontal sheer are relevant to the design and operation of wind turbines, as they represent the degree of asymmetrical loading imposed on the rotor. Shear is quantified through the exponent used to fit a log-law velocity profile onto observed flow conditions. An extreme wind shear event is dynamic and occurs over a set time span of 12 s. The threshold to consider a change in shear exponent as extreme varies relative to the mean velocity. The wind shear exponent is calculated from wind speed records subjected to a 3-s moving-average low-pass-filter, as described in Section 7.4.

A dynamic shearing event outlined in the IEC is an idealized change of velocities observed at the top-tip and bottom-tip of the rotor, shown in Figure 55a. Velocity transients defining an EWS event follow the formulation,

$$V(z) = V_{hub} \left(\frac{z}{z_{hub}} \right)^{\alpha} \pm \frac{z - z_{hub}}{D} \left(2.5 + 0.2\beta\sigma_1 \left(\frac{D}{\Lambda_1} \right)^{0.25} \right) (1 - \cos(2\pi t/T)) \qquad (7.19)$$

where $z_1 = 38$ m, $z_2 = 122$ m, $\alpha = 0.2$, $\beta = 6.4$, and $T = 12$ s. The normal turbulence standard deviation σ_1 is defined in Eq. (7.4). Transients shown in Figure 55a correspond to the peak values that occur at $t = T/2 = 6$ s. The formulation in Eq. (7.19) defines a dynamically shearing velocity profile. At $t = 6$ s, the extreme cases of the shearing profile reach there most positive or negative values for α_+ and α_-, respectively. Limiting shear profiles are shown in Figure 55b along with the standard normal profile with $\alpha = 0.2$.

From each of the limiting shear profiles, an effective value of α is calculated from the velocities at top-tip and bottom tip of the rotor. In the current development, top-tip height is taken as $z_{top} = 122$ m, and bottom-tip is taken at $z_{bottom} = 38$ m. Then the effective shear exponent for a given hub-height velocity is,

$$\alpha_e = \frac{\log(V_{top}/V_{bottom})}{\log(z_{top}/z_{bottom})} \qquad (7.20)$$

Limiting cases that define EWS events are shown in Figure 55c
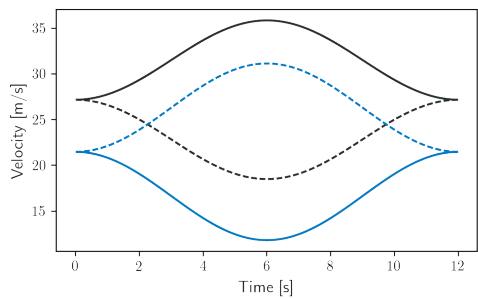
(a) Idealized velocity transients for a hub-height velocity of $V_{\text{hub}} = 25$ m/s
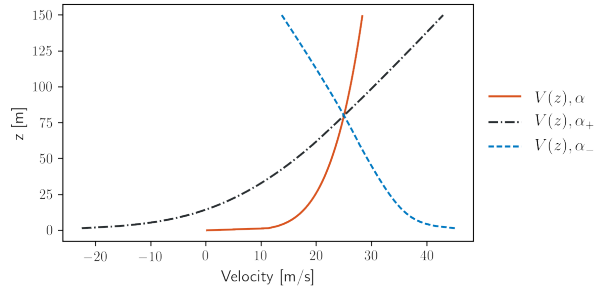
(b) Standard normal velocity profile compared to extreme positive and negative shear profiles for $V_{\text{hub}} = 25$ m/s at $t = T/2$
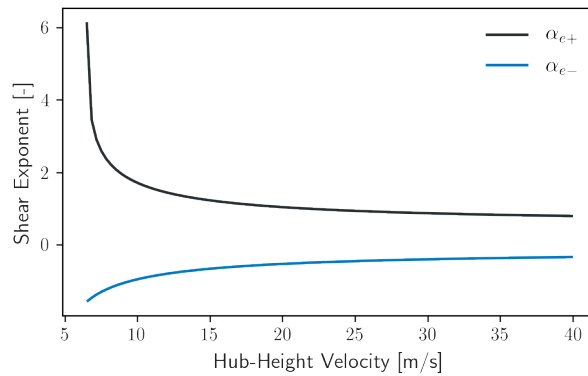
(c) Limiting positive and negative values of the shear exponent, α_+ and α_-, respectively

Figure 55. Specified IEC EWS characteristics
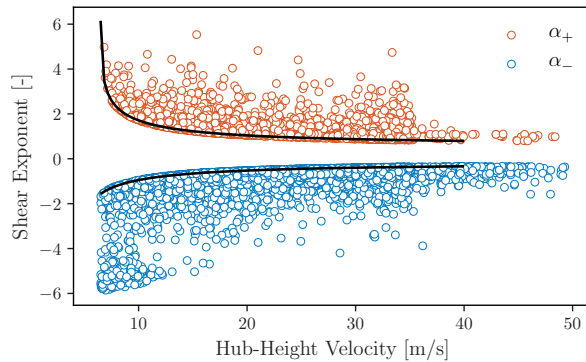
(a) Observed EWS events compared to positive and negative shear thresholds, α_{e+} and α_{e-}, black lines
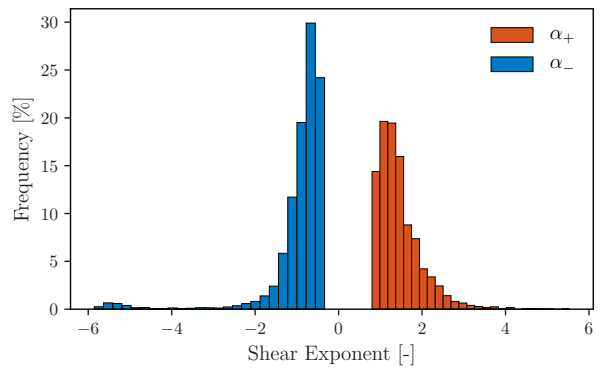
(b) Histograms of positive and negative EWS events

Figure 56. EWS events recorded by M5

To provide some sense of how EWS events are related to the atmospheric conditions at the NWTC, Figure 57 shows the relative frequency of events against the average wind direction calculated within each respected T-s window. Most notable from Figure 57 is that both positive and negative EWS events are frequently associated with winds coming from the east, despite the prevailing westerly winds at the site. The figure

also indicates that most negative EWS events (α_-) are more commonly associated with winds from the NE, while positive EWS events (α_+) are slightly more common from the east and the west.
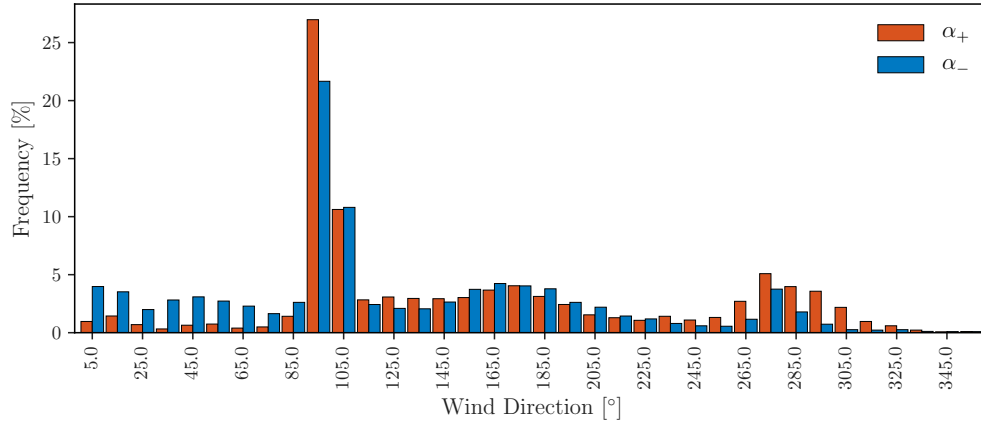
Figure 57. Relative frequency of observed EWS events organized by mean wind direction

8 Summary

The NWTC offers utility-scale wind turbine facilities and unique atmospheric conditions for wind energy research and validation purposes. A multitude of field campaigns have been executed at this site to address different scientific questions and to perform validation studies of full-scale wind turbine technologies. Power performance tests are conducted on-site to characterize the power curve of wind turbines and validate wind turbine blade designs.

A wind resource assessment plays an important role for designing a campaign or validation test, given that scientific and commercial applications rely heavily on the particular operating conditions of the site. In this work, time series data spanning 6 years from a 135-m met mast is used to quantify the atmospheric conditions on site. Overall atmospheric conditions are summarized to provide an overview of the expected behavior on site. Further detail is provided regarding the diurnal and annual periodicity to wind conditions, as well as a detailed view of the conditions at the NWTC under relatively low turbulence intensity.

Daily averaged records of atmospheric parameters reveal the strong and regular periodicity of the conditions at the wind site. Moreover, the quantification of basic thermodynamic properties of the atmosphere, such as barometric pressure and potential temperature, is clearly and easily linked to more fundamental driving forces like incident solar radiation and more complex characteristics of the atmospheric flow like wind shear, veer, and stability. Cumulative trends in the atmospheric stability indicate that the NWTC is characterized by very unstable conditions during the day and stable or very stable conditions at night.

Taking a more granular view of the atmospheric resource by conditionally averaging data over both time of day and month shows the annual variation one can expect at the NWTC (along with the more fundamental thermodynamic properties of the atmosphere). Unsurprisingly, unstable periods are much more common during the summer months, when there are more daylight hours, and the terrain receives more solar radiation. The wind resource is also greatly attenuated during the summer months at the NWTC, reducing the influence of mechanical shear driven turbulence as compared to the contribution of buoyancy-driven turbulence. The nighttime remains well-characterized by strongly stable conditions throughout the year. During the winter months, roughly from November to March, the relative frequency of neutral conditions is greatly increased to as much as 32% of an average day, up from less than 8% of the day during the summer months.

Periods of low turbulence are relatively infrequent at the NWTC, which is known for extremely gusty behavior and variability in the wind resource. Throughout the year, observations made at M5, where the $TI \leq 10\%$, represent only about 20% of the total observations. Further, periods of low turbulence are not clearly distinguished in terms of air pressure, density, or temperature. Rather, they are most easily distinguished in terms of the wind direction. Low-turbulence conditions are significantly less common from the west, which is the prevailing wind direction at the NWTC. Periods of low turbulence intensity are much more commonly associated with weather patterns traveling north or south along the Front Range of the Colorado Rockies.

The NWTC is also well-recognized as a location for validating turbine performance under extreme weather conditions. IEC standards provide general recommendations for the identification of extreme wind events. NWTC data are evaluated against the IEC recommendations for extreme wind speeds, wind shear, and wind direction. Extreme events are evaluated in terms of their mean values, standard deviations, and yearly occurrence. The NWTC experiences extreme atmospheric events many times per year, which make the site a viable resource to test the response of wind turbine blades under extreme conditions. The frequency of extreme events was determined using the IEC recommendations for threshold values for extreme wind speeds, operating gusts, shearing events, and changes in wind direction. The NWTC has a high rate of

occurrence of particular extreme events; for example, extreme wind direction change events occur at an average rate of 2,880 events per year. The estimated 50-year extreme wind speed for the NWTC site is 57.3 m/s. However, it should be noted that this estimate is made based on only 6 years of data while more than 10-year of data is recommended.

Parties interested in further exploration of the data collected by the met masts at the NWTC are encouraged to explore the analysis and visualization codebase developed at the National Renewable Energy Laboratory (https://github.com/NREL/MetMastVis). All of the underlying code used to develop the visualizations and quality control for met mast data are available in the repository. Interested parties are encouraged to contribute feedback on the visualization platform or to contribute directly by adding content to the analysis and visualization codebase. The full data, including all raw data channels at 20 Hz and derived values are available on NREL's website (https://nwtc.nrel.gov/135mData).

Appendix A Raw Data Channels

Table A.1. M4 Data Channels

Channel	Description	Variable	Height
6	Sonic *x* velocity	Raw_Sonic_*x*_131	131
7	Sonic *y* velocity	Raw_Sonic_*y*_131	131
8	Sonic *z* velocity	Raw_Sonic_*z*_131	131
9	Sonic temperature	Raw_Sonic_Temp_131	131
10	Sonic *x* velocity	Raw_Sonic_*x*_100	100
11	Sonic *y* velocity	Raw_Sonic_*y*_100	100
12	Sonic *z* velocity	Raw_Sonic_*z*_100	100
13	Sonic temperature	Raw_Sonic_Temp_100	100
14	Sonic *x* velocity	Raw_Sonic_*x*_76	76
15	Sonic *y* velocity	Raw_Sonic_*y*_76	76
16	Sonic *z* velocity	Raw_Sonic_*z*_76	76
17	Sonic temperature	Raw_Sonic_Temp_76	76
18	Sonic *x* velocity	Raw_Sonic_*x*_50	50
19	Sonic *y* velocity	Raw_Sonic_*y*_50	50
20	Sonic *z* velocity	Raw_Sonic_*z*_50	50
21	Sonic temperature	Raw_Sonic_Temp_50	50
22	Sonic *x* velocity	Raw_Sonic_*x*_30	30
23	Sonic *y* velocity	Raw_Sonic_*y*_30	30
24	Sonic *z* velocity	Raw_Sonic_*z*_30	30
25	Sonic temperature	Raw_Sonic_temp_30	30
26	Sonic *x* velocity	Raw_Sonic_*x*_15	15
27	Sonic *y* velocity	Raw_Sonic_*y*_15	15
28	Sonic *z* velocity	Raw_Sonic_*z*_15	15
29	Sonic temperature	Raw_Sonic_Temp_15	15
30	Air temperature	Raw_Air_Temp_88m	88
31	Air temperature	Raw_Air_Temp_26	26
32	Air temperature	Raw_Air_Temp_3	3
33	Dewpoint temperature	Raw_Dewpt_Temp_134m	134
34	Dewpoint temperature	Raw_Dewpt_Temp_88m	88
35	Dewpoint temperature	Raw_Dewpt_Temp_26m	26
36	Dewpoint temperature	Raw_Dewpt_Temp_3m	3
37	ΔT	Raw_DeltaT_134_88m	88
38	ΔT	Raw_DeltaT_88_26m	26
39	ΔT	Raw_DeltaT_26_3m	3
40	Vane wind direction	Raw_Vane_WD_134m	134
41	Vane wind direction	Raw_Vane_WD_88m	88
42	Vane wind direction	Raw_Vane_WD_26m	26
43	Vane wind direction	Raw_Vane_WD_10m	10
44	Vane wind direction	Raw_Vane_WD_3m	3

Channel	Description	Variable	Height
45	Acceleration in x	Raw_Accel_x_131	131
46	Acceleration in y	Raw_Accel_y_131	131
47	Acceleration in z	Raw_Accel_z_131	131
48	Acceleration in x	Raw_Accel_x_100	100
49	Acceleration in y	Raw_Accel_y_100	100
50	Acceleration in z	Raw_Accel_z_100	100
51	Acceleration in x	Raw_Accel_x_76	76
52	Acceleration in y	Raw_Accel_y_76	76
53	Acceleration in z	Raw_Accel_z_76	76
54	Acceleration in x	Raw_Accel_x_50	50
55	Acceleration in y	Raw_Accel_y_50	50
56	Acceleration in z	Raw_Accel_z_50	50
57	Acceleration in x	Raw_Accel_x_30	30
58	Acceleration in y	Raw_Accel_y_30	30
59	Acceleration in z	Raw_Accel_z_30	30
60	Acceleration in x	Raw_Accel_x_15	15
61	Acceleration in y	Raw_Accel_y_15	15
62	Acceleration in z	Raw_Accel_z_15	15
63	Station pressure	Raw_Baro_Presr_3m	3
64	Precipitation intensity	Raw_PRECIP_INTEN	0
65	Cup wind speed	Raw_Cup_WS_134m	134
66	Cup wind speed	Raw_Cup_WS_88m	88
67	Cup wind speed	Raw_Cup_WS_80m	80
68	Cup wind speed	Raw_Cup_WS_26m	26
69	Cup wind speed	Raw_Cup_WS_10m	10
70	Cup wind speed	Raw_Cup_WS_3m	3

Table A.2. M5 Data Channels

Channel	Description	Variable	Height
6	Sonic x velocity	Raw_Sonic_x_119	119
7	Sonic y velocity	Raw_Sonic_y_119	119
8	Sonic z velocity	Raw_Sonic_z_119	119
9	Sonic temperature	Raw_Sonic_Temp_119	119
10	Sonic x velocity	Raw_Sonic_x_100	100
11	Sonic y velocity	Raw_Sonic_y_100	100
12	Sonic z velocity	Raw_Sonic_z_100	100
13	Sonic temperature	Raw_Sonic_Temp_100	100
14	Sonic x velocity	Raw_Sonic_x_74	74
15	Sonic y velocity	Raw_Sonic_y_74	74

Channel	Description	Variable	Height
16	Sonic z velocity	Raw_Sonic_z_74	74
17	Sonic temperature	Raw_Sonic_Temp_74	74
18	Sonic x velocity	Raw_Sonic_x_61	61
19	Sonic y velocity	Raw_Sonic_y_61	61
20	Sonic z velocity	Raw_Sonic_z_61	61
21	Sonic temperature	Raw_Sonic_Temp_61	61
22	Sonic x velocity	Raw_Sonic_x_41	41
23	Sonic y velocity	Raw_Sonic_y_41	41
24	Sonic z velocity	Raw_Sonic_z_41	41
25	Sonic temperature	Raw_Sonic_temp_41	41
26	Sonic x velocity	Raw_Sonic_x_15	15
27	Sonic y velocity	Raw_Sonic_y_15	15
28	Sonic z velocity	Raw_Sonic_z_15	15
29	Sonic temperature	Raw_Sonic_Temp_15	15
30	Air temperature	Raw_Air_Temp_87m	87
31	Air temperature	Raw_Air_Temp_38m	38
32	Air temperature	Raw_Air_Temp_3m	3
33	Dewpoint temperature	Raw_Dewpt_Temp_122m	122
34	Dewpoint temperature	Raw_Dewpt_Temp_87m	87
35	Dewpoint temperature	Raw_Dewpt_Temp_38m	38
36	Dewpoint temperature	Raw_Dewpt_Temp_3m	3
37	ΔT	Raw_DeltaT_122_87m	87
38	ΔT	Raw_DeltaT_87_38m	38
39	ΔT	Raw_DeltaT_38_3m	3
40	Vane wind direction	Raw_Vane_WD_122m	122
41	Vane wind direction	Raw_Vane_WD_87m	87
42	Vane wind direction	Raw_Vane_WD_38m	38
43	Vane wind direction	Raw_Vane_WD_10m	10
44	Vane wind direction	Raw_Vane_WD_3m	3
45	Acceleration in x	Raw_Accel_x_119	119
46	Acceleration in y	Raw_Accel_y_119	119
47	Acceleration in z	Raw_Accel_z_119	119
48	Acceleration in x	Raw_Accel_x_100	100
49	Acceleration in y	Raw_Accel_y_100	100
50	Acceleration in z	Raw_Accel_z_100	100
51	Acceleration in x	Raw_Accel_x_74	74
52	Acceleration in y	Raw_Accel_y_74	74
53	Acceleration in z	Raw_Accel_z_74	74
54	Acceleration in x	Raw_Accel_x_61	61
55	Acceleration in y	Raw_Accel_y_61	61
56	Acceleration in z	Raw_Accel_z_61	61

Table A.2 – continued from previous page

Channel	Description	Variable	Height
57	Acceleration in x	Raw_Accel_x_41	41
58	Acceleration in y	Raw_Accel_y_41	41
59	Acceleration in z	Raw_Accel_z_41	41
60	Acceleration in x	Raw_Accel_x_15	15
61	Acceleration in y	Raw_Accel_y_15	15
62	Acceleration in z	Raw_Accel_z_15	15
63	Station pressure	Raw_Baro_Presr_3m	3
64	Precipitation intensity	Raw_PRECIP_INTEN	0
65	Cup wind speed	Raw_Cup_WS_C1_130m	130
66	Cup wind speed	Raw_Cup_WS_122m	122
67	Cup wind speed	Raw_Cup_WS_C1_105m	105
68	Cup wind speed	Raw_Cup_WS_87m	87
69	Cup wind speed	Raw_Cup_WS_C1_80m	80
70	Cup wind speed	Raw_Cup_WS_C1_55m	55
71	Cup wind speed	Raw_Cup_WS_38m	38
72	Cup wind speed	Raw_Cup_WS_C1_30m	30
73	Cup wind speed	Raw_Cup_WS_10m	10
74	Cup wind speed	Raw_Cup_WS_3m	3

Appendix B Extreme Wind Speed Estimate Statistics

Extrapolation of wind speed distributions found in Section 7.1.2 demonstrate some sensitivity to the thresholds used to filter out low-speed observations. The final results considered in the main text rely on the threshold of $\mu + 1.4 \times \sigma$, or 1.4 standard deviations of the collection of wind speeds over their respective mean. This threshold conveniently supplies similar estimates using both the two-parameter Weibull and Gumbel distributions (Eqs. (7.8) and (7.9), respectively) for both the 3-s and 10-min averaged wind speeds. The same threshold was also used in previous work extrapolating to rare events by Moriarty, Holley, and Butterfield (2004).

Table B.1. Descriptive statistics from least-squares fits of
Weibull and Gumbel distributions to wind speed observations.

	V_{50} 3-s average wind speed		V_{e50} 10-min average wind speed	
	Weibull	Gumbel	Weibull	Gumbel
Mean [m/s]	43.78	40.18	57.28	53.79
Std. Dev. [m/s]	4.10	1.97	7.38	5.86
Min. [m/s]	40.50	38.27	50.28	47.28
Max. [m/s]	48.33	42.69	67.94	61.44

The distributions found by least-squares fitting to wind speed observations over the threshold can also be used in an inverse sense to provide estimates of recurrence rates to the EWM velocity thresholds recommended by the IEC standards. Estimated rates of recurrence are tabulated below. Note that the sensitivity of the fitted distribution applies to the inverse consideration as well: these values should be expected to change by altering the thresholds considered or by modifying the data record considered to include only seasonal wind speed observations or include more years of data.

Table B.2. Estimated rates of recurrence of EWM events outlined in the IEC Standards.

| EWM event	V_1	V_{50}	V_{e1}	V_{e50}
Velocity Threshold [m/s]	40.0	50.0	56.0	70. 0
Estimated Recurrence rate – Weibull [years]	45	3,700	85	13,700
Estimated Recurrence rate – Gumbel [years]	63	3,700	142	13,700

Appendix C Gust Characterization

According to Hu, Letson, Barthelmie, and Pryor (2018), 20-Hz 10-min wind signals are smoothed to remove the higher frequency spikes with a 3-s moving window. A low-pass-filtered signal based on a 3-s moving window is shown in Figure C.1a, along with the spectral behavior. The peak wind speed is identified in terms of its amplitude above the background wind speed. In this work, gust events are described by parameters including maximum wind speed (calculated from 3-s moving average wind signal) over 10-min period, V_{max}, the difference of maximum wind speed to the 10-min mean, V_a, the ratio of the maximum wind speed to 10-min mean G_r, duration of the peak wind speed over 10-min mean wind speed T_g, and gust length, G_L.
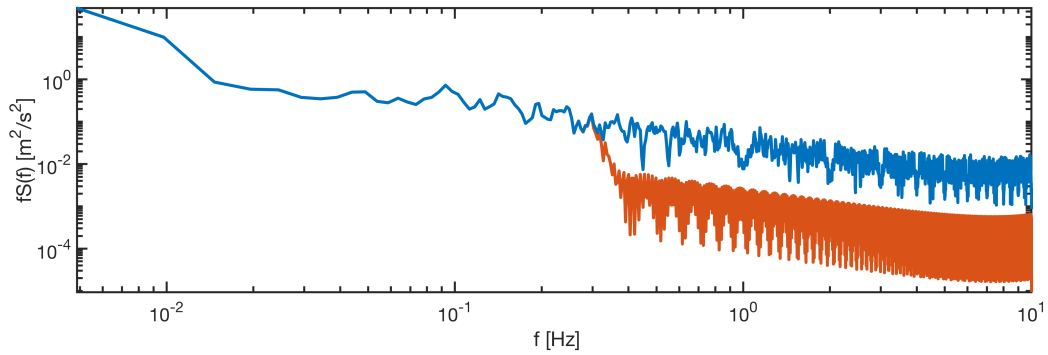
$$V_a = V_{max} - \overline{V} \tag{1}$$

$$G_r = \frac{V_{max}}{\overline{V}} \tag{2}$$

$$G_L = \int_{t_a}^{t_b} V(t)dt \tag{3}$$

where t_a and t_b are the starting and ending time of the peak wind speed over the $\overline{V}$, respectively. The gust period is marked with a shaded region in Figure C.1a
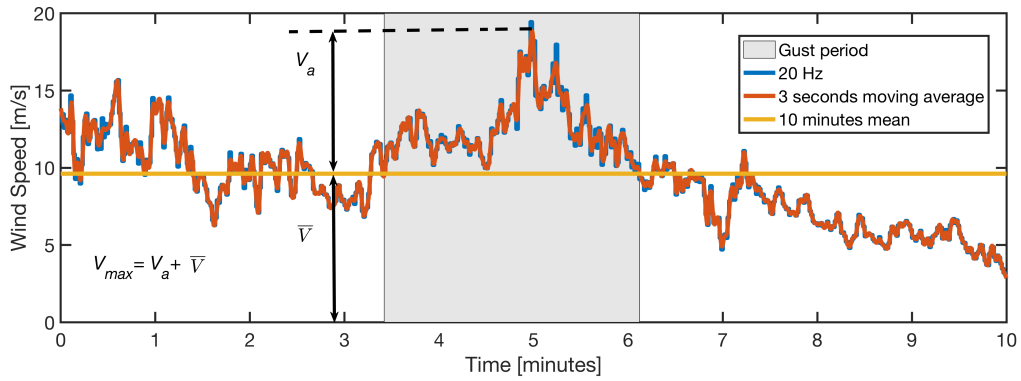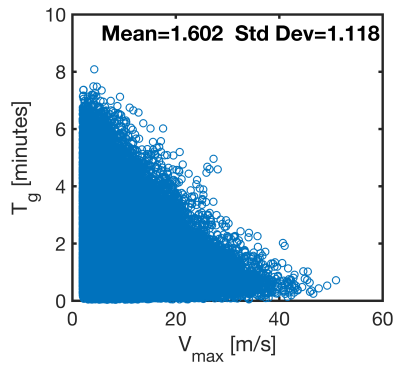
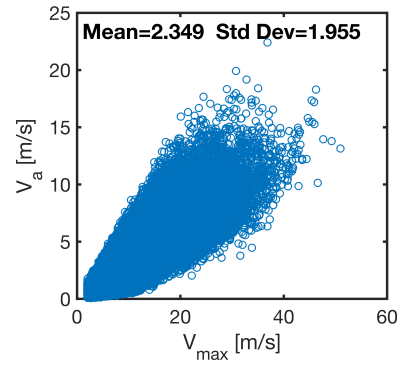**(a) A 10-min signal sampled with 20-Hz in time domain**

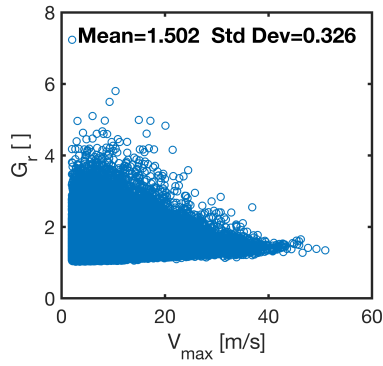**(b) A 10-min signal sampled with 20-Hz in frequency domain**

Figure C.1. Example of a 10-min wind speed signal with a 3-s moving average signal and time average mean
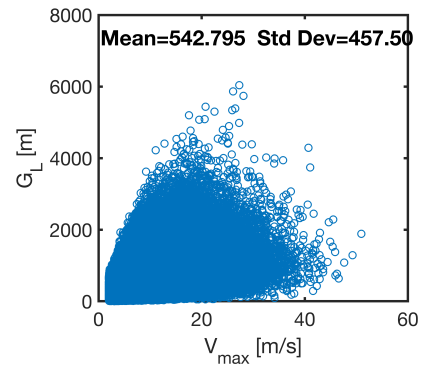
(a) Time duration of peaks of 10-min signals over 10-min average wind speed

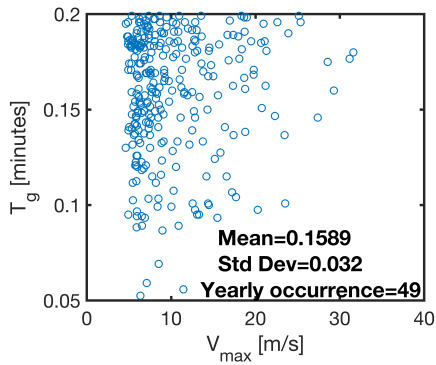**(b)** Amplitude of the peak wind with respect to 10-min average wind speed

(c) Ratio of the peak wind speed to 10-min average wind speed

(d) Gust length

Figure C.2. Different gust parameters are plotted against the peaks of 10-min wind signals

79

(a) Time duration of peaks of 10-min signals over 10-min average wind speed

(b) Amplitude of the peak wind with respect to 10-min average wind speed

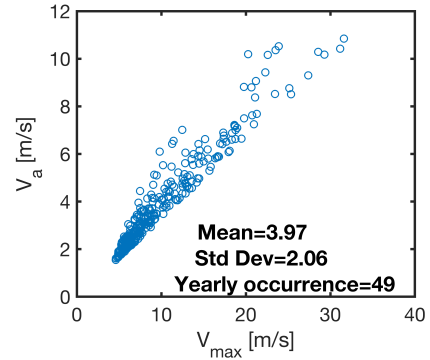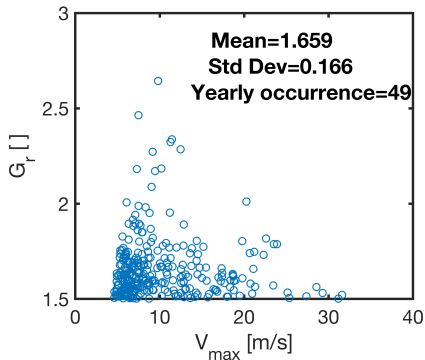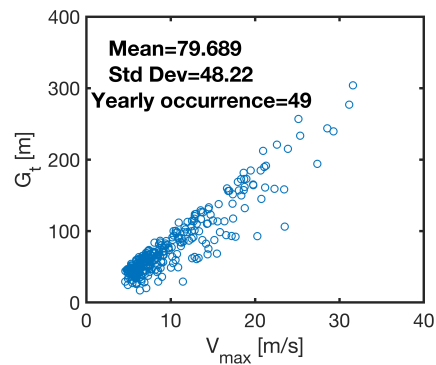**(c) Ratio of the peak wind speed to 10-min average wind speed**

(d) Gust length

Figure C.3. Different gust parameters are plotted against the peaks of 10-min wind signals with gust identification conditions

References

Abkar, Mahdi, and Fernando Porté-Agel. 2015. "Influence of Atmospheric Stability on Wind-Turbine Wakes: A Large-Eddy Simulation Study." *Physics of Fluids* 27 (3): 035104. doi:10.1063/1.4913695. eprint: https://doi.org/10.1063/1.4913695. https://doi.org/10.1063/1.4913695.

Ali, Naseem, Nicholas Hamilton, Gerard Cortina, Marc Calaf, and Raúl Bayoán Cal. 2018. "Anisotropy Stress Invariants of Thermally Stratified Wind Turbine Array Boundary Layers Using Large Eddy Simulations." *Journal of Renewable and Sustainable Energy* 10 (1): 013301.

Banta, RM, RK Newsom, JK Lundquist, YL Pichugina, RL Coulter, and L Mahrt. 2002. "Nocturnal Low-level Jet Characteristics over Kansas During CASES-99." *Boundary-Layer Meteorology* 105 (2): 221–252.

Banta, RM, LD Olivier, and PH Gudiksen. 1993. "Sampling Requirements for Drainage Flows That Transport Atmospheric Contaminants in Complex Terrain." *Radiation Protection Dosimetry* 50 (2-4): 243–248.

Barthelmie, Rebecca Jane, and LE Jensen. 2010. "Evaluation of Wind Farm Efficiency and Wind Turbine Wakes at the Nysted Offshore Wind Farm." *Wind Energy* 13 (6): 573–586.

Bhaganagar, Kiran, and Mithu Debnath. 2014. "Implications of Stably Stratified Atmospheric Boundary Layer Turbulence on the Near-Wake Structure of Wind Turbines." *Energies* 7 (9): 5740–5763. ISSN: 1996-1073. http://www.mdpi.com/1996-1073/7/9/5740.

Businger, Joost A, John C Wyngaard, Y. Izumi, and Edward F Bradley. 1971. "Flux-profile Relationships in the Atmospheric Surface Layer." *Journal of the Atmospheric Sciences* 28 (2): 181–189.

Chamorro, Leonardo P, and Fernando Porté-Agel. 2009. "A Wind-tunnel Investigation of Wind-turbine Wakes: Boundary-Layer Turbulence Effects." *Boundary-Layer Meteorology* 132 (1): 129–149.

Clifton, A. 2014. "135-m Meteorological Masts at the National Wind Technology Center: Instrumentation, Data Acquisition and Processing." https://wind.nrel.gov/MetData/Publications/NWTC_135m_MetMasts.pdf.

Clifton, Andrew, and Julie K Lundquist. 2012. "Data Clustering Reveals Climate Impacts on Local Wind Phenomena." *Journal of Applied Meteorology and Climatology* 51 (8): 1547–1557.

Cook, N.J. 1982. "Towards Better Estimation of Extreme Winds." *Journal of Wind Engineering and Industrial Aerodynamics* 9 (3): 295–323. ISSN: 0167-6105. doi:https://doi.org/10.1016/0167-6105(82)90021-6. http://www.sciencedirect.com/science/article/pii/0167610582900216.

Garratt, John Roy. 1994. "The Atmospheric Boundary Layer." *Earth-Science Reviews* 37 (1-2): 89–134.

Gusclla, Vittorio. 1991. "Estimation of Extreme Winds from Short Term Records." *Journal of Structural Engineering* 117 (2): 375–390. doi:10.1061/(ASCE)0733-9445(1991)117:2(375).

Hamilton, Nicholas, Hyung Suk Kang, Charles Meneveau, and Raúl Bayoán Cal. 2012. "Statistical Analysis of Kinetic Energy Entrainment in a Model Wind Turbine Array Boundary Layer." *Journal of Renewable and Sustainable Energy* 4 (6): 063105.

Hand, M Maureen, Neil D Kelley, and Mark J Balas. 2003. "Identification of Wind Turbine Response to Turbulent Inflow Structures." In *ASME/JSME 2003 4th Joint Fluids Summer Engineering Conference*, 2557–2566. American Society of Mechanical Engineers.

Hansen, Brian O, Xiaoli G Larsén, Mark C Kelly, Ole S Rathmann, Jacob Berg, Andreas Bechmann, Anna Maria Sempreviva, and Hans E Jørgensen. 2016. *Extreme Wind Calculation Applying Spectral Correction Method–Test and Validation*. DTU Wind Energy: Copenhagen, Denmark.

Hansen, Kurt S, and Gunner Chr Larsen. 2005. "Characterising Turbulence Intensity for Fatigue Load Analysis of Wind Turbines." *Wind Engineering* 29 (4): 319–329.

Hosking, J. R. M., J. R. Wallis, and E. F. Wood. 1985. "Estimation of the Generalized Extreme-Value Distribution by the Method of Probability-Weighted Moments." *Technometrics* 27 (3): 251–261. ISSN: 00401706. http://www.jstor.org/stable/1269706.

Hu, W., F. Letson, R. J. Barthelmie, and S. C. Pryor. 2018. "Wind Gust Characterization at Wind Turbine Relevant Heights in Moderately Complex Terrain." *Journal of Applied Meteorology and Climatology*. doi:10.1175/JAMC-D-18-0040.1. eprint: https://doi.org/10.1175/JAMC-D-18-0040.1. https://doi.org/10.1175/JAMC-D-18-0040.1.

IEC, CDV. 2005. "61400-12-1: Wind Turbines—Part 12-1: Power Performance Measurements of Electricity Producing Wind Turbines."

Larsén, Xiaoli Guo, Jakob Mann, Ole Rathmann, and Hans E. Jørgensen. 2013. "Uncertainties of the 50-year Wind from Short Time Series Using Generalized Extreme Value Distribution and Generalized Pareto Distribution." *Wind Energy* 18 (1): 59–74. doi:10.1002/we.1683. eprint: https://onlinelibrary.wiley.com/doi/pdf/10.1002/we.1683. https://onlinelibrary.wiley.com/doi/abs/10.1002/we.1683.

Lundquist, J. K., M. J. Churchfield, S. Lee, and A. Clifton. 2015. "Quantifying Error of Lidar and Sodar Doppler Beam Swinging Measurements of Wind Turbine Wakes Using Computational Fluid Dynamics." *Atmospheric Measurement Techniques* 8 (): 907–920. doi:10.5194/amt-8-907-2015.

Mann, J., L. Kristensen, and N.O. Jensen. 1998. "Uncertainties of Extreme Winds, Spectra, and Coherences." In *Bridge Aerodynamics*, ed. by A. Larsen and S. Esdahl, 49–56. CRC Press/Balkema. ISBN: 90-5410-961-0.

Moriarty, PJ, WE Holley, and SP Butterfield. 2004. "Extrapolation of extreme and fatigue loads using probabilistic methods": NREL/TP–500–34421.

Mücke, Tanja, David Kleinhans, and Joachim Peinke. 2011. "Atmospheric Turbulence and Its Influence on the Alternating Loads on Wind Turbines." *Wind Energy* 14 (2): 301–316.

Oncley, Steven P, Carl A Friehe, John C Larue, Joost A Businger, Eric C Itsweire, and Sam S Chang. 1996. "Surface-Layer Fluxes, Profiles, and Turbulence Measurements over Uniform Terrain under Near-neutral Conditions." *Journal of the Atmospheric Sciences* 53 (7): 1029–1044.

Pearson, Ronald K., Yrjö Neuvo, Jaakko Astola, and Moncef Gabbouj. 2016. "Generalized Hampel Filters." *EURASIP Journal on Advances in Signal Processing* 2016 (1): 87. ISSN: 1687-6180. doi:10.1186/s13634-016-0383-6. https://doi.org/10.1186/s13634-016-0383-6.

Poulos, Gregory S., William Blumen, David C. Fritts, Julie K. Lundquist, Jielun Sun, Sean P. Burns, Carmen Nappo, et al. 2002. "CASES-99: A Comprehensive Investigation of the Stable Nocturnal Boundary Layer." *Bulletin of the American Meteorological Society* 83 (4): 555–582. doi:10.1175/1520-0477(2002)083<0555:CACIOT>2.3.CO;2. eprint: https://doi.org/10.1175/1520-0477(2002)083<0555:CACIOT>2.3.CO;2. https://doi.org/10.1175/1520-0477(2002)083<0555:CACIOT>2.3.CO;2.

Pryor, S. C., R. J. Barthelmie, N. E. Clausen, M. Drews, N. MacKellar, and E. Kjellström. 2012. "Analyses of Possible Changes in Intense and Extreme Wind Speeds over Northern Europe under Climate Change Scenarios." *Climate Dynamics* 38 (1): 189–208. ISSN: 1432-0894. doi:10.1007/s00382-010-0955-3. https://doi.org/10.1007/s00382-010-0955-3.

Wharton, Sonia, and Julie K Lundquist. 2012. "Wind Gust Characterization at Wind Turbine Relevant Heights in Moderately Complex Terrain." *Wind Energy* 15 (4): 525–546.

Wu, Yu-Ting, and Fernando Porté-Agel. 2012. "Atmospheric Turbulence Effects on Wind-Turbine Wakes: An LES Study." *Energies* 5 (12): 5340–5362. ISSN: 1996-1073. doi:10.3390/en5125340. http://www.mdpi.com/1996-1073/5/12/5340.

Wyngaard, JC. 1981. "Cup, Propeller, Vane, and Sonic Anemometers in Turbulence Research." *Annual Review of Fluid Mechanics* 13 (1): 399–423.